POLITECNICO DI MILANO

DIPARTIMENTO DI INGEGNERIA AEROSPAZIALE

Feedback Control of Turbulent Wall Flows

Ph.D. Thesis by:

Fulvio Martinelli

DOTTORATO DI RICERCA IN INGEGNERIA AEROSPAZIALE
XXI CICLO

POLITECNICO DI MILANO
DIPARTIMENTO DI INGEGNERIA AEROSPAZIALE
VIA LA MASA, 34 - 20156 MILANO

Tesi presentata da:
Fulvio Martinelli
per il conseguimento del titolo di *Dottore di Ricerca*

Relatore della Ricerca:
Prof. Maurizio Quadrio

Tutor della Ricerca:
Prof. Paolo Mantegazza

Coordinatore della Scuola di Dottorato:
Prof. Sergio Ricci

DOTTORATO DI RICERCA IN INGEGNERIA AEROSPAZIALE
XXI CICLO

Preface

The present thesis addresses the problem of feedback control of wall turbulence, to the aim of reducing friction. This is a fairly recent and very active research field; its multidisciplinary nature is likely to bring substantial developments in the understanding of turbulence dynamics as well as in control system design. The present work develops and uses an original approach to control and estimation of wall turbulence which is quite different from the strategies presented in the recent literature. The cornerstone is a frequency-domain formulation of the optimal filter and compensator design problems. Nowadays, frequency-domain approaches are often considered "old fashioned", as they are inherently limited to linear time-invariant systems, while state-space approaches can be extended to the time-varying case or the nonlinear case. However, if the design of a linear time-invariant controller is the goal, then the frequency-domain approach becomes particularly attractive when dealing with very high-dimensional systems with a small number of actuators and sensors. This is exactly the case of turbulent flows; therefore, the purpose of this work is to discuss the feasibility of such approaches when designing control systems for turbulent skin friction drag reduction.

The thesis is organized as follows. Chap. 1 presents a general overview of the flow control research field, with particular emphasis on the recently developed feedback control strategies. Furthermore, this chapter provides a succinct review of basic concepts in linear systems, to be used throughout the work in order to make it more self-contained.

The "standard" model-based approach to channel flow control is presented in Chap. 2. In particular, issues regarding the state-space modeling of the channel flow system, as well as the control design procedure, will be discussed; example state-of-the-art results will be presented. Advantages and shortcomings of these approaches will be highlighted, emphasizing issues that will be addressed in the subsequent chapters.

Chap. 3 is devoted to the formulation of the Wiener filtering problem and its application to the state estimation of turbulent channel flow, based on wall-measured quantities. The first computation of the full space-time structure of the noise on the linearized governing equations is presented, and results are briefly discussed. Along with a linearized model of the flow system, these noise data are used in the design of optimal Wiener filters, whose performances are compared to previously proposed

Kalman-based estimation techniques.

Chap. 4 formulates the optimal control problem in the frequency domain, so easing the design of compensators for the channel flow system. This formulation is dual with respect to standard state-space-based techniques, but provides a substantial reduction of the computational burden at the compensator design stage. An alternative linear model of the turbulent channel flow is also presented, which is particularly well-suited in the the frequency-domain framework. Compensators designed within this framework are tested using Direct Numerical Simulations, in order to assess the most efficient combination of parameters and possible Re effects.

Finally, Chapter 5 summarizes and critically discusses the main achievements of the present work and outlines possible future developments.

The reader familiar with control and estimation topics as applied to fluid flow systems may skip the introduction, but is advised to read its last section as well as Chap. 2, where the notation used throughout the thesis is established. Moreover, the reader just interested in the control part may skip Chap. 3, but for the section reviewing Wiener-Hopf equations and related solution techniques, where notation and a few numerical details are presented.

Appendices A and B are devoted to the presentation of "side issues" addressed during the development of the Ph.D. work. In particular, Appendix A considers a study of Re-effects on LQR-controlled turbulence, while Appendix B is focused on fundamental performance limitations in transition control of plane Poiseuille flow when using wall actuation.

The development of this work would not have been possible without the continuous suggestions and encouragement from my advisor, Prof. M. Quadrio, and from my co-advisor, Prof. P. Luchini, to whom I am profoundly indebted. Prof. Luchini is also gratefully acknowledged for having provided the availability of his supercomputing system at the University of Salerno. I would like to acknowledge the warm hospitality and advice of Prof. T. R. Bewley at UC San Diego, where part of the present work was completed. I also wish to thank Prof. P. J. Schmid, Dr. F. Giannetti and Dr. J. O. Pralits for many invaluable discussions concerning this work. Prof. J. F. Whidborne and Dr. J. McKernan are gratefully acknowledged for the collaboration in the research related to Appendix B of this thesis.

During my doctoral work, I had a chance to meet many clever Ph.D. students from different countries. Among them, I wish to thank S. Bagheri, C. Mack, A. Monokrousos, V. De Felice, J. Schulze, J. Cessna, C. Colburn, D. Zhang, K. Kang, M. Mattaboni and F. Cavadini for the many suggestions and discussions; to them I wish the very best for their career. I wish to thank my office mates, Gabriella Gaias, Andrea Brambilla and Alessandro Fumagalli, for creating a nice working environment. Finally, special thanks go to my family and friends, for their patience and support during this adventure.

Milan, February 2009

Fulvio Martinelli

Contents

Chapter 1

Introduction

This chapter presents the state of the art in the field of control of wall turbulence. A review of the recent scientific literature is given, covering both numerical and experimental attempts towards devising effective control strategies. Active feedback control techniques are particularly emphasized; accordingly, a brief review of the fundamental background concepts and tools in system theory is given.

1.1 Control of aerodynamic flows

Control of fluid flows is relevant in a variety of engineering applications, most notably air and naval transportation, combustion, bioengineering and chemical industry [40]. In particular, modern aerospace industry is interested in improving the aerodynamic efficiency of aircrafts. Potential benefits are both environmental (reduced pollution from air transportation) and economic (fuel saving).

Up to present, most of the research regarding aerodynamic efficiency has focused on shape optimization, which can be considered as a *passive* control technique. LFC airfoils, designed to mantain a laminar boundary layer over most of the wing, constitute one well-known example; winglets, typically aimed at reducing induced drag for a given lift in steady conditions [23; 133], are a more recently developed passive control device. Passive techniques are generally developed to improve efficiency in cruise flight.

In take-off and landing configurations, flaps and slats provide the necessary excess lift to sustain the vehicle. Several *active* control techniques have been employed in the past, to improve the efficiency of flap/slat configurations. Most of these active devices are based on steady blowing or suction of the turbulent boundary layer over the airfoil; a typical example is the combination of a standard flap on the trailing edge with boundary layer control at the leading edge of the airfoil [119]. It is important to notice that such techniques are inherently *feedforward*, namely, they are designed on the basis of a certain model of the flow system, which is supposed to remain unchanged during the operations performed by the control devices.

As a consequence, performance of these active techniques is likely to severely degrade when operating off the design point.

Aeroservoelastic control can be regarded as an active *feedback* manipulation of the flow over the flexible aircraft. Despite aeroservoelastic systems are traditionally considered as structural control systems – since the control design is focused on the redistribution of aerodynamic loads on the aircraft structure – they actually perform an active modification of the flow over the vehicle. Typically, aim of aeroservoelastic control is the active damping of unsteady aerodynamic loads, two notable examples being the alleviation of gust loads and the control of transonic buffeting [111; 129; 8]; these control objectives are obtained by appropriate design of feedback control laws for the fully coupled aeroelastic system. Aeroservoelastic control systems act on a relatively large spatial scale, comparable with that of the wings ($\approx O(1\,m)$), and operate at relatively low frequency ($\approx O(10\,Hz) \div O(100\,Hz)$).

The fairly recent development of micro-electro-mechanical-system (MEMS) technology [42; 48; 39; 40; 41; 126] led to new ideas aimed at controlling aerodynamic flows on much smaller time and space scales. MEMS devices operate on spatial scales of the order of $10\,\mu m$ and at frequencies up to $10\,kHz$, thus introducing a new world of possibilities where engineering solutions may be applied. For example, arrays of MEMS actuators and sensors, providing the necessary space/time resolution to act on the fine scale structure of the turbulent boundary layer, could be deployed on wings or other wetted surfaces of the airplane, and controlled by feedback with the aim of reducing drag, preventing transition or controlling separation (see fig. 1.1). Particularly active groups in the research on MEMS devices for a variety of applications, including the aerospace ones, are Ho's group at the UCLA Micro Systems Lab [73; 138; 47] and Kasagi's group at Tokyo University[63].

Leading aerospace industries recognized the potential prospective MEMS technologies that may be applied on civil airplanes in the next 20 years. An example of such feasibility study was given by the Airbus company in 2006, in the KAT-Net framework [124]: this study shows that viscous drag constitutes the most relevant part of the total drag of a civil airplane, and it is also the most likely to be reduced in the near future, by employing turbulence and separation control technologies (see fig. 1.2). Moreover, it has recently been highlighted by the U.S. Committee on Theoretical and Applied Mechanics [44] that the fundamental understanding of the turbulence problem as well as the development of flow control technology are two out of the five research areas expected to be most influential to the enhancement of industry in the future. As an example, it has been estimated that reduction of skin friction drag by 10% could result in 10 billion dollars saving per year for shipping industry. This confirms the scientific and industrial relevance of the turbulence and flow control problems, and the aeronautical industry is leading the global research efforts in this direction.

Design of feedback controllers for turbulent fluid flows is on the very edge of engineering research and it's challenging under many respects. The turbulent flow

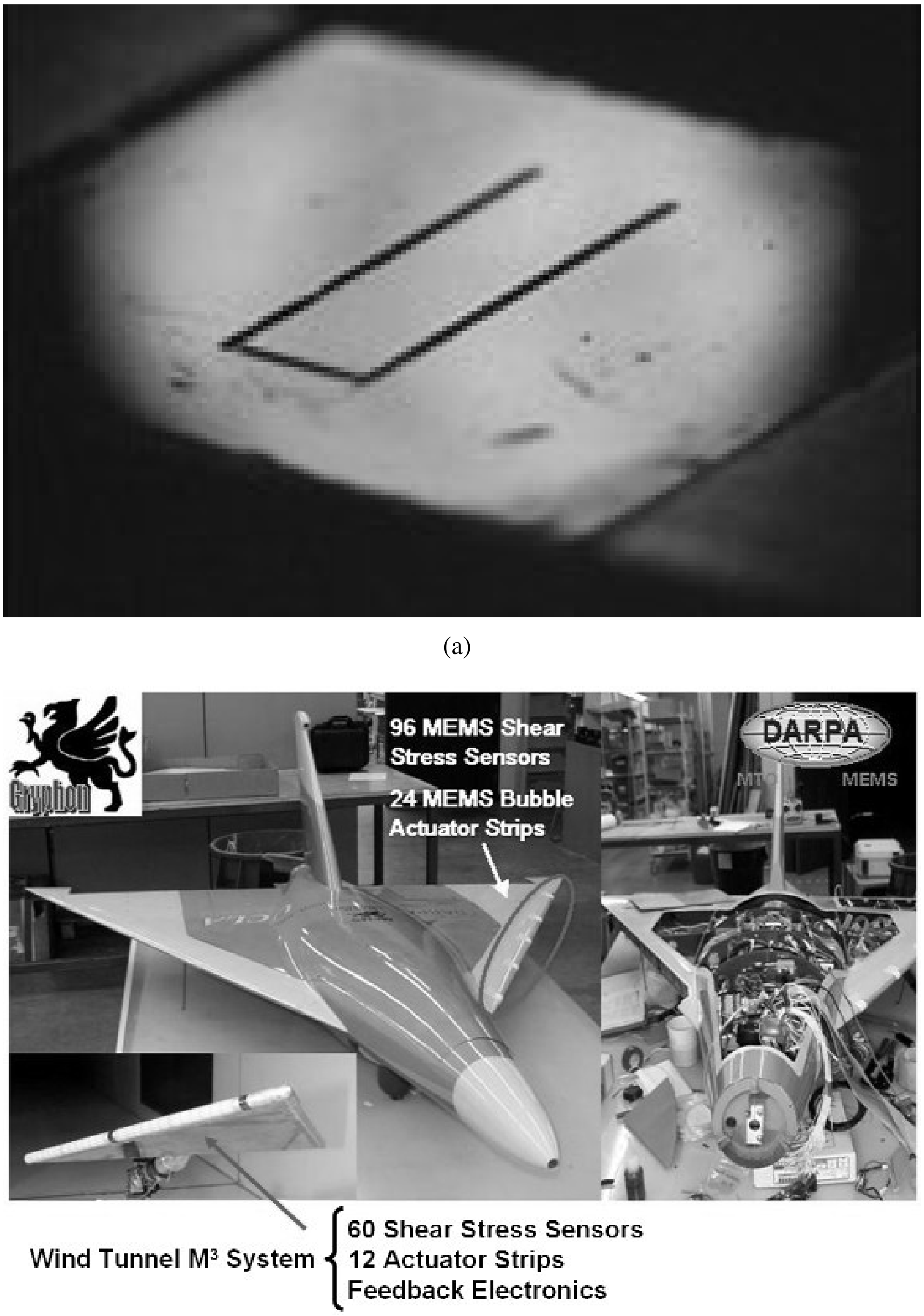

(a)

(b)

Figure 1.1: (a) MEMS actuator for boundary layer control; this is a cantilever beam having size $3 \times 1\,mm$ and $50\,\mu m$ thickness. (b) An example application of MEMS actuators in vortex shedding control on a delta wing. From [47].

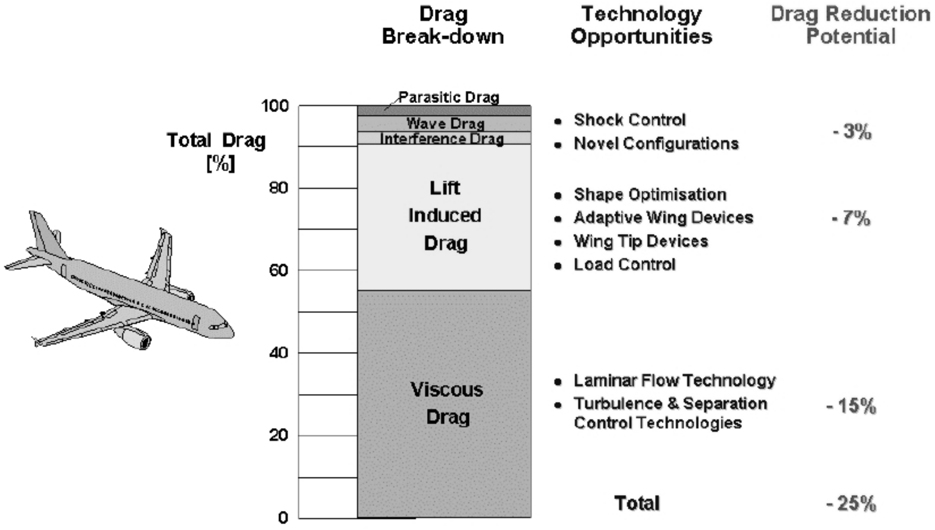

Figure 1.2: Drag breakdown for a civil airliner, and reduction potential in the foreseeable future, on the basis of available flow control technologies. From [124].

over a wall is a distributed parameter system governed by nonlinear partial differential equations. System analysis must be performed with the help of efficient numerical techniques, and Direct Numerical Simulation (DNS) of turbulent wall flows – where the full nonlinear equations are numerically integrated resolving all the scales of the turbulent motions without subgrid-scale modeling – is a key ingredient. Furthermore, control theory has been mostly developed for low-order, linear, lumped-parameter systems such as the electromechanical ones; therefore, most available theoretical and numerical techniques turn out not to be well-suited for the controller synthesis in high-dimensional problems. These features make the control of turbulence interesting both for the fluid dynamicist and the control designer: challenges may well lead to substantial developments in both fields. The multidisciplinary blend of fluid dynamics, control theory and numerical mathematics is a fairly recent subject which is growing quickly, and becoming increasingly known as *flow control* [10].

1.2 Turbulent drag reduction

Turbulent drag reduction by means of *passive* devices has been employed with some success in the past. A notable example is the application of "riblets" (wall grooves on the wetted surfaces) aligned with the mean flow direction [135; 27; 5; 25; 6]. Such devices have the capability of weakening the turbulent wall cycle, leading to drag reduction up to 10% when optimal size is used. In aeronautical application, the typical optimal dimension at $Re \approx 10^6$ is $h \approx 30\mu m$. Despite the initial research and industrial interest in the 80's and 90's, such devices have been abandoned because they are fragile and particularly sensitive to dust, and they are particularly expensive to produce due to the micromachining procedure required. However, a recent renewed interest in riblets led to the design of a second generation of *sinusoidal* riblets [103].

A second important example of drag reduction technique is polymer injection in turbulent boundary layers [134; 82; 83; 33], mostly employed in internal flows such as in oil ducts. Polymer additives change the physical properties of the flow; more specifically, long-chain macromolecule polymers interact with the flow by damping fluctuations in the buffer layer, where turbulent production is maximum. Polymer injection can lead to drag reduction up to 80%, but clearly it is not applicable in the aerospace industry.

A final, noteworthy example of passive drag-reducing devices are compliant coatings; these are viscoelastic surfaces capable of favourably interacting with the flow when deformations due to skin friction and pressure occur. The initial, positive results of Kramer [68] in 1957 – where drag reduction up to 50% in a turbulent boundary layer was obtained – were not confirmed by following investigators [19]. These conflicting results led to important theoretical developments, especially focused on the stability of the fully coupled hydro-viscoelastic problem [21; 22]. The application of compliant coatings in turbulent boundary layers has been recently revisited [29] and shown to provide up to 7% in water flows.

Turbulent drag may be reduced by employing active *feedforward* techniques; see [40] for a comprehensive review. A noteworthy drag reduction strategy is the use of spanwise wall oscillations to partially suppress the turbulent wall cycle [61; 28]. It has been shown that turbulent channel flows are particularly sensitive to such wall movements, and that there exist optimal oscillation amplitude and frequency that provide a maximum drag reduction; moreover, optimal amplitude and frequency have been found that provide the maximum net power saving [107; 104; 114; 113; 115]. A recent and interesting extension of this technique is the use of streamwise-traveling waves of spanwise velocity at the channel wall [101; 105].

1.3 Turbulent drag reduction by feedback

Most of the recent attempts in the control of wall turbulence have considered either incompressible turbulent boundary layer or channel flow as model problems. These flows are amenable to efficient DNS, and possess all the relevant features of generic wall flows, such as those over wing surfaces. Most of the available results have been obtained numerically - at the relatively low to moderate Reynolds numbers attainable by DNS - with the purpose of establishing the feasibility of feedback drag reduction strategies.

While theoretical understanding of turbulent flow control is still at an early stage, its experimental implementation – that additionally requires significant advances in MEMS technology – is perhaps even more on its infancy. A very first attempt in feedback control of wall turbulence has been performed via *numerical simulations* by Choi et al. [26; 45]. They considered a turbulent channel flow, and introduced the concept of "opposition control": they applied, at each time instant, a boundary wall-normal velocity opposite to the one measured in some wall-parallel plane in the near-wall region. This simple control law, based on a physical intuition about the dynamics of the self-sustaining cycle of wall turbulence [59; 95], led to drag reduction up to 25%, with a net energy saving. After this first success, several developments in the control of wall turbulence followed. First, the fundamental theory of flow control [1; 13; 65; 16]. Secondly, on the more practical side, effective strategies to control turbulence have been actively investigated. Among the approaches relying on wall-based actuation, the work of Bewley & coworkers [89; 12; 11; 50] and Kim & coworkers [60; 72; 74; 64; 31; 76] led to significant results. These groups introduced control techniques based on modern optimal control theory, which constitutes a rigorous mathematical framework for linear time-invariant (LTI) systems described in state-space form. These efforts stimulated fundamental research in the field of reduced-order modeling for very high-dimensional systems, as well as the interesting quest for sustained sublaminar drag in channel flow [88; 11; 54; 78; 10; 14], which is still an open issue. Flow control techniques based on modern optimal control theory are nowadays well established and can be referred to as "the standard approach".

Alternative approaches, based on the use of system identification techniques, have been used in the past, notably by employing neural networks for the dynamic inversion of the system under control [35; 71]. These approaches are particularly appealing since they can provide nonlinear control laws accounting for the nonlinearity of the process; moreover, they rely on design techniques that do not require an accurate physical modeling, since the input-output relation of the system is identified and accounted for in real-time. Different actuation techniques have also been explored, in particular employing actuations with body forces, generally created by means of electric or magnetic fields [9; 18; 94]. Despite the potential of such actuators, usually an electrically conducting working fluid is required, thus excluding aeronautical applications. A notable exception is the use of plasma actuators to modify the flowfield over airfoils at high angle of attack, in order to prevent separation [100].

The actual use of optimal controllers requires filters capable of real-time providing a reliable state-estimate. The problem of real-time reconstruction of the flow state using wall-based measurements is of utmost importance, and however not well understood yet. Starting from the seminal attempts in [26], a state estimation framework has been developed for transitional [51] and turbulent [24] flows by the KTH group; this group developed advanced estimation and control strategies for boundary layer flows [117]. However, up to present it is still unclear whether or not linear estimation provides a sufficiently accurate estimate of the flow near a wall – on the basis of wall measurements only – with respect to nonlinear estimation strategies.

A very first *experimental* attempt in the use of MEMS actuators to control a turbulent boundary layer was presented by Tsao et al. [132]. MEMS sensors for wall pressure measurements (typically in the form of small flexible membranes) and shear stress measurements (floating elements, hot films and piezoelectric sensors) have been developed at the end of the 80's and the beginning of the 90's [46; 92; 2]. In the same period, a variety of actuation strategies have been proposed and tested, most notably the use of small cavities from which the fluid is pumped out by means of a micro cantilever beam [69; 56], by using either electrostatic forces or acoustic speakers [17; 87], or forcing with synthetic jets [108].

1.4 Review of fundamental notions

Most of the well-established design and synthesis techniques used in flow-control applications require the availability of a *linear model* of the system to be controlled. The model is usually obtained from the mathematical description of the physical system under consideration; in the present case of incompressible channel flow, this leads to nonlinear partial differential equations with constant coefficients. These equations can be linearized about a reference solution, and upon spatial discretization a constant-coefficients system of ordinary differential equations in time can be obtained.

The state-space form of the governing equations of a LTI system may be written as

$$\begin{aligned} \dot{x} &= Ax + Bu + n \\ y &= Cx + d \end{aligned} \tag{1.1}$$

where $x \in \mathbb{C}^n$ is the state vector, $u \in \mathbb{C}^m$ is the input vector, and $y \in \mathbb{C}^p$ is the output vector. The system matrix $A \in \mathbb{C}^{n \times n}$ describes the dynamics of the unforced system; matrix $B \in \mathbb{C}^{n \times m}$ accounts for the effect of the inputs on the state equation, while matrix $C \in \mathbb{C}^{p \times n}$ defines the measuring capability of sensors. The vector $n \in \mathbb{C}^n$ represents a *noise* on the state equations, that may be used to partially reintroduce the effect of the unmodeled dynamics into the system; finally, the vector $d \in \mathbb{C}^p$ represents a measurement *disturbance*, that accounts for the (always present) disturbances in measurement systems. Note that, in standard textbooks on control theory, there is no need to let the entries in (1.1) be complex-valued, since physical systems are real; this extension is employed here since, in Chap. 2, a particular mathematical model will be introduced that require a complex representation of the system dynamics.

A block diagram of the system defined by (1.1) is reported in fig. 1.3. We refer to the *impulse response* function of the system in (1.1) as the function given by the

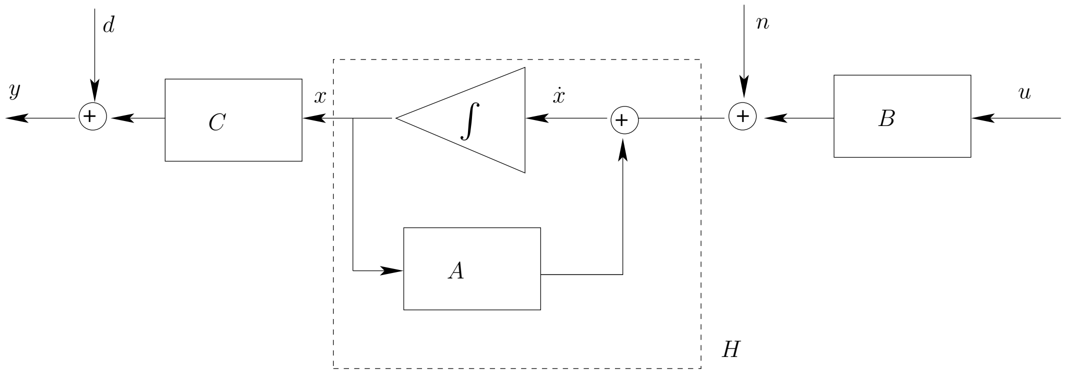

Figure 1.3: Block diagram of the state-space model defined in (1.1).

matrix exponential[1]

$$h(t) = \begin{cases} e^{At}, & t \geq 0 \\ 0, & t < 0 \end{cases} \tag{1.2}$$

Note that the definition in (1.2) is that of a *causal* function; this mathematical statement accounts for the property of physical systems not to depend on their future dynamics, inputs, or disturbances. Taking the bilateral Laplace's transform of (1.2) one obtains the system's *transfer function* matrix:

$$H(s) = \int_{-\infty}^{+\infty} h(t)e^{-st}\,dt, \qquad s = \sigma + j2\pi f. \tag{1.3}$$

It is important to notice [62] that the transfer function $H(s)$ of an asymptotically stable causal system is regular in the closed right half of the complex plane. In fact, asymptotic stability implies that the generic element (m,n) of the impulse response matrix will be bounded by:

$$|h_{m,n}(t)| \leq \kappa e^{-ct}, \qquad \kappa, c \in \mathbb{R}^+, t > 0, \quad \forall m,n.$$

In turn, this translates into a condition on the corresponding element of the transfer function matrix (note that the lower bound in the integral sign has been changed to 0 because of the causality constraint):

$$|H_{m,n}(s)| \leq \int_0^{+\infty} e^{-(\sigma+c)t}\,dt \qquad \forall m,n$$

and then there exists a constant c such that $H(s)$ is regular for $\sigma > -c$. The restriction of the transfer function $H(s)$ on the imaginary axis corresponds to the Fourier

---

[1] Usually, the impulse response of a system is referred to an input-output relation; in this work, when considering response functions different from that defined in this chapter, the respective inputs and outputs will be made clear by the context.

transform of $h(t)$, and is referred to as the *frequency response* function $H(f)$:

$$H(f) = \int_{-\infty}^{+\infty} h(t)e^{-j2\pi ft}\,dt. \tag{1.4}$$

It is customary to refer to complex functions – defined on the imaginary axis – that are restriction of complex functions regular in the closed right half plane, as *plus functions*. Accordingly, the frequency response in (1.4) may be denoted by $H_+(f)$. Likewise, complex functions that are restriction of functions regular in the closed left half plane will be referred to as *minus functions*, and denoted by a $-$ subscript accordingly.

Once a linear model of the system is available (note that this includes the knowledge of matrices B and C - corresponding to actuators and sensors - whose definition is normally up to the control designer), a control objective must be stated before moving to the control design. Among the various possibilities, we shall be restricted to the design of LTI compensators that minimize a certain *objective functional*; this approach is typical of optimal control theory, and it is pursued herein. Typically, objective functionals to be minimized are expressed in terms of statistics of some quadratic form of the state and the input vectors. Therefore, in the following a brief review of fundamental results in statistics that are relevant to the present context is provided; a thorough treatment of these notions can be found in [7] or [96].

A most relevant quantity that will be used throughout this work is the *autocorrelation* function $K_{xx}(t,\tau)$ of a complex-valued, zero-mean vector process x, a matrix defined as

$$K_{xx}(t,\tau) = E\{x(t+\tau)x^H(t)\}$$

where $E\{\cdot\}$ denotes the expectation operator and the superscript H denotes conjugate transpose. When the process x is statistically weakly stationary, the autocorrelation function does not depend explicitly on t and its definition reduces to

$$K_{xx}(\tau) = E\{x(t+\tau)x^H(t)\}.$$

If the ergodicity assumption holds, the following time-averaging operator can be defined (the "Mean Integral operator"):

$$\int\!\!\!\!\!\!M \cdot dt = \lim_{T\to+\infty} \frac{1}{T}\int_{-T/2}^{T/2} \cdot\, dt,$$

and used to express the autocorrelation as:

$$K_{xx}(\tau) = \int\!\!\!\!\!\!M x(t+\tau)x^H(t)\,dt \tag{1.5}$$

The *spectral density* function $\phi_{xx}(f)$ of a weakly stationary, complex valued, zero-mean vector process x is defined as the Fourier transform of its autocorrelation function:

$$\phi_{xx}(f) = \int_{-\infty}^{+\infty} K_{xx}(\tau)e^{-j2\pi f\tau}\,d\tau. \tag{1.6}$$

The spectral density function plays a central role in the analysis of LTI systems in presence of stationary noises. In particular, given a multiple-input, multiple-output system having impulse response matrix $g(t)$, input $u(t)$ and output $y(t)$, the spectral density function of the output is expressed as a function of the input spectral density as:

$$\phi_{yy}(f) = G(f)\phi_{uu}(f)G^H(f). \tag{1.7}$$

Expressions in (1.5) and (1.6) are straightforwardly extended to define the *cross-correlation* function and the *cross-spectral density* function.

Chapter 2

Standard approach to flow control

After a brief presentation of the model problem considered in this work, this chapter addresses the “standard approach” to turbulent flow control. The basic theory of optimal control and filtering is briefly reviewed; furthermore, control and estimation kernels - similar to those reported in the recent literature - are presented. The interested reader is referred to the recent review of Kim & Bewley [65] for a more detailed presentation, as well as a description of the adjoint-based approach to control design, which is omitted here. The chapter closes with a discussion of the fundamental results obtained with the standard approach; moreover advantages and drawbacks of this formulation are critically discussed, emphasizing open issues to be addressed in subsequent chapters.

2.1 A model problem: turbulent channel flow

We consider the incompressible turbulent flow between two plane parallel walls. This flow is amenable to very efficient Direct Numerical Simulation (DNS) at moderate Reynolds numbers, and shows all the features of more complex wall flows. The computational domain Ω is depicted in fig. 2.1. A Cartesian coordinate system is introduced, where x, y, z, denote the streamwise, wall-normal and spanwise directions, respectively; the dimensions of the finite computational domain are L_x, 2δ and L_z, respectively. The velocity field is denoted by $\mathbf{V}(x, y, z)$, and its components in the coordinate directions are U, V, W, whereas the pressure field is denoted by $P(x, y, z)$; velocity and pressure perturbations fields are denoted by lowercase letters. The governing Navier–Stokes equations for an incompressible fluid flow:

$$\begin{cases} \nabla \cdot \mathbf{V} = 0 \\ \dfrac{\partial \mathbf{V}}{\partial t} + (\mathbf{V} \cdot \nabla)\mathbf{V} = -\nabla P + \dfrac{1}{Re}\Delta \mathbf{V} \\ + \qquad \text{initial and boundary conditions,} \end{cases} \tag{2.1}$$

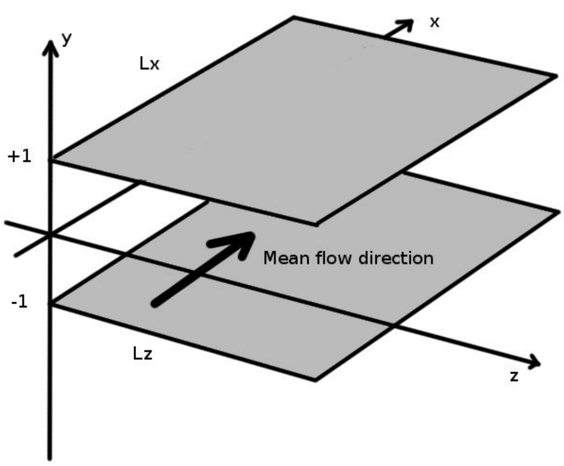

Figure 2.1: Computational domain Ω of the problem.

express conservation of mass and momentum; they are made nondimensional with the bulk velocity and the channel half width, so that $Re = \frac{U_b \delta}{\nu}$ is the corresponding Reynolds number, where ν is the fluid kinematic viscosity.

In the conventional approach to channel flow control (see, for instance, Chevalier et al. [24]), the system (2.1) of governing equations is rewritten in terms of nonlinear perturbations about a reference streamwise velocity profile $\overline{u}(y)$ (for instance, the mean turbulent profile), defined as:

$$\overline{u}(y) = \frac{1}{L_x L_z} \int_0^{L_x} \int_0^{L_z} \int M \, U(x, y, z, t) \; dtdzdx. \tag{2.2}$$

In such a case, the wall-normal velocity - wall-normal vorticity ($v - \eta$) formulation can be exploited [67]:

$$\begin{cases} \dfrac{\partial \Delta v}{\partial t} + \overline{u} \dfrac{\partial}{\partial x} \Delta v - \overline{u}'' \dfrac{\partial v}{\partial x} - \dfrac{1}{Re} \Delta\Delta v = h_v \\ \dfrac{\partial \eta}{\partial t} + \overline{u}' \dfrac{\partial v}{\partial z} + \overline{u} \dfrac{\partial \eta}{\partial x} - \dfrac{1}{Re} \Delta \eta = h_\eta \end{cases} \tag{2.3}$$

where $\eta = \partial u / \partial z - \partial w / \partial x$. The nonlinear terms h_v and h_η are:

$$h_v = \frac{\partial}{\partial y} \Big\{ \frac{\partial}{\partial x} \Big[\frac{\partial (uu)}{\partial x} + \frac{\partial (uv)}{\partial y} + \frac{\partial (uw)}{\partial z} \Big] + \frac{\partial}{\partial y} \Big[\frac{\partial (vu)}{\partial x} + \frac{\partial (vv)}{\partial y} + \frac{\partial (vw)}{\partial z} \Big] + \dots$$

$$\dots + \frac{\partial}{\partial z} \Big[\frac{\partial (wu)}{\partial x} + \frac{\partial (wv)}{\partial y} + \frac{\partial (ww)}{\partial z} \Big] \Big\} - \Delta \Big[\frac{\partial (vu)}{\partial x} + \frac{\partial (vv)}{\partial y} + \frac{\partial (vw)}{\partial z} \Big],$$

$$h_\eta = \frac{\partial}{\partial x} \Big[\frac{\partial (wu)}{\partial x} + \frac{\partial (wv)}{\partial y} + \frac{\partial (ww)}{\partial z} \Big] - \frac{\partial}{\partial z} \Big[\frac{\partial (uu)}{\partial x} + \frac{\partial (uv)}{\partial y} + \frac{\partial (uw)}{\partial z} \Big].$$

The use of the $v - \eta$ formulation implicitly enforces the continuity constraint, by projecting the velocity field on a divergence-free manifold. This formulation highlights the two degrees of freedom of the mathematical problem, and provides the minimal set of state variables required; therefore, this set of variables is a natural choice in the control design framework, and will be used throughout the entire thesis.

It is useful to exploit the spatial invariance of the problem with respect to translations in x and z by introducing a Fourier series expansion in these directions; for instance, for the v perturbation velocity component:

$$v(x,y,z,t) = \sum_{n_x=-N_x}^{N_x} \sum_{n_z=-N_z}^{N_z} \hat{v}(n_x,y,n_z,t) e^{j\frac{2\pi n_x x}{L_x}} e^{j\frac{2\pi n_z z}{L_z}},$$

where the Fourier coefficients (denoted by hats) satisfy:

$$\hat{v}(n_x,y,n_z,t) = \frac{1}{L_x L_z} \int_0^{L_x} \int_0^{L_z} v(x,y,z,t) e^{-j\frac{2\pi n_x x}{L_x}} e^{-j\frac{2\pi n_z z}{L_z}} \, dz dx.$$

Defining the streamwise and spanwise wavenumbers $\alpha = \frac{2\pi n_x}{L_x}$ and $\beta = \frac{2\pi n_z}{L_z}$, and defining $\alpha_m = \frac{2\pi N_x}{L_x}$ and $\beta_m = \frac{2\pi N_z}{L_z}$, the Fourier series expansion can be rewritten more compactly as

$$v(x,y,z,t) = \sum_{\alpha=-\alpha_m}^{\alpha_m} \sum_{\beta=-\beta_m}^{\beta_m} \hat{v}(\alpha,y,\beta,t) e^{j(\alpha x + \beta z)}.$$

After Fourier transform, equations (2.3) become:

$$\begin{cases} \dfrac{\partial}{\partial t}\hat{\Delta}\hat{v} + j\alpha\overline{u}\hat{\Delta}\hat{v} - j\alpha\overline{u}''\hat{v} - \dfrac{1}{Re}\hat{\Delta}\hat{\Delta}\hat{v} = \hat{h}_v \\ \dfrac{\partial}{\partial t}\hat{\eta} + j\beta\overline{u}'\hat{v} + j\alpha\overline{u}\hat{\eta} - \dfrac{1}{Re}\hat{\Delta}\hat{\eta} = \hat{h}_\eta \end{cases} \tag{2.4}$$

so that the system (2.3) can be rewritten in matrix form, for each wavenumber pair, as in [24]:

$$\frac{d}{dt} M\hat{q} + L\hat{q} = \hat{h} \qquad \forall \alpha, \beta \tag{2.5}$$

where

$$\hat{q} = \begin{pmatrix} \hat{v} \\ \hat{\eta} \end{pmatrix} \qquad M = \begin{pmatrix} \hat{\Delta} & 0 \\ 0 & I \end{pmatrix} \qquad L = \begin{pmatrix} \mathbf{L} & 0 \\ \mathbf{C} & \mathbf{S} \end{pmatrix} \qquad \hat{h} = \begin{pmatrix} \hat{h}_v \\ \hat{h}_\eta \end{pmatrix}$$

and

$$\begin{aligned} \mathbf{L} &= j\alpha\overline{u}\hat{\Delta} - j\alpha\overline{u}'' - \hat{\Delta}\hat{\Delta}/Re \\ \mathbf{C} &= j\beta\overline{u}' \\ \mathbf{S} &= j\alpha\overline{u} - \hat{\Delta}/Re. \end{aligned}$$

2.2 Linearized model

Equations (2.5) inherit the nonlinearity of the governing equations (2.1); in fact, evolution equations for each wavenumber pair are coupled with each other by the nonlinear term $\hat{h}$ on the right hand side, accounting for nonlinear triadic interactions.

In order to obtain a linear model of the flow from (2.5), an *ad hoc* procedure has been proposed in [24]. Nonlinear terms on the right hand side in (2.5) are neglected and replaced with a *noise* $\hat{r}$ with the same first and second order statistics of $\hat{h}$. In this way, the equations become linear, but the *effect* of nonlinearity is partially accounted for as the effect of a noise on the state (i.e. a modeling error). Specifically, $E\{\hat{r}\} = E\{\hat{h}\} = 0$, and the autocorrelation function of $\hat{r}$ is given by

$$R_{\hat{r}\hat{r}}(y_1, y_2, \tau; \alpha, \beta) = E\{\hat{h}(y_1, t+\tau; \alpha, \beta)\hat{h}^H(y_2, t; \alpha, \beta)\}.$$

Note that, since $\hat{h} = \hat{h}(y, t)$ (for each wavenumber pair) and y is a non homogeneous direction, the autocorrelation function explicitly depends on the two wall-normal positions. The final form of the governing equations reads

$$\frac{d}{dt}M\hat{q} + L\hat{q} = \hat{r}, \qquad \forall\alpha, \beta. \tag{2.6}$$

Once this procedure is performed, eq. (2.6) provides a linear model of the system at hand, represented by a parametric family of partial differential equations in y and t, parametrized by the wavenumber couple (α, β).

2.2.1 Wall actuation

Accounting for wall blowing/suction velocity in the $v - \eta$ form of the equations is rather tricky, since time-dependent boundary conditions on $\hat{v}$ affect both $\hat{v}$ and $\dot{\hat{v}}$ in (2.6). After a few initial incorrect attempts [15; 76], it has been recognized that the appropriate way to account for the nonhomogeneous wall forcing was to use a lifting procedure [49; 85]. For example, if actuation is performed on the wall at $y = -1$, boundary conditions for (2.6) are:

$$\begin{aligned} \hat{v}(\alpha, -1, \beta, t) &= \hat{v}_w(\alpha, \beta, t) \\ \frac{\partial \hat{v}}{\partial y}(\alpha, -1, \beta, t) &= 0 \\ \hat{\eta}(\alpha, -1, \beta, t) &= 0 \end{aligned}$$

where $\hat{v}_w(\alpha, \beta, t)$ represents, for each wavenumber pair, the wall blowing-suction intensity to be used in feedback control. The homogeneous problem with inhomogeneous boundary conditions is transformed into a nonhomogeneous problem with homogeneous boundary conditions. To this aim, the following splitting is introduced:

$$\hat{q} = \hat{q}_h + \hat{q}_p$$

where $\hat{q}_p$ is chosen to account for inhomogeneous boundary conditions on $\hat{v}$, and satisfies the diffetential problem $\mathbf{L}\hat{q}_p = 0$. It is convenient to choose the particular solution $\hat{q}_p$ as a separable function:

$$\hat{q}_p(y,t) = \hat{g}(y)\hat{v}_w(t).$$

Solution of the two-point boundary value problem with homogeneous Dirichlet boundary conditions for $\dot{\hat{v}}_h$ leads to

$$\frac{d}{dt}\hat{q}_h = -M^{-1}L\hat{q}_h - M^{-1}(M\hat{g})\dot{\hat{v}}_w + M^{-1}\hat{r}$$

It is convenient to introduce the auxiliary state $\hat{v}_w$, obtaining the state-space form of the equations as in (1.1):

$$\underbrace{\frac{d}{dt}\begin{pmatrix}\hat{q}_h\\ \hat{v}_w\end{pmatrix}}_{\dot{x}} = \underbrace{\begin{pmatrix}-M^{-1}L & 0\\ 0 & 0\end{pmatrix}}_{A}\underbrace{\begin{pmatrix}\hat{q}_h\\ \hat{v}_w\end{pmatrix}}_{x} + \underbrace{\begin{pmatrix}-M^{-1}(M\hat{g})\\ I\end{pmatrix}}_{B}\underbrace{\dot{\hat{v}}_w}_{u} + \underbrace{\begin{pmatrix}M^{-1}\hat{r}\\ 0\end{pmatrix}}_{n} \tag{2.7}$$

Note that a natural outcome of this procedure is the fact that actuation is dictated by the rate of change of wall-normal velocity at the walls, instead of wall-normal velocity itself.

2.2.2 Output equations

Output relations are obtained by recalling that the wall-normal velocity and vorticity fields can be written as:

$$\begin{pmatrix}\hat{v}\\ \hat{\eta}\end{pmatrix} = \begin{pmatrix}\hat{v}_h\\ \hat{\eta}_h\end{pmatrix} + \begin{pmatrix}g_v\\ g_\eta\end{pmatrix}\hat{v}_w.$$

Introducing appropriate differentiation operators D_1, D_2 and D_3, wall shear stresses and wall pressure may be written as:

$$\begin{aligned}
\hat{\tau}_{x_w} &= \frac{j}{Re\,k^2}[\alpha D_2 \quad -\beta D_1]\begin{pmatrix}\hat{v}\\ \hat{\eta}\end{pmatrix}\Big|_{y=\pm 1}\\
\hat{\tau}_{z_w} &= \frac{j}{Re\,k^2}[\beta D_2 \quad \alpha D_1]\begin{pmatrix}\hat{v}\\ \hat{\eta}\end{pmatrix}\Big|_{y=\pm 1}\\
\hat{p}_w &= \frac{1}{Re\,k^2}[D_3 \quad 0]\begin{pmatrix}\hat{v}\\ \hat{\eta}\end{pmatrix}\Big|_{y=\pm 1}.
\end{aligned}$$

These equations, written in terms of the state vector x, lead to the output relation

$$y = Cx + d \tag{2.8}$$

where the term d has been added to account for possible measurement disturbances, always present in any practical setting.

2.3 Norms of the state

In the system analysis and control design, it is important to measure the "magnitude" of the state in a physically relevant fashion. To this aim, we introduce here two possible norms, namely, kinetic energy norm and rate of dissipation norm. The former has been thoroughly used in previous works on turbulence control [12], while the latter is used in the flow control setting first in the present thesis.

2.3.1 Energy norm

The kinetic energy of the flow per unit mass is defined as

$$\mathbf{E} = \frac{1}{2\Omega}\int_{\Omega}(U^2+V^2+W^2)\,d\Omega$$

and may be rewritten in terms of $\hat{v}$ and $\hat{\eta}$ by applying the continuity equation, the definition of η, and Parseval's identity:

$$\begin{aligned}\mathbf{E} = \sum_{\alpha,\beta}\frac{1}{4}\int_{-1}^{1}(|\hat{U}|^2+|\hat{V}|^2+|\hat{W}|^2)\,dy = \\ \sum_{(\alpha,\beta)\neq(0,0)} E(\alpha,\beta) + \frac{1}{4}\int_{-1}^{1}(|\hat{U}_{(0,0)}|^2+|\hat{W}_{(0,0)}|^2)\,dy\end{aligned} \qquad (2.9)$$

where

$$E(\alpha,\beta) = \frac{1}{4k^2}\int_{-1}^{1}\Big(k^2|\hat{v}|^2 + |\frac{\partial\hat{v}}{\partial y}|^2 + |\hat{\eta}|^2\Big)\,dy$$

Owing to the orthogonality of Fourier modes, the contributions to the total energy from each wavenumber pair are decoupled.

Given the state variables of the system at hand, as in (2.7), it is straightforward to rewrite $E(\alpha,\beta)$ as a quadratic function of the state vector x, as follows:

$$E(\alpha,\beta) = x^H Q_E x = \|x\|_E \qquad (2.10)$$

where Q_E is an hermitian, positive definite matrix.

2.3.2 Dissipation norm

Another physically grounded norm of the state may be derived by noticing that, in statistically stationary conditions, the average skin friction drag in a turbulent channel flow equals the average rate of dissipation of turbulent kinetic energy. In fact, let us consider the governing Navier-Stokes equations written using indicial notation and implying summation convention:

$$\frac{\partial U_i}{\partial t} + \frac{\partial}{\partial x_j}(U_iU_j) = -\frac{\partial P}{\partial x_i} + \frac{1}{Re}\frac{\partial^2 U_i}{\partial x_k\partial x_k} - \overline{P}_x\delta_{1i}$$

Here, $\overline{P}_x$ is the mean longitudinal pressure gradient driving the flow against viscous shear stresses. The above equation, after scalar multiplication by U_i, application of the continuity equation and integration on the domain Ω, may be rewritten as

$$\frac{d}{dt}\int_\Omega \frac{U_iU_i}{2}\,d\Omega + \int_\Omega \frac{\partial}{\partial x_j}(U_j\frac{U_iU_i}{2})\,d\Omega + \int_\Omega \frac{\partial(PU_i)}{\partial x_i}\,d\Omega =$$
$$= \frac{1}{Re}\int_\Omega \frac{\partial}{\partial x_k}(U_i\frac{\partial U_i}{\partial x_k})\,d\Omega - \frac{1}{Re}\int_\Omega \frac{\partial U_i}{\partial x_k}\frac{\partial U_i}{\partial x_k}\,d\Omega - \int_\Omega \overline{P}_x U_i \delta_{1i}\,d\Omega$$

Applying periodic boundary conditions in homogeneous directions and homogeneous boundary conditions at the channel walls, and applying the divergence theorem, one obtains:

$$\frac{d}{dt}\int_\Omega \frac{U_iU_i}{2}\,d\Omega + \frac{1}{Re}\int_\Omega \frac{\partial U_i}{\partial x_k}\frac{\partial U_i}{\partial x_k}\,d\Omega = -\int_\Omega \overline{P}_x U_1\,d\Omega$$

Ensemble averaging of the above equations, and considering statistically stationary conditions, yields:

$$\overline{P}_x = \frac{1}{Re}\frac{d\langle U\rangle}{dy}\Big|_w = -\frac{1}{U_B\Omega Re}\Big\langle \int_\Omega \frac{\partial U_i}{\partial x_k}\frac{\partial U_i}{\partial x_k}\,d\Omega\Big\rangle$$

Fourier expansion in homogeneous directions leads to:

$$\frac{d\langle U\rangle}{dy}\Big|_w = -\frac{1}{U_B}\Big\langle \sum_{(\alpha,\beta)\neq(0,0)} D(\alpha,\beta) + \underbrace{\frac{1}{2}\int_{-1}^{1}\Big(\frac{\partial\hat{U}}{\partial y}\Big)_{(0,0)}\Big(\frac{\partial\hat{U}}{\partial y}\Big)^*_{(0,0)}dy}_{D_{mean}}\Big\rangle$$

where

$$D(\alpha,\beta) = \frac{1}{2}\int_{-1}^{1}\Big[\hat{\eta}^*\hat{\eta} + 2\frac{\partial\hat{v}^*}{\partial y}\frac{\partial\hat{v}}{\partial y} + k^2\hat{v}^*\hat{v} + \frac{1}{k^2}\frac{\partial\hat{\eta}^*}{\partial y}\frac{\partial\hat{\eta}}{\partial y} + \frac{1}{k^2}\frac{\partial^2\hat{v}^*}{\partial y^2}\frac{\partial^2\hat{v}}{\partial y^2}\Big]\,dy \quad (2.11)$$

is the contribution - at a given wavenumber pair - to the total dissipation pertaining to turbulent fluctuations, and D_{mean} is the contribution due to the mean flow.

Given the state variables of the system at hand, as in (2.7), it is straightforward to rewrite $D(\alpha,\beta)$ as a quadratic function of the state vector x, as follows:

$$D(\alpha,\beta) = x^H Q_D x = \|x\|_D \quad (2.12)$$

where Q_D is an hermitian, positive definite matrix.

2.4 Optimal compensator design

The control system design problem for a LTI system given in the form (1.1):

$$\dot{x} = Ax + Bu + n$$
$$y = Cx + d,$$

where the noise n and the disturbance d are weakly stationary, white Gaussian processes having known statistics, is a fundamental problem in control theory.

In general, control of wall turbulence is aimed at reducing certain norms of the flow state, namely, turbulent kinetic energy or dissipation rate. In such cases, the control objective is expressed in the form of a quadratic functional of the state; introducing an additional regularization weight, to account for limited control effort in order to avoid saturation of the actuators, leads to the following *objective functional*:

$$J = E\{x^H Q x + u^H R u\}. \tag{2.13}$$

The problem of minimizing J in (2.13) under the constraint of the state-space equation (1.1) has a well-known solution [36] based on an important *separation theorem*.

It is important to emphasize the difference between the well-known separation *principle* and the specialized separation theorem. The former states that it is possible to design the controller gains as if all states were available, and to design the state observer regardless of the input, thus obtaining a compensator that guarantees closed loop asymptotic stability; however, this statement does not ensures the *optimality* (in the sense of minimizing the functional in (2.13)) of such solution to the control problem. The latter theorem states that, in order to design a feedback compensator minimizing (2.13), given the statistical information on the state and measurement noise, it suffices to separately design the optimal deterministic controller (ignoring the noise) and the Kalman filter to provide the necessary state estimate. Proof of this fundamental theorem is not reported here; the interested reader is referred to the important monograph by Anderson and Moore [3].

The feedback compensator can, therefore, designed via a first step where the feedback control gains are determined; hence, a dynamical system - the state estimator - is designed separately, and it is ensured by the separation theorem that feedback signal computed from the estimated state is optimal in the sense of minimizing the functional in (2.13). The following subsections briefly review these two steps of optimal controller and estimator design; the full procedure is usually referred to as LQG (Linear Quadratic Gaussian) design.

2.4.1 Infinite-horizon optimal control

Consider a LTI system described by the state-space equation

$$\dot{x} = Ax + Bu. \tag{2.14}$$

It is assumed that the couple (A, B) is stabilizable. The infinite-horizon optimal control problem is stated as the search of an optimal control law for the input u, such that the following quadratic functional is minimized:

$$J = \int_0^{+\infty} (x^H Q x + u^H R u)\, dt. \tag{2.15}$$

Q is a positive semidefinite hermitian matrix, weighting the departure of the state from the origin of the state space; R is a positive definite hermitian matrix, corresponding to the weight on the control effort. It is also assumed that the couple $(A, Q^{1/2})$ is detectable.

Introducing a state-proportional control law in the form $u = Kx$, K being a complex gain matrix, the closed-loop system and functional read:

$$\dot{x} = (A + BK)x, \qquad J = \int_0^{+\infty} x^H (Q + K^H RK)x \, dt$$

Given an initial condition x_0, the solution of the closed-loop state-space equation reads

$$x(t) = e^{(A+BK)t} x_0$$

and, substituting in the functional J:

$$J = x_0^H \Big(\int_0^{+\infty} e^{(A+BK)^H t} (Q + K^H RK) e^{(A+BK)t} \, dt \Big) x_0 = x_0^H P(K) x_0.$$

The functional can be rewritten using the properties of the trace operator:

$$J = Tr[PX_0]$$

where the hermitian, positive definite matrix $X_0 = x_0 x_0^H$ is a design parameter characterizing the possible combinations of worst-case initial conditions for the system. Since the closed loop system is asymptotically stable, the matrix $P(K)$ satisfies the following Lyapunov equation:

$$(A + BK)^H P + P(A + BK) + Q + K^H RK = 0 \tag{2.16}$$

The functional J, constrained with the Lyapunov equation (2.16) by means of an appropriate Lagrange multiplier matrix Λ, reads:

$$J = Tr\{PX_0 + \Lambda[(A + BK)^H P + P(A + BK) + Q + K^H RK]\}.$$

Computing the gradient of the constrained functional with respect to P, Λ and K and setting it to zero one obtains

$$\begin{aligned}
\frac{\partial J}{\partial P} &= (A + BK)\Lambda + \Lambda(A + BK)^H + X_0 = 0 \\
\frac{\partial J}{\partial \Lambda} &= (A + BK)^H P + P(A + BK) + Q + K^H RK = 0 \\
\frac{\partial J}{\partial K} &= (\Lambda PB)^H + (\Lambda K^H R)^H = 0
\end{aligned}$$

Note, from the first equation above, that $\Lambda > 0$ since it satisfies a Lyapunov equation where $X_0 > 0$. Hence, from the third equation, one obtains:

$$K = -R^{-1} B^H P \tag{2.17}$$

The matrix P is the so-called stabilizing solution to the following algebraic Riccati equation:

$$PA + A^H P - PBR^{-1}B^H P + Q = 0$$

which is obtained by substituting eq. (2.17) in eq. (2.16).

2.4.2 Basic Kalman filtering theory

The state estimation problem for a LTI system given in the form (1.1):

$$\begin{aligned} \dot{x} &= Ax + Bu + n \\ y &= Cx + d, \end{aligned}$$

where the noise n and disturbance d are uncorrelated *white* Gaussian noise processes with known covariance matrices W_{nn} and W_{dd}, is a *dual* optimal control problem. The observer system is defined as

$$\begin{aligned} \dot{o} &= Ao + Bu + L(y - y_o) \\ y_o &= Co \end{aligned}$$

and the observer gain matrix L is to be designed optimally (in a sense to be defined later). The dynamics of the state estimation error $e = x - o$ is given by

$$\dot{e} = (A - LC)e + n - Ld.$$

The observer is asymptotically stable; consequently, the variance of the state estimation error, denoted by σ^2_{ee}, is given by the following Lyapunov equation:

$$(A - LC)\sigma^2_{ee} + \sigma^2_{ee}(A^H - C^H L^H) + W_{nn} + LW_{dd}L^H = 0 \tag{2.18}$$

The optimal gain matrix L is found by minimizing the variance of the state estimation error, constrained to the Lyapunov equation (2.18).The constrained functional reads:

$$J = Tr\{\sigma^2_{ee} + \Lambda[(A - LC)\sigma^2_{ee} + \sigma^2_{ee}(A^H - C^H L^H) + W_{nn} + LW_{dd}L^H]\},$$

where Λ is a Lagrange multiplier matrix. Computing the gradient of J with respect to Λ, L and σ^2_{ee}, and setting it to zero, one obtains:

$$\begin{aligned} \frac{\partial f}{\partial \Lambda} &= (A - LC)\sigma^2_{ee} + \sigma^2_{ee}(A^H - C^H L^H) + W_{nn} + LW_{dd}L^H = 0 \\ \frac{\partial f}{\partial \sigma^2_{ee}} &= I + \Lambda(A - LC) + (A^H - C^H L^H)\Lambda = 0 \\ \frac{\partial f}{\partial L} &= -C\sigma^2_{ee}\Lambda + W_{dd}L^H\Lambda = 0 \end{aligned}$$

Note that $\Lambda > 0$ since it satisfies the second Lyapunov equation. From the last equation one directly obtains:

$$L = \sigma_{ee}^2 C^H W_{dd}^{-1}. \tag{2.19}$$

The variance of the state estimation error is found from the following Riccati equation:

$$A\sigma_{ee}^2 + \sigma_{ee}^2 A^H - \sigma_{ee}^2 C^H W_{dd}^{-1} C \sigma_{ee}^2 + W_{nn} = 0$$

which is obtained by substituting (2.19) in (2.18).

By analogy with the optimal control problem, it may be noted that the steady Kalman filter, minimizing the variance of the state estimation error, can be obtained from the solution of the optimal control problem on the *dual* system

$$\dot{z} = A^H z + C^H v$$

with a cost function

$$J = \int_0^\infty z^H W_{nn} z + v^H W_{dd} v \, dt$$

and the weight matrices have the meaning of the covariance of the (white) noises on the state and measurement equations.

2.5 Control and estimation kernels

Optimal control and Kalman filtering theory can be applied to the system (2.6) - (2.8) for an array of wavenumber pairs (α, β), thus obtaining a parametric family of control and estimator gains; upon inverse Fourier transformation to physical space, these gains take the form of *convolution kernels* [49].

Examples of control convolution kernels have been computed and are reported in fig. 2.2; figure (a) shows the kernel for the wall-normal velocity v, while figure (b) shows the one for the wall normal vorticity η. These kernels are similar to those reported in [49]. The kernel for the velocity is symmetric with respect to the $x - y$ plane, while the kernel for the vorticity is anti-symmetric.

Examples of estimation kernels have been computed and are reported in fig. 2.3; figure (a) shows the kernel for the wall-normal velocity v, while figure (b) shows the one for the wall normal vorticity η. These kernels are computed assuming that the wall distribution of spanwise skin friction is available; hence, the kernel for the velocity is anti-symmetric and the one for the vorticity is symmetric with respect to the $x - y$ plane.

2.6 Critical discussion

The fundamental results from the application of LQG compensators to turbulent flows for drag reduction were obtained mainly by the groups of Bewley & coworkers

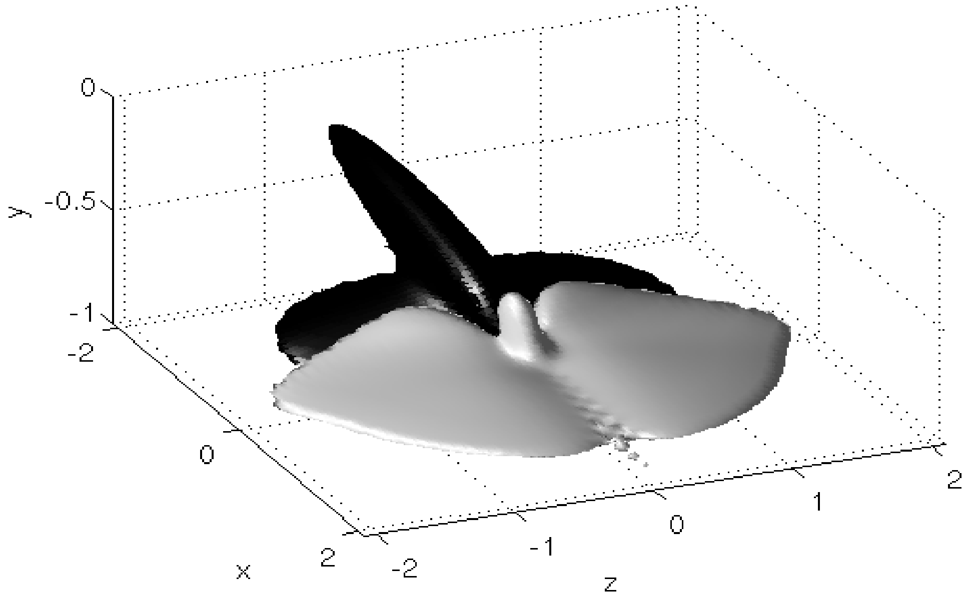

(a)

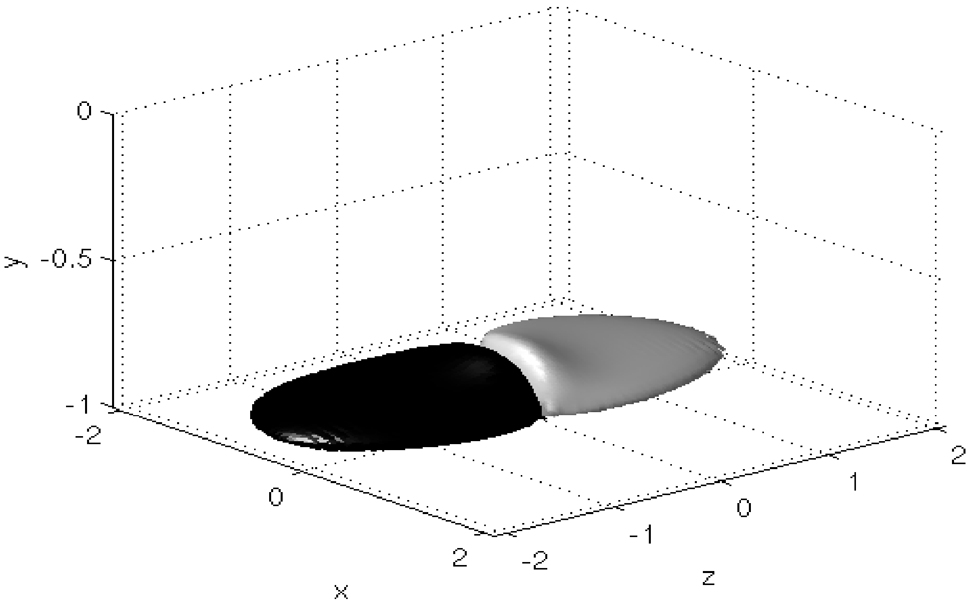

(b)

Figure 2.2: (a) Control convolution kernel for the wall-normal velocity v; negative (black) and positive (light gray) isosurfaces at $\pm 0.5\%$ of the maximum. (b) Control convolution kernel for the wall-normal vorticity η: negative (black) and positive (light gray) isosurfaces at $\pm 3\%$ of the maximum. These kernels relate the instantaneous flow state, in terms of wall-normal velocity and wall-normal vorticity, to the instantaneous control action at the wall.

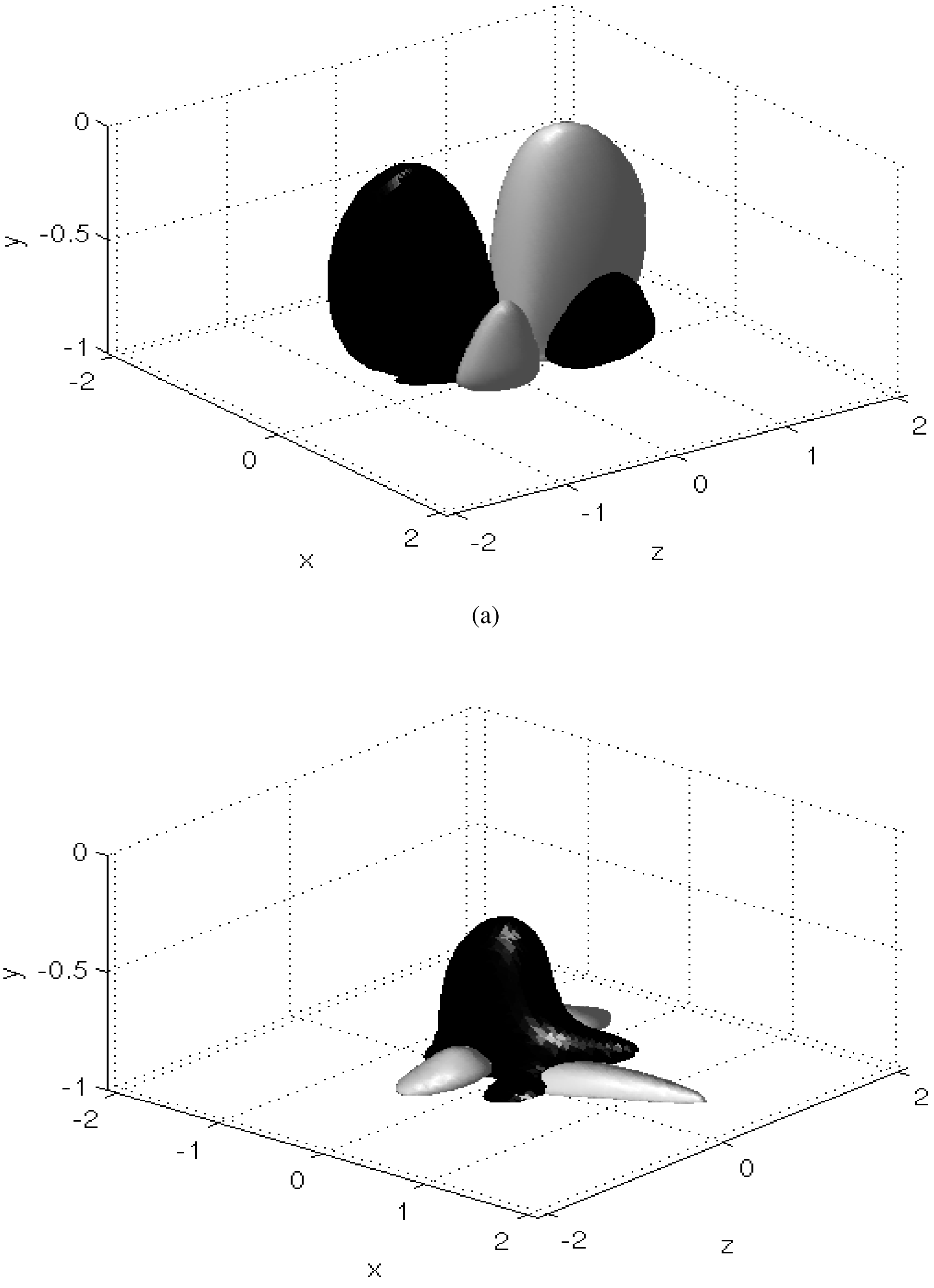

(a)

(b)

Figure 2.3: (a) Estimation kernel for the wall-normal velocity v; negative (black) and positive (light gray) isosurfaces at $\pm 20\%$ of the maximum. (b) Estimation kernel for the wall-normal vorticity η: negative (black) and positive (light gray) isosurfaces at $\pm 5\%$ of the maximum. These kernels relate the wall measurements to the feedback forcing term in the Kalman filter equations, acting on both the equation for the wall-normal velocity and wall-normal vorticity estimates.

and Kim & coworkers [65]. Lim [76] reported a maximum drag reduction of $\approx 20\%$ in a $Re_\tau = 100$[1] turbulent channel flow; Lee et al. [72] obtained a reduction up to $\approx 10\%$ using a LQG-Loop Transfer Recovery formulation. In both approaches, the choice of the cost functional to be minimized was crucial; they used a weighting matrix Q in (2.13) derived from the output equation. In the present work, the choice of the cost function is also addressed, with the purpose of testing a new objective function derived from the dissipation norm presented in previous sections. Note that those results were obtained by measuring skin friction components at the wall; a notable exception is the work by Lee et al. [72], where a suboptimal optimization procedure was applied to a $Re_\tau = 110$ turbulent channel flow using either one of the available wall measurements, including pressure fluctuation. A further aim of the present work is the investigation in the same direction of the effectiveness of either one available wall measurement in determining effective feedback compensators.

At this point, a few considerations concerning the choice of LTI models and compensators for the problem at hand are in order. Linear control theory, and in particular optimal control theory, are well established and provide a rigorous framework for the design of compensators for linear systems, as well as rather efficient numerical techniques. Therefore, it is natural to use such framework in *transition* control [49; 51; 86; 85]. The use of the same framework in the context of a turbulent flow is much less obvious. However, recent evidence exists [66; 79; 81; 65; 123; 70] that linear mechanisms play a fundamental role in the dynamics of wall turbulence, and may be addressed effectively by means of linear control systems designed on appropriate linear models. As shown in the previous sections, the linear feedback compensator is designed on the basis of a linearized model of the flow system at hand; however, the true flow is nonlinear and there is no guarantee about the performance of the compensator when applied to the real system. On the other hand, the linear framework allows the use of well-established and powerful control design techniques, capable of accounting for (at least approximately) modeling errors such as the ones arising from linearization. As a matter of fact, it is reasonable to consider linear optimal control and estimation theory as a good starting point to test control algorithms designed with a mathematically rigorous technique. This philosophy encouraged all recent attempts [65] and will be embraced here.

A further problem is the definition of an appropriate linear model embodying the largest possible amount of information about the physical system. Linearization approaches such as the one outlined in the present chapter may be substituted by measurement or identification of the average input-to-state response function, as recently proposed [81]. Such response-based models, however, would require a

---

[1] In the present thesis, Re_τ denotes the Reynolds number defined with the friction velocity u_τ and the channel half-width; by definition, $u_\tau = \sqrt{\tau_w/\rho}$, where τ_w is the average streamwise skin friction and ρ is the fluid density. According to the usual conventions in the turbulence literature, variables having the $+$ superscript are made non-dimensional with the friction velocity and the viscosity. The length and time scales associated to these two physical quantities will be referred to as *wall units*.

transformation to the state-space form for Riccati-based techniques to be applied; this transformation would be impractical and ill-conditioned for the present high-dimensional setting. The approach presented in this thesis overcomes such difficulty by employing a frequency domain formulation of the optimal compensator design problem. It will be shown that the frequency-domain approach is computationally very efficient when the input and output dimensions are relatively small if compared to the dimension of the state vector, in particular in the single-input/single-output case. This is a key advantage with respect to previously reported approaches, where the massive solution of Riccati equations transformed the compensator design phase in a supercomputing task.

A final issue, not entirely unrelated to the others, is the methodology to account for modeling errors. The approach presented in this chapter introduces a noise on the state equation, having known statistics that can be measured from DNS; such a measurement can be performed and used, at least in principle, in the design of an appropriate Kalman filter accounting for the full space-time structure of the noise on the state. However, up to present a single attempt [24] was made where state estimators were designed on the basis of an approximate noise statistics, derived from DNS measurements. This approximation was in fact a truncation of the time structure of the noise on the state, considered as white. In turbulent flows, the state noise has a well-defined temporal structure that may yield important informations for the estimator design; the appropriate way to consider the full time-space structure of the state noise at the filter design stage is still an open issue. The solution, obtained within a computationally effective framework based on Wiener filtering theory, will be outlined in the present thesis.

Chapter 3

Optimal estimation: a Wiener filtering approach

The issue of linear state estimation in turbulent channel flows, based on real-time wall measurements of skin friction or pressure, is addressed in this chapter. Few state-space approaches for the solution of the state estimation problem in presence of colored noise are briefly described, and shown not to be suitable for the present, very high-dimensional setting. Wiener filtering theory is then proposed as a viable tool for the effective solution of the problem. The basic theory is outlined, and original results are presented and discussed. Prior to discussing the Wiener filter design technique, a brief note on the Wiener-Hopf equation presents the history, the fundamental idea and solution techniques which are relevant to the present context.

3.1 Linear estimation of wall turbulence

The state estimation problem in wall turbulence is the problem of accurately reconstructing, on the basis of limited wall measurements and in presence of measurement disturbances and state noise, the near-wall flow field. In the present setting, the actual system is nonlinear, hence the selected models for the state noise must be representative of the unmodeled dynamics due to linearization of the governing equations.

The first attempts in linear state estimation of wall-bounded flows on the basis of wall measurements have been performed by Högberg et al. [49] and Lee et al. [74]; these authors proposed the use of state estimators in the form of Kalman filters (see Chap. 2), designed on a linearized model of the system obtained from discretization of the Orr-Sommerfeld-Squire equations. An important feature of their approach was the use of identity matrices - scaled by scalar parameters, and chosen by trial and error - as models of noise covariances. This choice neglects the *spatial* structure of the noise on the state, since it implies that noise acting on a given wall-normal location is uncorrelated to noise acting in different locations; moreover, it neglects the *temporal* structure of the noise on the state, as a consequence of the white noise assumption. An improvement has been recently made by Chevalier et al. [24]; they measured via DNS of a turbulent channel flow the spatial structure of the noise covariance, but assumed whiteness of the noise in time. This approach led to spatially localized estimation kernels, that converged upon grid refinement; such estimators were shown to provide a relatively good estimate of the state in the viscous sublayer only. In the present chapter, we effectively move one step further, by accounting for the full space-time structure of the noise acting on the linear equations. The white noise assumption is relaxed and, therefore, the full statistical information as obtained by a DNS is used in the estimator design procedure.

Taking appropriately into account the time structure of the noise requires, in the Kalman filter setting, the design of noise-shaping filters. This approach is briefly detailed in the following, and leads to numerical formulations having intractably huge dimensions. Lastly, the estimation problem is solved by means of Wiener filtering theory. This solution greatly reduces the computational burden of the filter design procedure, if compared to the standard Kalman filter solution. In fact, it will be shown that, in the Wiener filter design procedure, the frequency dependence of the spectral density of the state noise is automatically accounted for in the coefficients of a certain Wiener-Hopf equation, without the need to resort to noise-shaping filters.

3.2 Accounting for the time structure of the state noise

The white noise assumption plays a central role in the derivation of the Kalman filter equations, allowing for the determination of the variance of the state estimation error by means of the Lyapunov equation (2.18). Although the measurement disturbance may be regarded as spectrally white in practical applications, the same assumption on the state noise may be very crude. In order to design an optimal filter in presence of *colored* zero-mean noise n with known autocorrelation function $R_{nn}(\tau)$, it is necessary to design an appropriate pre-filtering system known as *noise-shaping filter*. The noise-shaping filter for a noise n is a dynamical system that can be written in state-space form as

$$\begin{aligned} \dot{x}_f &= A_f x_f + B_f w \\ n &= C_f x_f \end{aligned} \tag{3.1}$$

where w is a zero-mean stationary white Gaussian noise. Matrices A_f, B_f and C_f are determined in such a way that the autocorrelation of the output of this system provides a sufficiently good approximation to $R_{nn}(\tau)$. Once the shaping filter matrices are known, the state-space equations (3.1) may be incorporated in (1.1) to give the augmented system:

$$\begin{aligned} \begin{pmatrix} \dot{x} \\ \dot{x}_f \end{pmatrix} &= \begin{pmatrix} A & C_f \\ 0 & A_f \end{pmatrix} \begin{pmatrix} x \\ x_f \end{pmatrix} + \begin{pmatrix} B \\ 0 \end{pmatrix} u + \begin{pmatrix} 0 \\ B_f \end{pmatrix} w \\ y &= \begin{pmatrix} C & 0 \end{pmatrix} \begin{pmatrix} x \\ x_f \end{pmatrix} + d \end{aligned} \tag{3.2}$$

To this system, standard Kalman filtering theory can be applied to obtain an optimal state estimator.

Usually, the state space realization (3.1) of the noise-shaping filter is not known in advance, whereas the autocorrelation function $R_{nn}(\tau)$ (or, equivalently, the spectral density function $\phi_{nn}(j\omega)$) is the only available information. This problem can be overcome by performing the so-called *spectral factorization* of the spectral density function $\phi_{nn}(j\omega)$; the reader is referred to [118] for an updated review of available spectral factorization methods. Note, indeed, that the problem of the design of a noise-shaping filter can be restated introducing the filter's impulse response function $f(t)$, such that

$$n(t) = \int_{-\infty}^{+\infty} f(t-\tau)w(\tau)\,d\tau; \tag{3.3}$$

note that the filter is an asymptotically stable system. The autocorrelation on $n(t)$ is defined as

$$R_{nn}(\tau) = E\{n(t+\tau)n^H(t)\} \tag{3.4}$$

and hence, substituting (3.3):

$$R_{nn}(\tau) = \int_{-\infty}^{+\infty}\int_{-\infty}^{+\infty} f(v)R_{ww}(\tau+r-v)f^H(r)\ dv\,dr \tag{3.5}$$

Introducing the bilateral Laplace transform of $R_{nn}(\tau)$:

$$\phi_{nn}(s) = \int_{-\infty}^{+\infty} R_{nn}(\tau)e^{-s\tau}\ d\tau$$

leads to

$$\phi_{nn}(s) = F(s)\phi_{ww}(s)F^H(-s^*)$$

where $F(s)$ is the filter transfer function. In particular, when the noise w is white (i.e. delta-correlated) with unit intensity then $R_{ww}(\tau+r-v) = \delta(r-(v-\tau))$ leading to

$$R_{nn}(\tau) = \int_{-\infty}^{\infty} f(v)f^H(v-\tau)dv \tag{3.6}$$

and hence

$$\phi_{nn}(s) = F(s)F^H(-s^*)$$

Note the symmetry with respect to the imaginary axis of the singularities of $\phi_{nn}(s)$; in the case of a real-valued filter response function $f(t)$, a lower-upper symmetry is present such that the function $\phi_{nn}(s)$ has a special quadrantal symmetry with respect to the origin. Specializing the equation above on the imaginary axis, one obtains:

$$\phi_{nn}(j\omega) = F(j\omega)F^H(j\omega) \tag{3.7}$$

Eq. (3.7) shows that, in order to obtain the dynamical equations of the noise shaping filter, it suffices to solve a factorization problem for $\phi_{nn}(j\omega)$. This problem is trivial for scalar rational spectra $\phi_{nn}(j\omega)$, a case in which it may be performed by inspection. In the non-rational case or in the matrix case, this factorization is substantially harder. The difficulty arises from the fact that the above factorization is clearly non unique, and the solution of the problem can be found by requiring that the filter $F(j\omega)$ is minimum phase.

In the following, two different techniques for the design of noise-shaping filter matrices A_f, B_f and C_f are presented. It will be highlighted that a fundamental issue in such approaches is the need to obtain a state-space realization of certain systems, given the statistical information on the noise. Such kind of realizations are impractical and ill-conditioned for the present problem, where the typical dimension of the state vector is $\approx O(100)$. Furthermore, even if it were possible to perform such procedure, the resulting augmented system (3.2) will have dimensions $\approx O(100) \times O(N_{poles}+1)$, where $N_{poles} \approx 10$ is an estimate of the number of poles per variable required to approximate the noise statistics. This dimension is intractably large for the standard Riccati solvers to be applied; hence, the two techniques outlined below are restricted to relatively low-dimensional problems.

3.2.1 Bauer's method

Rewriting eq. (3.6) in discrete time and introducing a sampling time Δt we have

$$R_{nn}(p\Delta t) = \Delta t \sum_{r=-\infty}^{+\infty} f(r\Delta t) f^H((r-p)\Delta t)$$

or, more compactly:

$$R_{nn_p} = \Delta t \sum_{q=-\infty}^{+\infty} f_{p+q} f_q^H .$$

Now, let us introduce the following hermitian block Toeplitz matrix, built from the terms of the discretized correlation

$$T = \begin{pmatrix} R_{nn_0} & R_{nn_{-1}} & R_{nn_{-2}} & \cdots \\ R_{nn_1} & R_{nn_0} & R_{nn_{-1}} & \cdots \\ R_{nn_2} & R_{nn_1} & R_{nn_0} & \cdots \\ \vdots & \vdots & \vdots & \ddots \end{pmatrix} .$$

Since, by assumption, the noise process is not rank deficient, we can introduce the (unique) block Cholesky decomposition

$$T = LL^H$$

where L is a block Cholesky (lower triangular) factor:

$$L = \begin{pmatrix} L_{00} & 0 & 0\dots & \\ L_{10} & L_{11} & 0 & \dots \\ L_{20} & L_{21} & L_{22} & \dots \\ \vdots & \vdots & \vdots & \ddots \end{pmatrix}.$$

Then, it can be shown (see, e.g., [116]) that

$$\lim_{i\to\infty} L_{ij} = \sqrt{\Delta t} f_{i-j} \qquad \forall j, \tag{3.8}$$

obtaining the discretized impulse response function of the noise-shaping filter.

It should be noted that, since the matrix to be factorized is a hermitian Toeplitz matrix, it is possible to use particularly efficient algorithms that exploit the Toeplitz structure (see, for instance, [43]). Once the discretized impulse response of the noise-shaping filter is known, it is necessary to apply a state-space realization procedure to extract matrices A_f, B_f and C_f to be used into the augmented system (3.2).

3.2.2 Approach based on a Riccati equation

This approach is based on the state-space formulation of the *spectral factorization theorem*, presented e.g. in [141].

Let $G(s) = \overline{C}(sI - \overline{A})^{-1}\overline{B} + \overline{D}$ be the transfer function associated to a stabilizable, detectable state-space realization such that $\phi_{nn}(s) = G(s)G^H(-s^*)$; furthermore, let $\phi_{nn}(j\omega) > 0, \quad \forall\omega$.

The realization of the canonical spectral factor, i.e. the unique minimum-phase LTI system associated to $\phi_{nn}(j\omega)$ has a transfer function given by:

$$F(s) = \overline{C}(sI - \overline{A})^{-1}(\overline{B}\overline{D}^H + Y\overline{C}^H)(\overline{D}\overline{D}^H)^{-1/2} + (\overline{D}\overline{D}^H)^{1/2}. \tag{3.9}$$

This is the transfer function of the noise shaping filter given in (3.1), from which filter matrices are identified by inspection. It can be shown that the matrix Y in (3.9) is the stabilizing solution to the algebraic Riccati equation:

$$\begin{gathered}(\overline{A} - \overline{B}\overline{D}^H(\overline{D}\overline{D}^H)^{-1}\overline{C})Y + Y(\overline{A} - \overline{B}\overline{D}^H(\overline{D}\overline{D}^H)^{-1}\overline{C})^H + \dots \\ \dots - Y\overline{C}^H(\overline{D}\overline{D}^H)^{-1}\overline{C}Y + \overline{B}(I - \overline{D}^H(\overline{D}\overline{D}^H)^{-1}\overline{D})\overline{B}^H = 0\end{gathered}$$

This approach provides a state-space representation of the noise-shaping filter once a *tentative* filter is already known in state-space form. Therefore, it requires a preliminary state-space realization procedure using the statistical information on the noise, and for this reason is not practical for the present problem.

3.3 Interlude: N. Wiener, E. Hopf and the Wiener-Hopf integral equation

3.3.1 Biographical sketches

Norbert Wiener (1894-1964) (see fig. 3.1 (a)) was an American child prodigy whose father, a famous Polish-Jewish language professor, rigidly supervised most of his early education. The young Norbert grew up into his father's intellectually active environment, where he encountered many scientists and philosophers to be influential in his later work. He graduated from Tufts College at the age of 14, and performed his graduate studies at Harvard, Cornell, and Cambridge; at the age of 18, he obtained a Ph.D. from Harvard with a thesis on mathematical logic. After the war, in 1919, he obtained a position at MIT, where he remained until retirement in 1960. In those 41 years of mathematical work at MIT he proved to be one of the most profound and influential mathematicians in his century. His early work concerned the mathematical statement of the Brownian motion, and the definition of the now well-known *Wiener measure*, a concept to be fundamental in later developments of the theory of stochastic processes by Kolmogorov, Levy and himself [58]. He established a new framework for potential theory, worked on the development of the foundations of *distribution theory*, and devised with E. Hopf an important method for the solution of certain integral equations of semi-convolutional type, now widely known as the Wiener-Hopf technique. Furthermore, Wiener provided a fundamental generalization of harmonic analysis to stochastic processes, a key ingredient to its work on feedback filters during World War II. During the war, he worked on the design of automatic anti-aircraft guns; this technological problem eventually led him to a profound analysis of the concept of *feedback*. The recognition that feedback systems naturally exist in biological systems and human interactions brought him to the definition of *cybernetics*, a concept to be revolutionary to many scientific fields such as sociology, biophysics, cognitive sciences and psychology.

Eberhard Hopf (1902-1983) (see fig. 3.1 (b)) was an Austrian mathematician and astronomer. At the age of 24 he received his Ph.D. in Mathematics from the University of Berlin, and since then his academic career was divided between Germany and the Unites States. He has been one of the pioneers of ergodic theory, whose work in this field culminated in 1937 with his book *Ergodentheorie*. He also worked on bifurcation theory, and gave significant contributions to the theory of partial differential equations, integral equations, and differential geometry. A particularly fruitful period in his activity was between 1930 and 1936, where he worked at Harvard, MIT and Cambridge. During those years he developed (in collaboration with N. Wiener) the famous Wiener-Hopf technique. In 1936 he moved to Leipzig University as mathematics professor, and then moved to Munich University in 1944. In 1949 he became a US citizen and moved to Indiana University at Bloomington as Research Professor in mathematics, a position he held until his death.

The Wiener-Hopf problem, and the associated solution technique, has many applications in a variety of scientific fields, such as scattering of electromagnetic waves in domains with discontinuous geometries, fracture mechanics and crack propagation, mathematical finance, radiation problems, feedback control and filtering. The Wiener-Hopf equations encountered in this work arise from problems in optimal linear estimation and control, and are similar to those tackled by N. Wiener when working to the design of feedback filters to be applied to anti-aircraft guns.

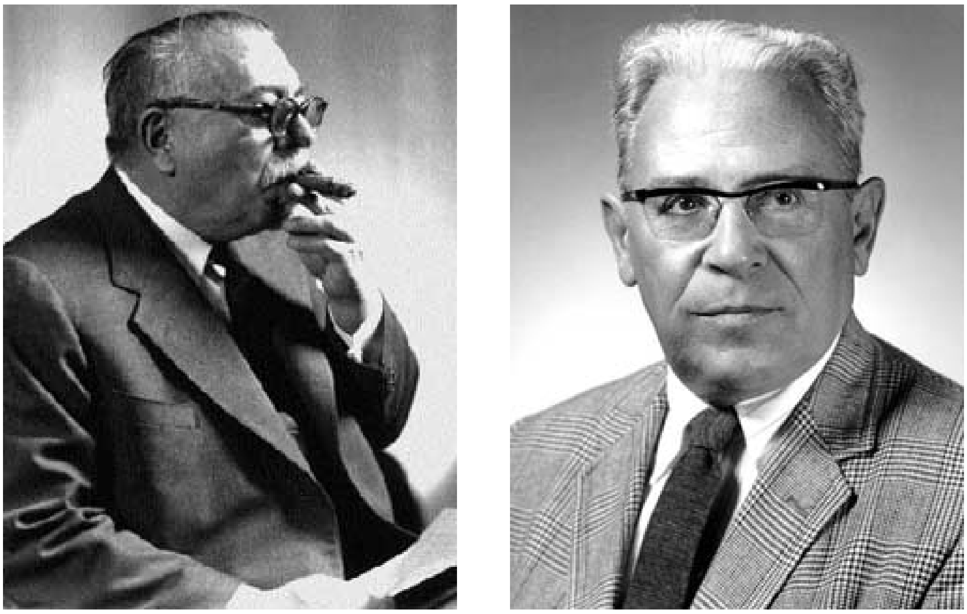

(a) (b)

Figure 3.1: (a): Norbert Wiener. (b): Eberhard Hopf.

3.3.2 Wiener-Hopf equations

The Wiener-Hopf problem and the essentials of analytical and numerical solution techniques are presented in this section. The discussion reported here gives particular emphasis to the form of the equations arising in the compensator design framework, although the technique can be applied to more general situations. Specifically, the approach presented here follows the one reported in [128] or [93, Chap. IV], where a connection between the so-called Hilbert's problem to the Wiener-Hopf problem is described. The interested reader is referred to [128; 34; 93] for a general and rigorous treatment of this subject.

Hilbert problem

Let C be a closed, smooth contour in $\mathbb{C}$. Let $f(\tau)$, $\tau \in C$ be a scalar function satisfying the Lipschitz condition on C. Find the function $\phi_+(s)$, regular inside C and continuous up to C, and the function $\phi_-(s)$, regular outside C, vanishing at infinity and continuous up to C, such that:

$$\phi_+(\tau) - \phi_-(\tau) = f(\tau) \qquad \tau \in C. \tag{3.10}$$

This problem is one of the *Hilbert problems* and its solution is a fundamental building block to the solution of the Wiener-Hopf problems encountered in this work. The definition of an analytic function via a Cauchy integral provides the solution to the Hilbert problem:

$$\phi(s) = \frac{1}{2\pi j} \int_C \frac{f(\tau)}{\tau - s}\, d\tau.$$

In fact, this relation defines two different functions, one analytic outside C and one analytic inside. Letting $s \to \tau$ from both sides of C yields the so-called Plemelji formulae:

$$\begin{aligned} \phi_+(\tau) &= \frac{1}{2} f(\tau) + \frac{1}{2\pi j} \oint_C \frac{f(\xi)}{\xi - \tau}\, d\xi \\ \phi_-(\tau) &= -\frac{1}{2} f(\tau) + \frac{1}{2\pi j} \oint_C \frac{f(\xi)}{\xi - \tau}\, d\xi \end{aligned} \tag{3.11}$$

and by subtraction it is easily seen that (3.10) is satisfied; note that in these relations the integral is taken in Cauchy principal value. By letting the contour C appropriately go to infinity, when $f(\tau)$ goes sufficiently fast to zero at infinity, it is possible to extend the present solution to the case when C is the imaginary axis.

The Wiener-Hopf problem

Given the Lipschitz-continuous scalar functions $A(\tau)$, $B(\tau)$, find the functions $K_+(\tau)$ and $\Lambda_-(\tau)$ such that

$$A(\tau)K_+(\tau) + \Lambda_-(\tau) = B(\tau) \qquad \tau = j2\pi f \tag{3.12}$$

on the imaginary axis. This problem is a generalization of the Hilbert problem on the imaginary axis, in that it considers a general linear combination of *plus* and *minus* functions. Wiener-Hopf problems appearing in the present work belong to a more restricted class, characterized by the following key features:

- $A(\tau) \in \mathbb{R}$
- $\lim_{\tau \to \pm\infty} A(\tau) = \kappa_\pm > 0$

The first feature, along with the Lipschitz continuity of $B(\tau)$, guarantees existence and uniqueness of the solution to the problem [128], as well as the existence of a unique homogeneous solution to the homogeneous problem. The second feature is related to a condition on the non-singularity of the optimal control and estimation problems, meaning that the weight on the control effort is always positive definite, and the measurement noise is always present; this condition is always satisfied in the present work.

The Wiener-Hopf problem (3.12) may be solved in two steps. In a first step, the multiplicative factor $A(\tau)$ is factorized as

$$A(\tau) = \frac{A_+(\tau)}{A_-(\tau)}.$$

When $A(\tau)$ is a scalar, rational function, the factorization can be usually performed by inspection. In the general case, factorization can be performed by taking the natural logarithm of $A(\tau)$

$$\log A_+(\tau) - \log A_-(\tau) = \log A(\tau),$$

thus obtaining an Hilbert problem for $\log A$. Once the factors are known, the problem (3.12) can be recast as

$$A_+(\tau)K_+(\tau) + A_-(\tau)\Lambda_-(\tau) = B(\tau)A_-(\tau),$$

thus obtaining a second Hilbert problem, which may be solved by using the Plemelji formulae.

Analytical example

Let us consider the following Wiener-Hopf problem on the imaginary axis:

$$\frac{(\omega^2+2)^2}{(\omega^2+1)^2}\overline{K}_+ + \Lambda_- = -\frac{1}{-j\omega+1}\frac{1}{\omega^2+1} \tag{3.13}$$

where $\omega = 2\pi f$ has been introduced to simplify the notation. The above equation is in the form

$$A(j\omega)\overline{K}_+(j\omega) + \Lambda_-(j\omega) = B(j\omega).$$

The factorization of the coefficient $A(j\omega)$ is straightforward and can be performed by inspection:

$$A_+(j\omega) = \frac{(j\omega+\sqrt{2})^2}{(j\omega+1)^2}, \qquad A_-(j\omega) = \frac{(-j\omega+1)^2}{(-j\omega+\sqrt{2})^2}.$$

Multiplication of both sides of (3.13) by $A_-(j\omega)$ yields the Hilbert problem:

$$\underbrace{A_+(j\omega)\overline{K}_+(j\omega)}_{\phi_+(j\omega)} + \underbrace{A_-(j\omega)\Lambda_-(j\omega)}_{-\phi_-(j\omega)} = \underbrace{B(j\omega)A_-(j\omega)}_{g(j\omega)}$$

Applying the Plemelj formula one obtains:

$$\phi_+(j\omega) = \frac{1}{2}g(j\omega) + \frac{1}{2\pi j}\oint_C \frac{g(\xi)}{\xi - j\omega}\, d\xi.$$

The integral is taken in Cauchy principal value, and the contour C corresponds to the imaginary axis. Integration can be performed with the aid of the residue theorem, by noting that (see fig. 3.2):

$$\frac{1}{2\pi j}\oint_C \frac{g(\xi)}{\xi - j\omega}\, d\xi = \frac{1}{2\pi j}\int_\Gamma \frac{g(\xi)}{\xi - j\omega}\, d\xi - \frac{1}{2\pi j}\int_\gamma \frac{g(\xi)}{\xi - j\omega}\, d\xi$$

as γ shrinks to zero, and observing that the contribution of the integration on $\ni$ vanishes as the radius of the circumference goes to infinity. The solution to the problem then reads:

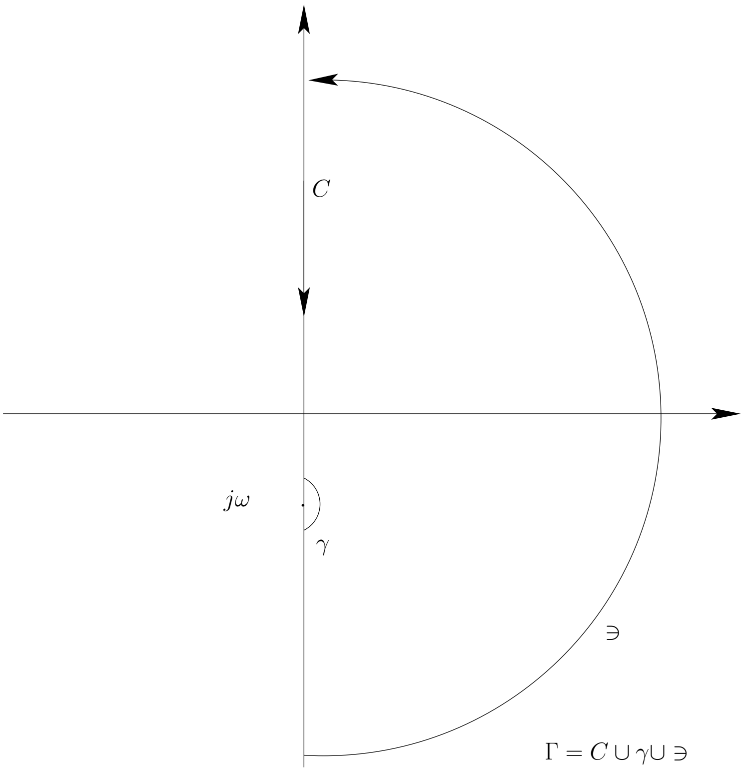

Figure 3.2: Contour integration path used in the example (3.13).

$$\overline{K}_+(j\omega) = \frac{\phi_+(j\omega)}{A_+(j\omega)} = -\frac{(j\omega + 1)}{(\sqrt{2}+1)^2(j\omega + \sqrt{2})^2} \tag{3.14}$$

Numerical solution to the Wiener-Hopf equation

The scalar Wiener-Hopf problem (3.12) may be solved numerically either in frequency domain or in time domain.

The frequency domain approach follows closely the analytical procedure, in that the Wiener-Hopf problem is reduced to a sequence of two Hilbert problems. In turn, each Hilbert problem is solved numerically by employing discrete Fourier transforms. Specifically, it can be noted that the sum of a *plus* and a *minus* function as

$$A(j\omega) = A_+(j\omega) + A_-(j\omega)$$

can be inverse Fourier transformed to give

$$a(t) = a_+(t) + a_-(t)$$

where $a_+(t)$ is a causal function (identically zero for $t < 0$) and $a_-(t)$ is an anticausal function (identically zero for $t > 0$). Therefore, a numerical procedure to solve the Hilbert problem can be performed by inverse Fourier transform of the function $A(j\omega)$, forcing to zero $a(t)$ for $t < 0$ to obtain $a_+(t)$ and then Fourier transforming to obtain $A_+(j\omega)$; the other factor $A_-(j\omega)$ can be readily obtained by subtraction.

The time domain approach is based on a direct discretization of the integral equation corresponding to the original Wiener-Hopf problem. Upon inverse Fourier transform of (3.12), the following integral equations are obtained:

$$\begin{aligned} \int_0^{+\infty} a(t-\tau)k_+(\tau)\,d\tau &= b(t) \qquad t \geq 0 \\ \int_0^{+\infty} a(t-\tau)k_+(\tau)\,d\tau + \lambda_-(t) &= b(t) \qquad t < 0. \end{aligned} \tag{3.15}$$

The full solution can be obtained with two steps, namely, recovering $k_+(t)$ from the first equation and, upon substitution, $\lambda_-(t)$ from the second equation. Discretizing the first equation one obtains:

$$\Delta t \sum_{p=0}^{N} a_{i-p} k_p = b_i \qquad i = 0, \ldots, N$$

which may be rewritten in matrix form as

$$\Delta t \begin{pmatrix} a_0 & a_{-1} & a_{-2} & \cdots \\ a_1 & a_0 & a_{-1} & \cdots \\ a_2 & a_1 & a_0 & \cdots \\ \vdots & \vdots & \vdots & \ddots \end{pmatrix} \begin{pmatrix} k_0 \\ k_1 \\ k_2 \\ \vdots \end{pmatrix} = \begin{pmatrix} b_0 \\ b_1 \\ b_2 \\ \vdots \end{pmatrix}.$$

Therefore, discretization of the linear integral problem (3.15) leads to a linear system of equations; in turn, solution of this system requires the factorization of a positive definite Toeplitz matrix. It is noteworthy that the time-domain solution may be extended to Wiener-Hopf problems with matrix coefficients; in this case, a block-Toeplitz system results from the discretization of the corresponding integral equation.

3.4 The Wiener filter

Consider the linear time-invariant system (1.1):

$$\begin{aligned} \dot{x} &= Ax + Bu + n \\ y &= Cx + d \end{aligned}$$

where the state noise n and the measurement disturbance d are uncorrelated, and have known spectral density functions $\phi_{nn}(f)$ and $\phi_{dd}(f)$, respectively. Introducing the frequency response function $H(f)$ of the system – defined in Chap. 1, eq. (1.4) – the filtering problem may be represented with the schematic block diagram in fig. 3.3. The goal is the design of a linear time-invariant optimal filter, having frequency response $W(f)$, such that the trace of the variance σ_{ee}^2 of the estimation error $e = \tilde{x} - x$ is minimized. From the Wiener-Khintchine relations one obtains

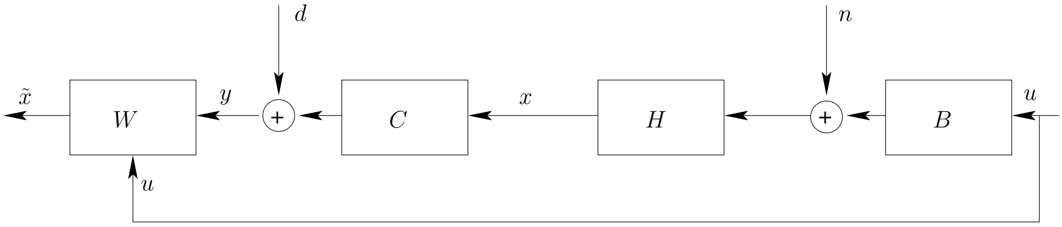

Figure 3.3: Block diagram of the Wiener filtering problem.

$$Tr[\sigma_{ee}^2] = \int_{-\infty}^{+\infty} Tr[\phi_{ee}(f)]\, df.$$

where $\phi_{ee}(f)$ is the spectral density of the estimation error. It is noteworthy that the filter $W(f)$ has two inputs, namely, u and y. Hence, it can be represented in matrix form as

$$W(f) = \begin{pmatrix} W_u(f) & W_y(f) \end{pmatrix}$$

Block diagram relations from fig. 3.3 show that:

$$\begin{aligned} x &= Hn + HBu \\ \tilde{x} &= W_u u + W_y y = W_u u + W_y(d + CHn + CHBu) \\ e &= W_y d + (W_y C - I)Hn + (W_u + W_y CHB - HB)u \end{aligned} \tag{3.16}$$

The state estimation error should not depend on the input u, hence

$$W_u + W_y CHB - HB = 0,$$

and W_u is then obtained as a function of W_y as

$$W_u = (I - W_y C)HB. \tag{3.17}$$

The state estimation error can now be written as the output of a system driven by n and d as

$$e = \begin{pmatrix} W_y & (W_y C - I)H \end{pmatrix} \begin{pmatrix} d \\ n \end{pmatrix}.$$

The relation above applies for deterministic signals, having well-defined Fourier transforms. When d and n are stochastic signals, it is possible to apply relation (1.7) to obtain the spectral density of the error:

$$\begin{aligned} \phi_{ee}(f) = & W_y \phi_{dd} W_y^H + W_y CH\phi_{nn} H^H C^H W_y^H + H\phi_{nn} H^H + \dots \\ & \dots - H\phi_{nn} H^H C^H W_y^H - W_y CH\phi_{nn} H^H. \end{aligned}$$

Hence, the functional to be minimized in the filter design problem is:

$$\begin{aligned} J = \int_{-\infty}^{+\infty} & Tr[W_y \phi_{dd} W_y^H + W_y CH\phi_{nn} H^H C^H W_y^H + H\phi_{nn} H^H + \dots \\ & \dots - H\phi_{nn} H^H C^H W_y^H - W_y CH\phi_{nn} H^H]\, df. \end{aligned}$$

Minimizing this functional leads to an optimal filter which is *noncausal*; this is the best possible LTI filter for the present problem, and its causality notwithstanding may be effectively used in post-processing of statistical data. However, in the present control setting, the filter must be applied runtime, hence causality must be enforced. In terms of frequency domain representation, the causality requirement is expressed by imposing that the filter frequency response is a *plus* function; this can be performed by introducing, under the integral operator, an appropriate Lagrange multiplier function $\Lambda_-(f)$ and modifying the integral (by means of Parseval theorem) as

$$\begin{aligned} J = \int_{-\infty}^{+\infty} & Tr[W_{y,+} \phi_{dd} W_{y,+}^H + W_{y,+} CH\phi_{nn} H^H C^H W_{y,+}^H + H\phi_{nn} H^H + \dots \\ & \dots - H\phi_{nn} H^H C^H W_{y,+}^H - W_{y,+} CH\phi_{nn} H^H] + Tr[\Lambda_- W_{y,+}^H]\, df. \end{aligned} \tag{3.18}$$

Setting to zero the gradient of J with respect to $W_{y,+}^H$ yields:

$$W_{y,+}(CH\phi_{nn}H^HC^H + \phi_{dd}) + \Lambda_- = H\phi_{nn}H^HC^H \tag{3.19}$$

which is a matrix Wiener-Hopf equation; note that the filter frequency response has dimensions $n \times p$. It is noteworthy that the multiplicative coefficient of the filter has dimensions $p \times p$, where p is the dimension of the output vector. If $p = 1$, the vector equation (3.19) is in fact a set of independent scalar equations. Factorization of the multiplicative term may be performed once at the beginning of the numerical solution to the Wiener-Hopf problem, and then additive factorization can be performed for each component of the vector equation. If the state vector has dimension n, the solution of the filtering problem is reduced to the solution of $n + 1$ independent scalar Hilbert problems; this is computationally more effective than the solution of the $n \times n$ algebraic Riccati equation required in the Kalman filtering procedure. Note also that the spectral density of state noise and measurement disturbance appear in functional form in the coefficients of the Wiener-Hopf equation (3.19), so that accounting for colored noise in the design procedure becomes straightforward, provided that $\phi_{dd}(f) > 0$, $\forall f$.

3.5 Model of the system

The design procedure of the Wiener filter requires a model of the system at hand in the form of frequency response function. Such frequency response $H(f)$, obtained from the discretization of the Orr-Sommerfeld-Squire equations, is computed directly from the state-space form of the discretized equations. However, prior to compute the frequency response as Fourier transform of the impulse response function, as defined in Chap. 1, the system of equations is diagonalized and, as suggested in [110] or by Lim [76], the modes corresponding to poorly resolved and highly damped eigenvalues of the discrete Orr-Sommerfeld-Squire spectrum have been discarded. In addition to reducing the size of the problem by truncating spurious dynamics, working in modal variables is beneficial because the frequency response of a diagonal system can be computed analytically, thus easing the design procedure. In the present work, it has been chosen to remove half of the modes, as suggested in [127], for each wavenumber pair; the truncated model was thoroughly tested verifying that it reproduces properly the transient energy growth [110; 121] for all the wavenumber pairs considered.

3.6 State noise measurements by DNS

The Wiener filter design procedure requires, furthermore, the knowledge of the state noise autocorrelation function, defined - for each wavenumber pair - as in

Chap. 2:

$$R_{\hat{r}\hat{r}}(y_1, y_2, \tau; \alpha, \beta) = E\{\hat{h}(y_1, t + \tau; \alpha, \beta)\hat{h}^H(y_2, t; \alpha, \beta)\}.$$

Note that this is a function of the two locations in the (non-homogeneous) wall-normal direction, and the time separation; therefore, this quantity is a function of 5 independent variables. In the following, the dependence on the wavenumber pair will be understood. The procedure to compute this function is conceptually straightforward. Nonlinear terms $\hat{h}$ are computed runtime while performing a DNS of a turbulent channel flow, and stored to disk every Δt; integration is performed on a sufficiently long time window having length T for second-order statistics to be converged. The database thus obtained is then post-processed wavenumber-wise, in order to compute the function $R_{\hat{r}\hat{r}}(y_1, y_2, \tau)$. In turn, this information is used in the Wiener filter design procedure, for each wavenumber pair; in fact, the correlation of the state noise in (2.7) is readily recovered from

$$R_{nn}(y_1, y_2, \tau) = M^{-1} R_{\hat{r}\hat{r}}(y_1, y_2, \tau) M^{-H}$$

and then the spectral density $\phi_{nn}(y_1, y_2, f)$ follows immediately from Fourier transform of $R_{nn}(y_1, y_2, \tau)$.

The procedure outlined above has been performed for a turbulent channel flow at $Re_\tau = 100$, based on the friction velocity and the channel half-width. Parameters of the simulation and the database collection procedure are reported in table 3.1. The very long averaging time $T^+ = 10000$ has been chosen ten and two times larger than the ones used in [57] and [102], respectively, in order to provide well converged second-order statistics. Although DNS of turbulent channel flows are customary at Reynolds number as low as $Re_\tau = 100$ on modern supercomputers, the present simulation proved to be particularly challenging from the point of view of data storage and handling; in fact, even using the minimum set of variables $(\hat{v}, \hat{\eta})$, it was necessary to limit the wavenumber range of stored data to $|\alpha| \leq \overline{\alpha}$ and $|\beta| \leq \overline{\beta}$ to keep the dimensions of the database to the relatively small size of $\approx 200\, GB$. Furthermore, the post-processing procedure to compute $R_{\hat{r}\hat{r}}(y_1, y_2, \tau)$ requires careful data handling, since the typical size of this discretized function is $\approx 300\, MB$ for each wavenumber pair.

Numerical simulations are performed using the computer code and computing system developed by Luchini and Quadrio and described in [80]. The code is a parallel solver of the Navier-Stokes equations for the incompressible flow in a plane channel. Time advancement employs the usual semi-implicit approach, where nonlinear terms are advanced explicitly with a low-storage Runge-Kutta scheme, and viscous terms are advanced implicitly. The mixed spatial discretization employs Fourier expansions in wall-parallel directions, and fourth-order accurate compact finite difference schemes discretize the wall-normal direction. The locality of finite difference operators in physical space allows to exploit a simple partitioning of the data among different computing machines, with excellent parallel performance. The

Re_τ	L_x	L_z	N_x	N_z	N_y	Δt^+_{sim}	Δt^+	T^+	$\overline{\alpha}$	$\overline{\beta}$
100	4π	2π	64	64	64	0.125	0.5	10000	10	20

Table 3.1: Parameters used in the construction of the database for the state noise correlations; Δt_{sim} is the time step size used in the simulations, and N_y is the number of discretization points in wall-normal direction.

amount of communication is reduced by a carefully designed parallel algorithm, so that the code can run on a computing system assembled without expensive networking hardware. This parallel algorithm proved to be well-suited for the database construction procedure; in fact, it was possible to store data pertaining to certain wall-normal regions in each machine's local hard disk, without the need to overload the network during the simulation with data to be stored in a single database. The construction of the full database required ≈ 15 days on a cluster of 10 dual-core Intel Xeon machines.

Note that the correlation function $R_{\hat{r}\hat{r}}(y_1, y_2, \tau)$ may be expanded as

$$R_{\hat{r}\hat{r}}(y_1, y_2, \tau) = \begin{pmatrix} E\{\hat{h}_v(y_1, t+\tau)\hat{h}_v^H(y_2, t)\} & E\{\hat{h}_v(y_1, t+\tau)\hat{h}_\eta^H(y_2, t)\} \\ E\{\hat{h}_\eta(y_1, t+\tau)\hat{h}_v^H(y_2, t)\} & E\{\hat{h}_\eta(y_1, t+\tau)\hat{h}_\eta^H(y_2, t)\} \end{pmatrix}; \tag{3.20}$$

therefore, for each wavenumber pair and each couple of positions in y direction, each entry of this matrix corresponds to the auto- or cross-correlation of the nonlinear terms acting on the $\hat{v}$ or $\hat{\eta}$ equations in (2.5). Note also that, by definition, the following symmetry property holds:

$$R_{\hat{r}\hat{r}}(y_1, y_2, \tau) = R_{\hat{r}\hat{r}}^H(y_2, y_1, -\tau).$$

The fact that the spatial structure of the noise on the state in (2.5) is nontrivial has been discussed in recent work [24] and will not be investigated in detail here. In this work, the temporal structure of the state noise is particularly emphasized, and is briefly discussed below by considering the correlation function pertaining to the wavenumber pair ($\alpha = 1$, $\beta = 2$) - representative of all the wavenumbers considered - and at a fixed reference wall-normal position $y^+_{1,ref} = 10$.

Fig. 3.4 shows the diagonal components of the autocorrelation matrix function $E\{\hat{h}_v(y_{1,ref}, t+\tau)\hat{h}_v^H(y_2, t)\}$ and $E\{\hat{h}_\eta(y_{1,ref}, t+\tau)\hat{h}_\eta^H(y_2, t)\}$. The maximum autocorrelation is located, as expected, at $y_2^+ = y^+_{1,ref}$, $\tau^+ = 0$. Considering, for instance, a correlation reference value of 50% of the maximum, it is shown that, at this wavenumber, the nonlinear terms $\hat{h}_v$ are self-correlated on a typical length scale of 10 wall units - at the given reference wall normal position $y_{1,ref}$ - and on a typical time scale of 10 viscous time units. Nonlinear terms $\hat{h}_\eta$ appear to be self-correlated on a typical length scale of about 12 wall units, and on a typical time scale of about 27 viscous time units. Representation of these functions in the τ, y_2 plane at a given location $y_{1,ref}$ do not exploit the symmetry of the correlation; this property is exemplified in fig. 3.6 (a), corresponding to a cut of fig. 3.4 at $y_2^+ = y^+_{1,ref} = 10$.

It is shown indeed that the computed result is symmetric with respect to the axis $\tau = 0$, where the maximum correlation also occurs.

Fig. 3.5 shows the off-diagonal correlation matrix components $E\{\hat{h}_v(y_{1,ref}, t + \tau)\hat{h}_\eta^H(y_2, t)\}$ and $E\{\hat{h}_\eta(y_{1,ref}, t + \tau)\hat{h}_v^H(y_2, t)\}$. Off-diagonal components need not have the maximum correlation at $y_2^+ = y_{1,ref}^+$, $\tau^+ = 0$. Considering again a correlation reference value of 50% of the maximum, it is shown that the nonlinear terms are cross-correlated on a typical length scale of about 10 viscous lengths, and on a typical time scale of 25 to 35 viscous time units. Fig. 3.6 (b), corresponding to a cut of fig. 3.5 at $y_2^+ = y_{1,ref}^+ = 10$, highlights the antisymmetry of the off-diagonal components with respect to the axis $\tau = 0$, and shows that the maximum correlation occurs at this wall-normal position at a given non-zero τ^+.

These results show that, additionally to the correlation in space, the correlation of the state noise acting on the linearized equations (2.5) has a nontrivial temporal structure, and confirm the unphysical nature of the white noise assumption. The question of how crude is this assumption in terms of preventing a linear estimator to be effective in turbulent wall flows is addressed in the next section.

3.7 Wiener filter: performance evaluation

The Wiener filter has been designed for an array of wavenumber pairs $|\alpha| \leq \overline{\alpha}$ and $|\beta| \leq \overline{\beta}$. Measurement noise is assumed to be white, and tests have been performed for two values of the noise intensity, namely, $\phi_{dd} = 10^{-3}$ and $\phi_{dd} = 10^{-5}$. It is assumed that measurement of either one of the two wall skin friction components or pressure fluctuation is available; in this way, as noted in this chapter, the Wiener-Hopf problem arising in the design of the optimal filter has a scalar multiplicative coefficient, and its numerical solution is particularly efficient. Similar Wiener filters, designed with the same parameters but using a state noise with artificially truncated time structure (in order to actually design a Kalman filter similar to those designed in [24]), are used for comparison purposes, and will be denoted hereinafter as “Kalman filters”.

Filtering simulations are performed using a modified turbulent channel flow solver, where equations of the filter are integrated together with the nonlinear flow equations. Instead of resorting to a state-space realization of the filter, we choose to directly compute the estimated state by using the discretized form of the following convolutional relation:

$$\hat{\hat{x}}(\alpha, \beta, t) = \int_0^t \hat{W}(\alpha, \beta, \tau)\hat{m}(\alpha, \beta, t - \tau)\, d\tau,$$

where $\hat{m}(\alpha, \beta, t)$ represents the history of wall measurements and $\hat{W}(\alpha, \beta, t)$ is the filter’s impulse response.

Results are first presented for two representative wavenumber pairs, namely $(\alpha, \beta) = (1, 3)$ and $(\alpha, \beta) = (3, 1)$. A first measure of the estimation capability

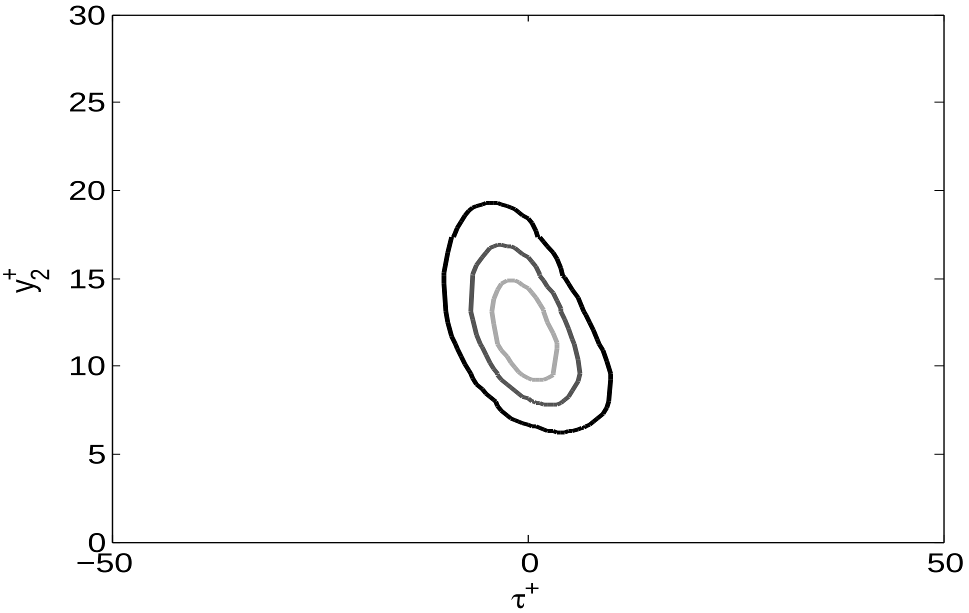

(a)

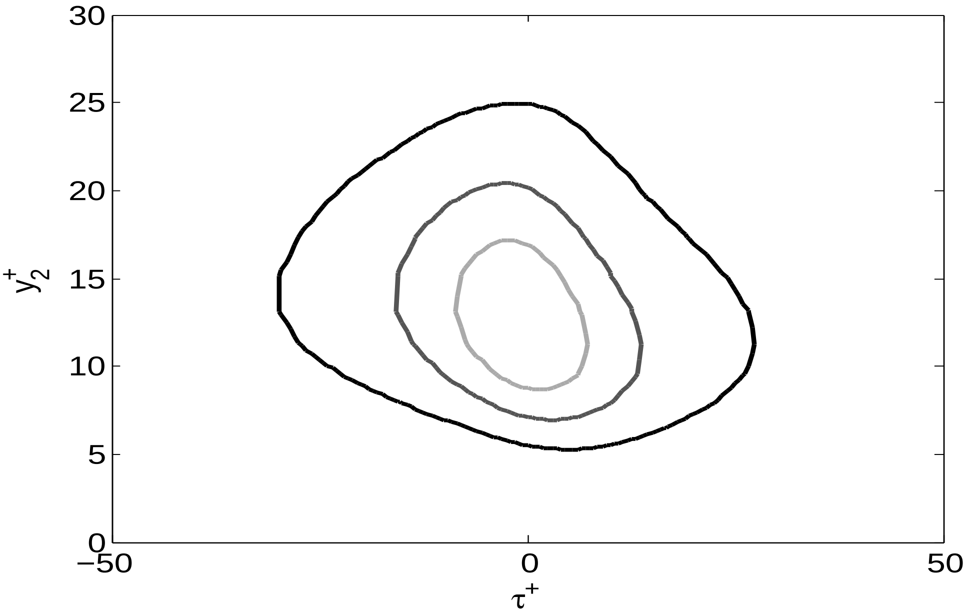

(b)

Figure 3.4: Lines at constant absolute value of (a) $E\{\hat{h}_v(y_{1,ref}, t+\tau)\hat{h}_v^H(y_2, t)\}$ and (b) $E\{\hat{h}_\eta(y_{1,ref}, t+\tau)\hat{h}_\eta^H(y_2, t)\}$, where $y_{1,ref}^+ = 10$. Level is taken at 25%, 50% and 75% of the maximum (dark to light gray). Dependent variables y_2 and τ normalized with viscous units. Results at $\alpha = 1, \beta = 2$, $Re_\tau = 100$.

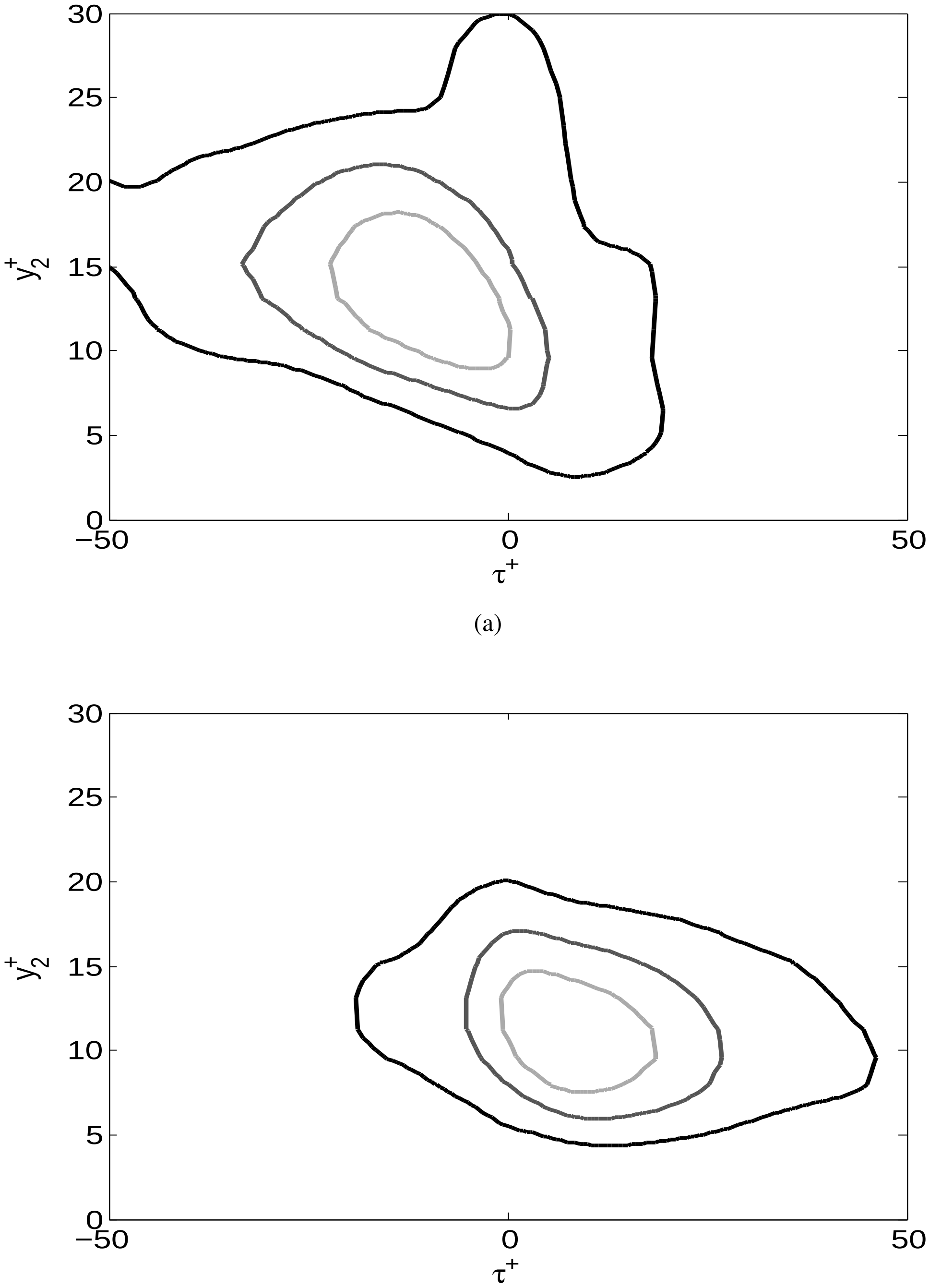

(a)

(b)

Figure 3.5: Lines at constant absolute value of (a) $E\{\hat{h}_v(y_{1,ref},t+\tau)\hat{h}_\eta^H(y_2,t)\}$ and (b) $E\{\hat{h}_\eta(y_{1,ref}t+\tau)\hat{h}_v^H(y_2,t)\}$, where $y_{1,ref}^+ = 10$. Level is taken at 25%, 50% and 75% of the maximum (dark to light gray). Dependent variables y_2 and τ normalized with viscous units. Results at $\alpha = 1, \beta = 2$, $Re_\tau = 100$.

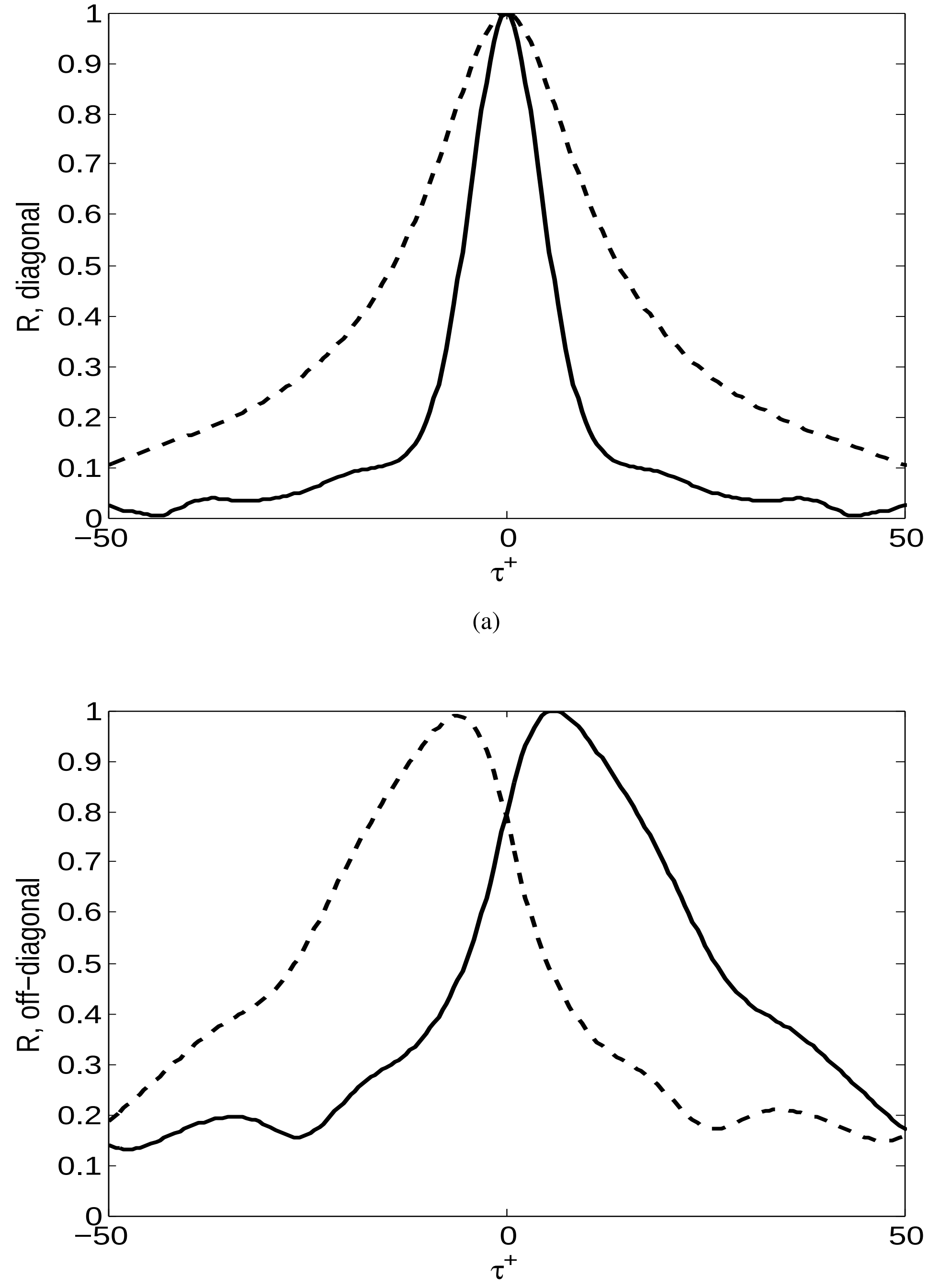

(a)

(b)

Figure 3.6: (a) Plot of $|E\{\hat{h}_v(y_{1,ref}, t+\tau)\hat{h}_v^H(y_{1,ref}, t)\}|$ (solid) and $|E\{\hat{h}_\eta(y_{1,ref}, t+\tau)\hat{h}_\eta^H(y_{1,ref}, t)\}|$ (dashed) against the time separation τ. (b) Plot of $|E\{\hat{h}_\eta(y_{1,ref}, t+\tau)\hat{h}_v^H(y_{1,ref}, t)\}|$ (solid) and $|E\{\hat{h}_v(y_{1,ref}, t+\tau)\hat{h}_\eta^H(y_{1,ref}, t)\}|$ (dashed) against the time separation τ. These results are consistent with the symmetry properties on the autocorrelation $R_{\hat{r}\hat{r}}(y_1, y_2, \tau)$. Dependent variable τ normalized with viscous units. Results at $\alpha = 1, \beta = 2, y_{1,ref}^+ = 10$, $Re_\tau = 100$.

Real/Imaginary part	Wiener			Kalman		
	τ_x	τ_z	p	τ_x	τ_z	p
$Re(\hat{v})$	0.1104	0.5936	0.5007	0.1303	0.5946	0.5013
$Im(\hat{v})$	0.1347	0.5903	0.5111	0.1520	0.5912	0.5107
$Re(\hat{\eta})$	0.7968	0.7716	0.7266	0.7766	0.7594	0.7323
$Im(\hat{\eta})$	0.8005	0.7705	0.7239	0.7804	0.7585	0.7300
$Re(\hat{v})$	0.0877	0.5934	0.4888	0.2138	0.5916	0.5024
$Im(\hat{v})$	0.1087	0.5909	0.4993	0.2362	0.5891	0.5116
$Re(\hat{\eta})$	0.7432	0.7697	0.7413	0.7562	0.7606	0.7317
$Im(\hat{\eta})$	0.7483	0.7677	0.7380	0.7613	0.7596	0.7295

Table 3.2: Correlation coefficients between the actual state and the estimated states, as provided by the Wiener and Kalman filter. First block row corresponds to $\phi_{dd} = 10^{-3}$, second block row to $\phi_{dd} = 10^{-5}$; results for $(\alpha, \beta) = (1, 3)$, $y^+ = 10$.

is the correlation coefficient between the actual state and its estimate provided by either Wiener or Kalman filters. We choose a representative location in wall-normal direction, $y^+ = 10$, and compute the correlation coefficients on an ensemble of data collected in a DNS performed for 2000 viscous time units. Table 3.2 and 3.3 report the computed correlation coefficients; it is shown that the results obtained with the Wiener and Kalman filters are strikingly similar, and there is no substantial improvement in the correlation coefficients when accounting for the time structure of the noise, for these wavenumbers. The measurement disturbance intensity affects these results in a wavenumber-dependent fashion, indicating that wavenumber-wise tuning of the filter with the term ϕ_{dd} might improve results.

However, correlation coefficients do no provide an assessment of the quantitative difference between the actual and estimated state. To this aim, we report in fig. 3.7, 3.8 and 3.9 the time-averaged energy density in wall-normal direction, as a function of the wall-normal variable, for the two wavenumber pairs considered. These results show that both the Wiener and the Kalman estimators provide a relatively good estimate of the spectral energy density only in the very near-wall region $y^+ < 10$ (with the exception in fig. 3.8 (b)). Further inside the channel, the energy of the estimated state is far different from that of the actual state and, typically, the Wiener filter tends to provide smaller values of the energy density if compared to the Kalman filter. The fact that linear estimators do not provide a good estimate of the energy in the flow is not unexpected. In fact, the evolution equation for the spectral energy in the linear case misses the nonlinear triadic interaction term, accounting for energy redistribution among wavenumbers [120]. Therefore, energy in the linear case will be under- or over-estimated, depending on the nonlinear interactions in spectral space of the real flow; the present results indicate that accounting for the time structure of the state noise is not sufficient for recovering this effect.

Nevertheless, it was shown by previous work (see, e.g. [76; 65]) that linear controllers derived from optimal control theory typically require information on the

Real/Imaginary part	Wiener τ_x	Wiener τ_z	Wiener p	Kalman τ_x	Kalman τ_z	Kalman p
$Re(\hat{v})$	0.0622	0.1848	0.4094	0.0537	0.1490	0.4131
$Im(\hat{v})$	0.0613	0.1848	0.4087	0.0529	0.1493	0.4127
$Re(\hat{\eta})$	-0.0686	-0.4141	0.1685	-0.1217	-0.4109	0.2240
$Im(\hat{\eta})$	-0.0690	-0.4139	0.1668	-0.1227	-0.4107	0.2235
$Re(\hat{v})$	0.2013	0.2429	0.3065	0.1471	0.1835	0.4154
$Im(\hat{v})$	0.2003	0.2429	0.3062	0.1463	0.1838	0.4152
$Re(\hat{\eta})$	0.0336	-0.4267	0.0065	-0.1200	-0.4279	0.2244
$Im(\hat{\eta})$	0.0336	-0.4263	0.0059	-0.1209	-0.4275	0.2239

Table 3.3: Correlation coefficients between the actual state and the estimated states, as provided by the Wiener and Kalman filter. First block row corresponds to $\phi_{dd} = 10^{-3}$, second block row to $\phi_{dd} = 10^{-5}$; results for $(\alpha, \beta) = (3, 1)$, $y^+ = 10$.

flow state in the near-wall region only. Therefore, state estimators may need to provide a good estimate of the near-wall flow, while states far away from the wall may be estimated wrongly without affecting substantially the control performance. Stemming from this argument, it is natural to evaluate the estimation performance of the Wiener and Kalman filters by weighting the estimated state using an optimal controller designed for a turbulent flow at the same Re. To this aim, we use control kernels designed for $Re_\tau = 100$ turbulent channel flow, obtained by minimizing a functional derived from a weighted form of the kinetic energy norm; see App. A for details about this optimal controller. This state-feedback controller led to drag reduction up to $\approx 30\%$ when applied to the fully turbulent flow. The control signal computed from the application of such control kernel to the real flow state is compared with those obtained by application of the kernel to the estimated state. Note that no feedback is introduced to the flow; the purpose here is to compare directly a reference control signal to the ones derived from the estimated data. A concise presentation of the results for the two representative wavenumbers considered is reported in table 3.4, where it is shown that the correlation coefficient between the control signal derived from the Wiener filter estimate and the reference signal is comparable to the one obtained with the Kalman filter. The time integral of the energy of the control signal $\int |\hat{u}|^2 dt$ is reported for the reference case, the Wiener filter case and the Kalman filter case in table 3.5. Again, it is shown quantitatively that, at the two wavenumbers tested, the performance of both filters is similar.

Finally, estimation results obtained when using both the Wiener and Kalman filter on the full array of wavenumbers $|\alpha| < \overline{\alpha}$ and $|\beta| < \overline{\beta}$ are reported in fig. 3.10, 3.11 and 3.12 for the streamwise, spanwise skin friction and pressure measurements, respectively; measurement noise intensity is $\phi_{dd} = 10^{-3}$. As a concise indicator of the estimation performance, we use here the energy density in wall normal direction, summed over all wavenumbers $|\alpha| \leq \overline{\alpha}$ and $|\beta| \leq \overline{\beta}$. It is shown that, when measuring either one of the wall skin friction components, both filters

Real/Imaginary part	Wiener			Kalman		
	τ_x	τ_z	p	τ_x	τ_z	p
$Re(\hat{c})$	0.7180	0.7076	0.7208	0.6991	0.6943	0.7178
$Im(\hat{c})$	0.7125	0.7062	0.7210	0.6939	0.6928	0.7166
$Re(\hat{c})$	0.3419	0.4047	0.5756	0.3174	0.3872	0.5660
$Im(\hat{c})$	0.3432	0.4049	0.5658	0.3177	0.3873	0.5645

Table 3.4: Correlation coefficients of the control signals $\hat{c}$ computed from the Wiener and Kalman filters estimates with that computed from the real flow state (reference signal), for the three measurements. Top block row: $\alpha = 1, \beta = 3$; bottom block row: $\alpha = 3, \beta = 1$. Results with $\phi_{dd} = 10^{-3}$.

Reference	Wiener			Kalman		
$\int \lvert\hat{u}\rvert^2 \, dt$	τ_x	τ_z	p	τ_x	τ_z	p
1.5675	2.4043	0.8252	1.3961	2.5796	0.9463	1.8081
0.0723	0.0646	0.0029	0.1340	0.0798	0.0026	0.1846

Table 3.5: Time integral of the energy of the control signal, as computed from the Wiener and Kalman filters estimates and from the real flow state, for the three measurements. Top block row: $\alpha = 1, \beta = 3$; bottom block row: $\alpha = 3, \beta = 1$. Results with $\phi_{dd} = 10^{-3}$.

perform similarly in the near wall region; in these cases, the estimated energy is close to the actual energy in the very near wall region only, up to $y^+ \approx 7$. On the other hand, pressure measurements leads to filters that substantially overestimate the energy density of the flow; this is in agreement with the fact noted by Chevalier et al. [24], that measurement of wall pressure is only useful when estimating the pressure field, but does not provide significant information to estimate the near-wall velocity field.

3.8 Conclusions

In this chapter, the Wiener filtering technique has been proposed as an effective tool for designing optimal filters for estimation of wall turbulence. In particular, the full time-space structure of the state noise, as measured by DNS, can be accounted for through the use of these filters. In the linear setting, they are the *best possible* LTI estimators for the system at hand. Their performance has been evaluated on representative single-wavenumber cases, as well as for a large array of wavenumbers, and compared to that of similar estimators designed to account for the spatial structure of the state noise only. Despite the non trivial temporal structure of the state noise, our performance assessment shows that including it in the filter design does not improve the estimation performance significantly. This suggests that the white-noise assumption, first proposed in [24], is reasonably accurate for state estimation purposes, at least in the present context of low-Reynolds number wall turbulence.

Furthermore, the present results indicate that linear estimation strategies for wall turbulence may be inherently limited, thus suggesting the need to resort to nonlinear observers (for instance, in the form of extended Kalman filters) in order to provide better estimates of the near wall flowfield on the basis of wall measurements.

Nevertheless, the formulation of the state estimation problem presented in this chapter, and the associated Wiener filter design technique, is numerically efficient if compared to the standard Riccati-based approach, especially when a single measurement is available. Therefore, it may represent a viable alternative to the standard approach in similar state estimation problems, where the high dimensionality of the estimation problem can be coped by the present approach.

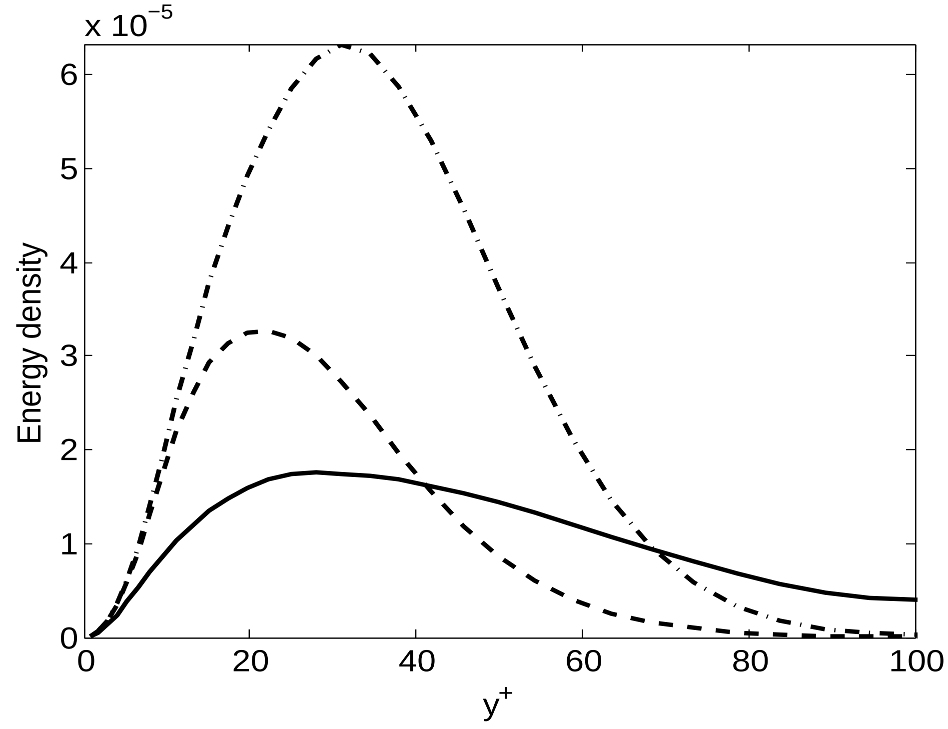

(a)

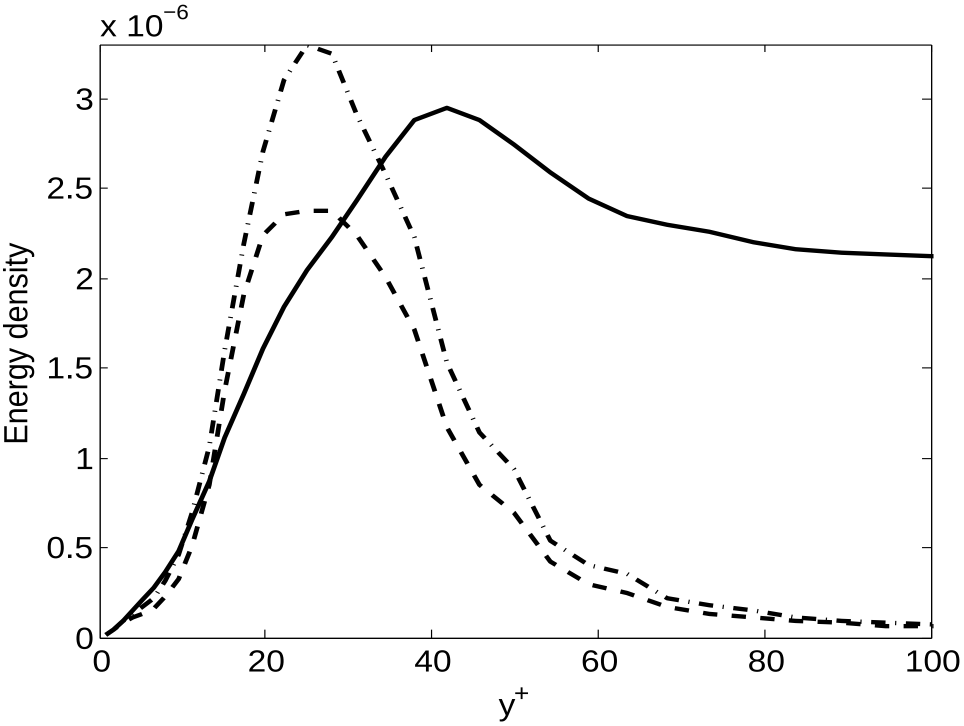

(b)

Figure 3.7: Spectral energy density (solid) and relative estimates via Wiener filter (dashed) and Kalman filter (dash-dotted); (a) $(\alpha, \beta) = (1, 3)$, (b) $(\alpha, \beta) = (3, 1)$. Results obtained for the measurement of streamwise skin friction τ_x.

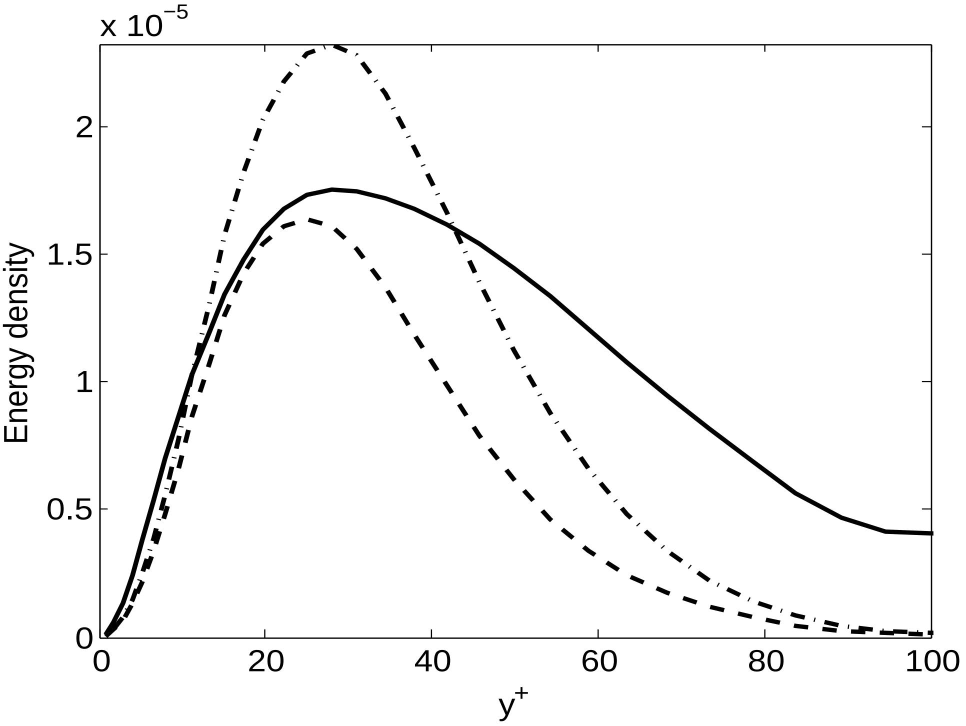

(a)

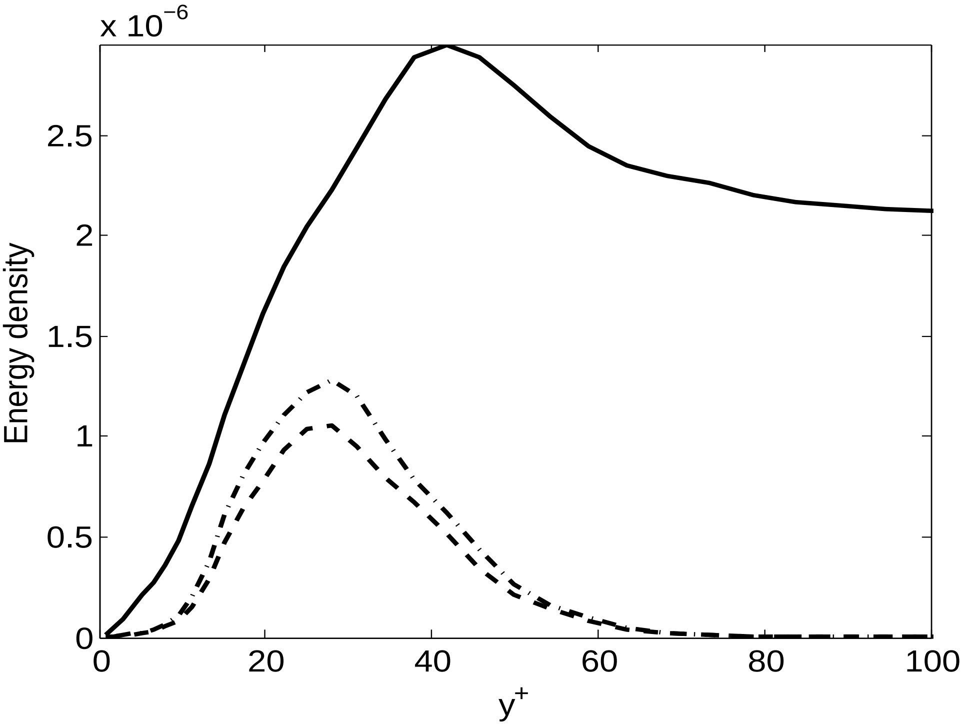

(b)

Figure 3.8: Spectral energy density (solid) and relative estimates via Wiener filter (dashed) and Kalman filter (dash-dotted); (a) $(\alpha, \beta) = (1, 3)$, (b) $(\alpha, \beta) = (3, 1)$. Results obtained for the measurement of spanwise skin friction τ_z.

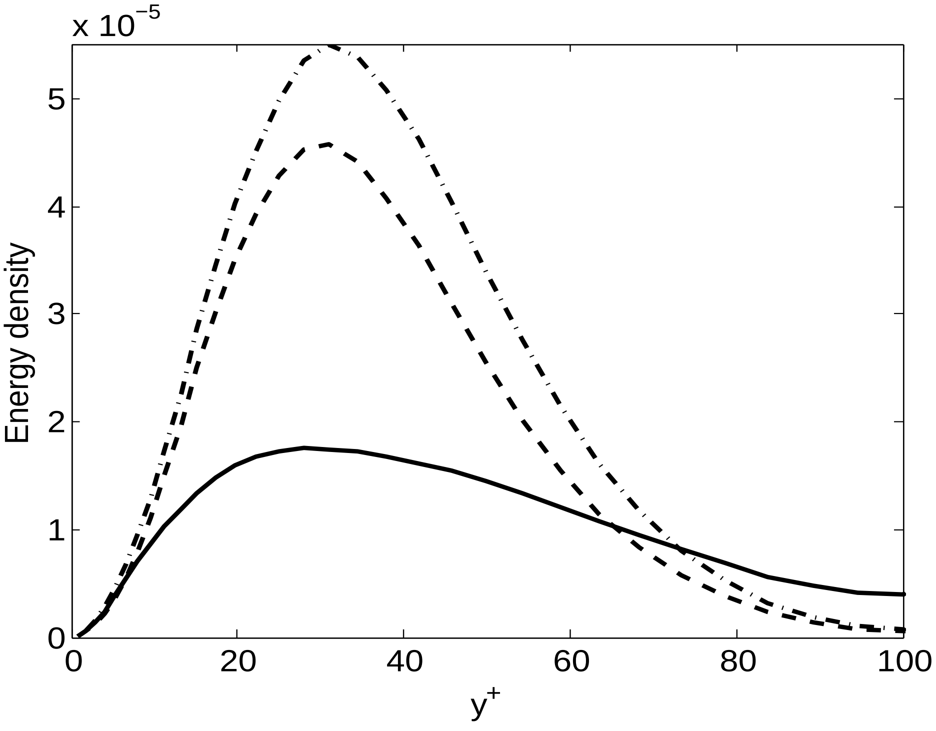

(a)

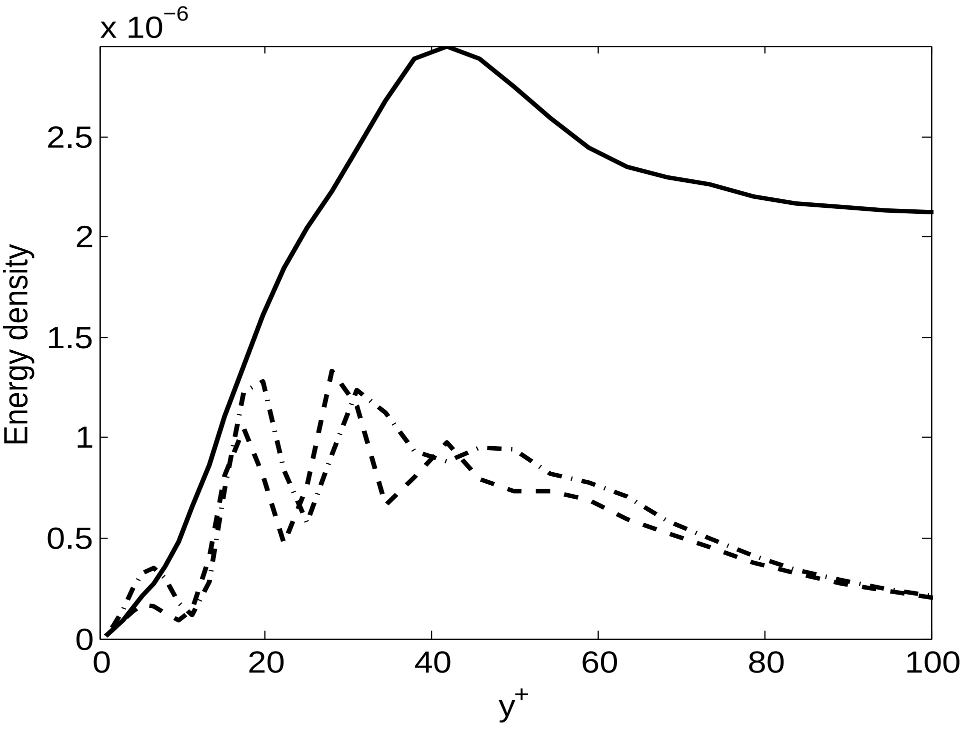

(b)

Figure 3.9: Spectral energy density (solid) and relative estimates via Wiener filter (dashed) and Kalman filter (dash-dotted); (a) $(\alpha, \beta) = (1, 3)$, (b) $(\alpha, \beta) = (3, 1)$. Results obtained for the measurement of pressure fluctuations p.

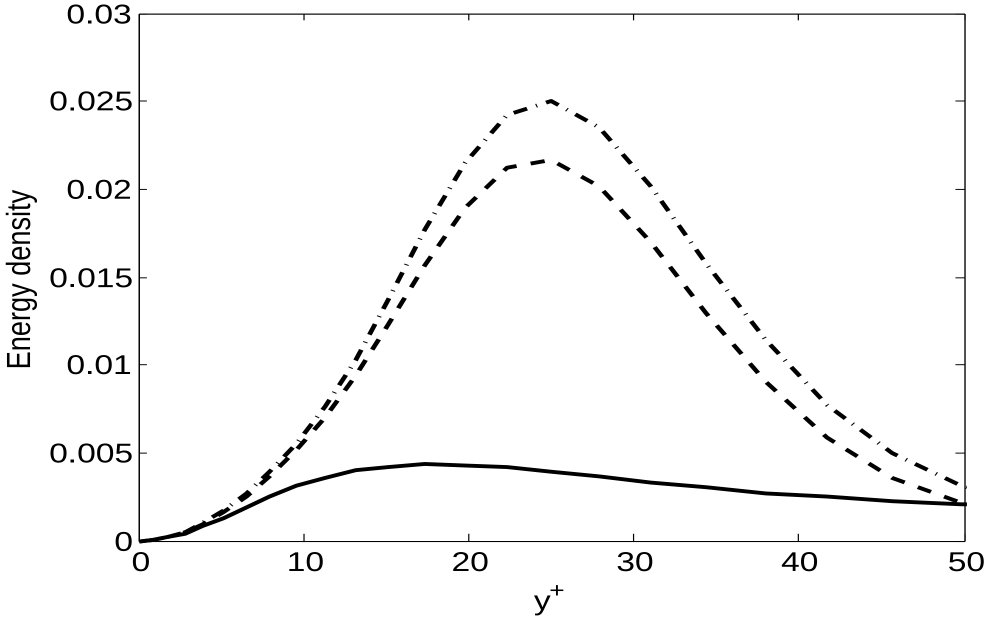

Figure 3.10: State energy density (solid), Wiener filter estimate (dashed) and Kalman filter estimate (dash-dotted) in the region $y^+ < 50$, evaluated for the array of wavenumber pairs $|\alpha| < \overline{\alpha}$ and $|\beta| < \overline{\beta}$. Measurement is streamwise skin friction. Results at $Re_\tau = 100$, $\phi_{dd} = 10^{-3}$.

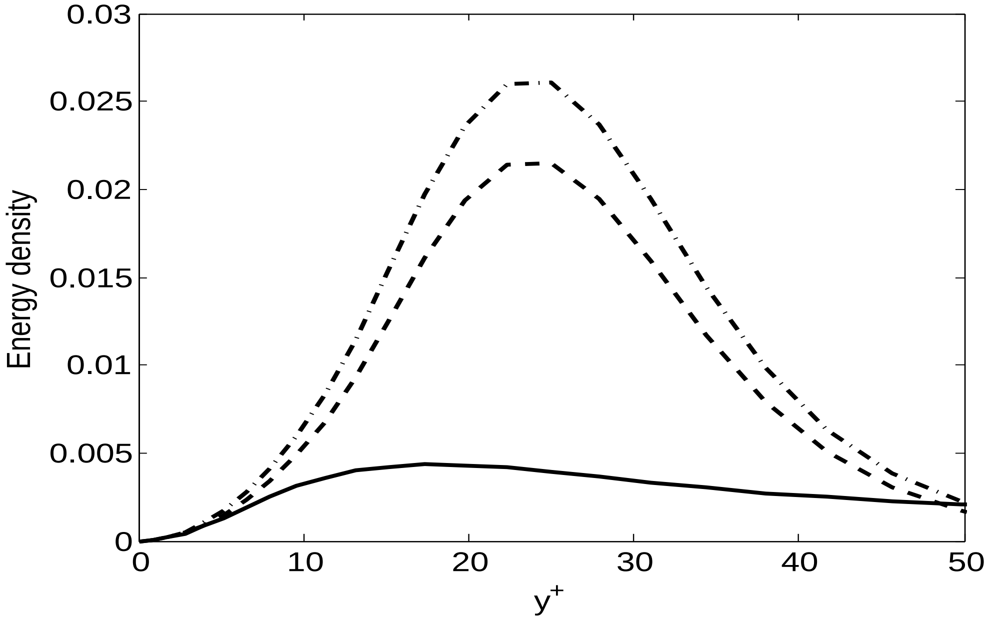

Figure 3.11: State energy density (solid), Wiener filter estimate (dashed) and Kalman filter estimate (dash-dotted) in the region $y^+ < 50$, evaluated for the array of wavenumber pairs $|\alpha| < \overline{\alpha}$ and $|\beta| < \overline{\beta}$. Measurement is spanwise skin friction. Results at $Re_\tau = 100$, $\phi_{dd} = 10^{-3}$.

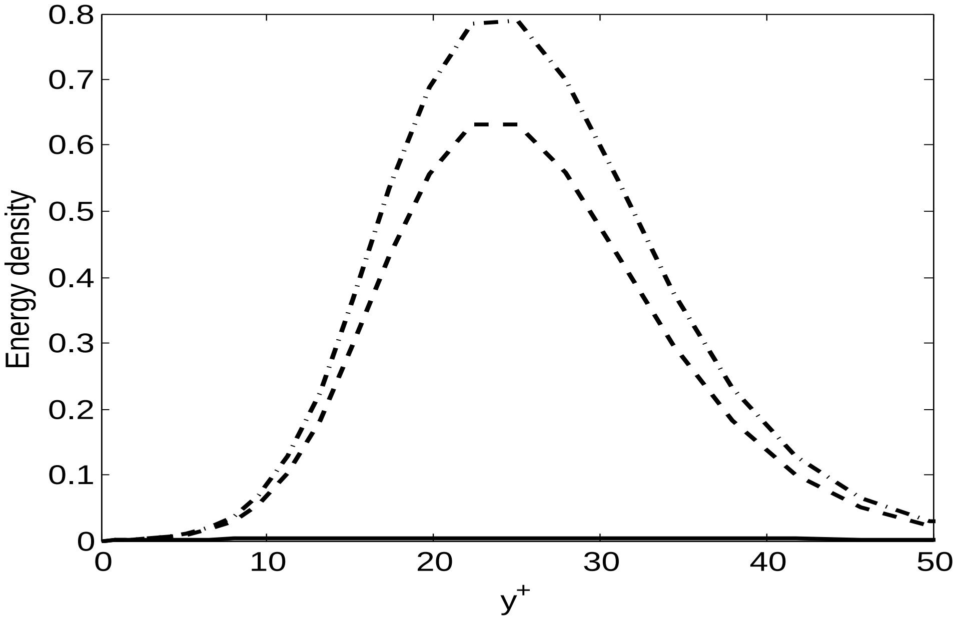

Figure 3.12: State energy density (solid), Wiener filter estimate (dashed) and Kalman filter estimate (dash-dotted) in the region $y^+ < 50$, evaluated for the array of wavenumber pairs $|\alpha| < \overline{\alpha}$ and $|\beta| < \overline{\beta}$. Measurement is wall pressure. Results at $Re_\tau = 100$, $\phi_{dd} = 10^{-3}$.

Chapter 4

Optimal compensator design: a Wiener-Hopf approach

The present chapter addresses the optimal compensator design problem. Leveraging the technique proposed in Chap. 3, this problem is stated in frequency domain. It will be shown that the approach presented here allows for the design of the optimal feedback compensator in one single step, without the need to resort to the separation theorem. After a brief discussion on the Internal Model Control (IMC) framework, the design procedure is outlined, and the Wiener-Hopf equation arising from it is discussed. Therefore, a recently proposed average linear model of the turbulent channel flow is presented and described; furthermore, statistics of the state noise - defined differently from Chap. 3 - are briefly presented. These informations are used in the design of optimal compensators, that are applied to turbulent channel flow for two values of the Reynolds number. Performance of such compensators, effects of design parameters and statistics of the controlled flow are discussed.

4.1 Frequency domain formulation of the optimal compensator design problem

4.1.1 Internal Model Control structure

The classical structure of a feedback control loop is depicted in fig. 4.1. In this figure, a compensator $K(s)$ feeds the system with an input signal u, computed on the basis of real-time measurements y. The *input-to-state* system transfer function is denoted with $H(s)$; the noise n typically accounts for unmodeled dynamics, while the disturbance d denotes measurements errors. Note that both the function $H(s)$ and the noise n are different from those defined in Chap. 1, fig. 1.3; in particular, the noise n acts on the state *downstream* the system's transfer function, while in Chap. 1 the noise was defined to act as an input to the dynamical system. The feedback loop in fig. 4.1 may be recast in the equivalent form shown in fig. 4.2; the

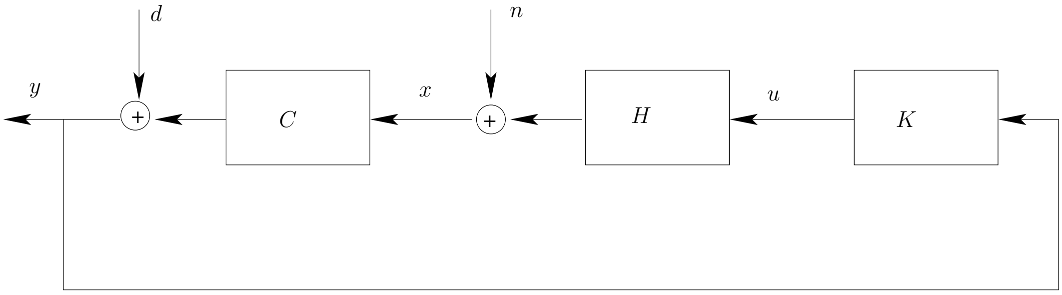

Figure 4.1: Classic feedback control loop.

compensator $\overline{K}$ is readily obtained by inspection as

$$\overline{K} = (I - KC\tilde{H})^{-1}K, \tag{4.1}$$

where $\tilde{H}$ is a *model* of the input-to-state transfer function of the system at hand. The explicit presence of a model of the process in the compensator transfer function gives to this structure the name of Internal Model Control (IMC) [90]. The feedback

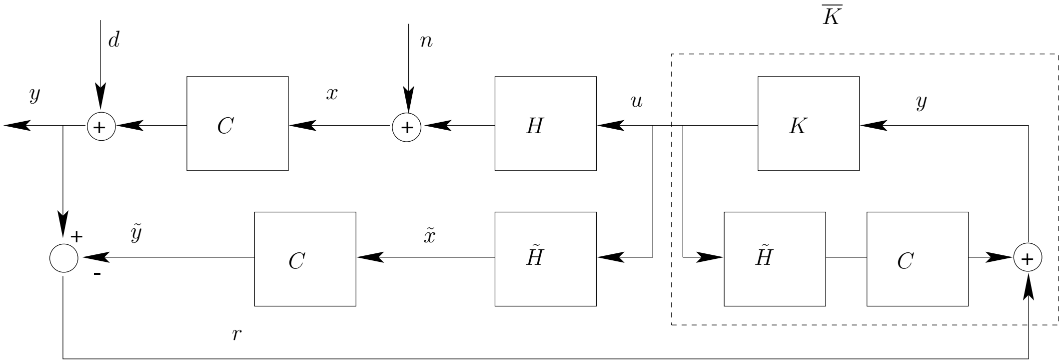

Figure 4.2: IMC feedback control loop.

signal r in fig. 4.2 is given by:

$$r = y - \tilde{y} = d + Cn + C(H - \tilde{H})u. \tag{4.2}$$

Eq. (4.2) shows that, in absence of noise, disturbance and modeling errors, the feedback signal is zero; this instructively highlights the important fact that, for open-loop stable systems, feedback is only required to compensate uncertainty.

4.1.2 Optimal compensator design in the IMC framework

Let us consider a multiple input-multiple output complex LTI system, characterized by an input-to-state frequency response function $H(f)$, and an output matrix C. Both the state and the measurements are corrupted by noise n and disturbances

d, respectively, as shown in fig. 4.1; moreover, noise and disturbances are uncorrelated and have known statistics. We assume that the input-to-state frequency response function is known exactly, i.e. uncertainty is accounted for in the terms n and d only. Furthermore, we restrict ourselves to the case when $H(f)$ is the frequency response function of an asymptotically stable system, i.e. the corresponding transfer function $H(s)$ is analytic in the closed right half of the complex plane.

The optimal compensator design problem is that of designing a frequency response function $K(f)$ that, based on the measurements, computes the optimal feedback input signal u that minimizes the usual LQG expectation functional

$$J = E\{x^H Qx + u^H Ru\}, \tag{4.3}$$

where the state and input weighting matrices, Q and R, are given constant design parameters. Wiener-Khintchine theorem and the properties of the trace operator can be used to rewrite the functional (4.3) in frequency domain:

$$J = \int_{-\infty}^{+\infty} Tr[Q\phi_{xx}(f)] + Tr[R\phi_{uu}(f)]\ df. \tag{4.4}$$

It is important to notice that substitution of the closed loop relations obtained by inspection of fig. 4.1 leads to a functional which is *not quadratic* in K; therefore, it is not possible to directly express the minimization of J with respect to K as a linear problem.

However, the IMC framework provides a convenient parametrization of all *stable* compensators K that ensure closed loop stability, by means of relation (4.1) [90]. The IMC closed loop system depicted in fig. 4.2, when $H = \tilde{H}$, is characterized by a feedback signal

$$r = d + Cn$$

which may be defined *uncontrolled output*. Noticing from fig. 4.2 that

$$y = (I + CH\overline{K})(d + Cn)$$

the closed-loop system in fig. 4.2 can be recast into an equivalent open loop form as in fig. 4.3, showing explicitly that the controlled (stable) system is driven by the noise n and the disturbance d.

The state x and input u can then be written as functions of the state noise n and measurement disturbance d as

$$\begin{aligned} x &= (I + H\overline{K}C)n + H\overline{K}d \\ u &= \overline{K}Cn + \overline{K}d, \end{aligned}$$

and, using relation (1.7), it is straightforward to obtain the spectral density functions

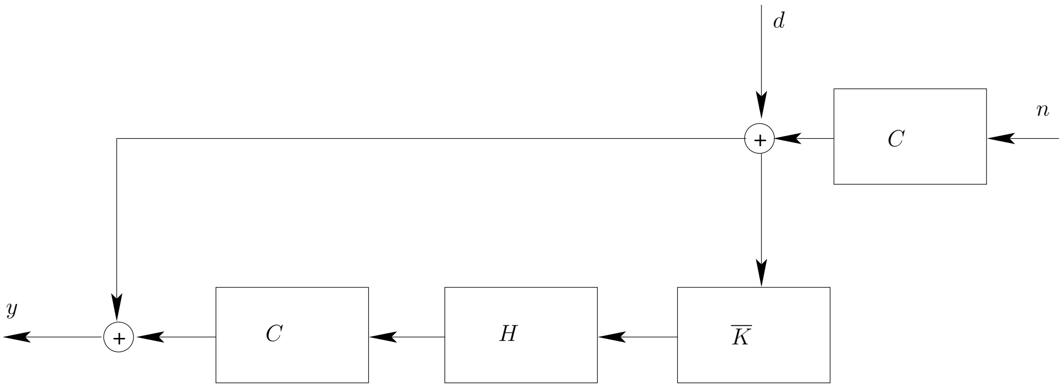

Figure 4.3: Equivalent open loop system

$\phi_{xx}(f)$ and $\phi_{uu}(f)$ as functions of $\phi_{nn}(f)$ and $\phi_{dd}(f)$. Substituting in (4.4) yields:

$$\begin{aligned} J = \int_{-\infty}^{+\infty} & Tr\Big\{Q\phi_{nn} + QH\overline{K}C\phi_{nn} + Q\phi_{nn}C^H\overline{K}^H H^H + \dots \\ & \dots + QH\overline{K}C\phi_{nn}C^H\overline{K}^H H^H + QH\overline{K}\phi_{dd}\overline{K}^H H^H\Big\} + \dots \\ & \dots + Tr\Big\{R\overline{K}C\phi_{nn}C^H\overline{K}^H + R\overline{K}\phi_{dd}\overline{K}^H\Big\}\, df. \end{aligned} \tag{4.5}$$

It is noteworthy that this expression of the functional J is *quadratic* in $\overline{K}$; therefore, minimization of this functional with respect to $\overline{K}$ leads to a *linear* problem for $\overline{K}$, and the original compensator K can be recovered from (4.1). In particular, minimization of the functional in (4.5) with respect to $\overline{K}$ leads to the best possible LTI compensator for the problem at hand. However, this compensator would be *noncausal*, i.e. it would require both future and past informations from the measurements to provide the optimal feedback signal. Causality is a fundamental requirement for filters to be applied real-time in feedback applications. In a fashion analogous to that reported in Chap. 3, causality is enforced by introducing an appropriate Lagrange multiplier and using Parseval theorem, rewriting J as:

$$\begin{aligned} J = \int_{-\infty}^{+\infty} & Tr\Big\{Q\phi_{nn} + QH\overline{K}_+C\phi_{nn} + Q\phi_{nn}C^H\overline{K}_+^H H^H \dots \\ & \dots + QH\overline{K}_+C\phi_{nn}C^H\overline{K}_+^H H^H + QH\overline{K}_+\phi_{dd}\overline{K}_+^H H^H\Big\} + \dots \\ & \dots + Tr\Big\{R\overline{K}_+C\phi_{nn}C^H\overline{K}_+^H + R\overline{K}_+\phi_{dd}\overline{K}_+^H\Big\} + Tr[\Lambda_-\overline{K}_+^H]\, df. \end{aligned} \tag{4.6}$$

Setting to zero the gradient of (4.6) with respect to $\overline{K}_+^H$ yields the following Wiener-Hopf equation:

$$(H^HQH + R)\overline{K}_+(C\phi_{nn}C^H + \phi_{dd}) + \Lambda_- = -H^HQ\phi_{nn}C^H \tag{4.7}$$

When this equation is solved for $\overline{K}_+$, the original compensator can be recovered by inverting the parametrization (4.1):

$$K = \overline{K}(I + CH\overline{K})^{-1}. \tag{4.8}$$

This formulation has been first proposed by Luchini [79]. Related approaches have been presented in the past by Youla and coworkers [139; 140] for the case of processes described by rational (scalar or matrix) transfer functions.

A brief discussion of the fundamental features of the present formulation is in order. The present strategy is *exactly* a restatement of the LQG design problem for asymptotically stable systems in the frequency domain; note also that the symmetry of the coefficients appearing in the Wiener-Hopf equation (4.7) highlights the dual nature of the control and estimation problems. The state-space formulation of the optimal compensator problem leverages the separation theorem to solve for the controller and the estimator; in the present approach, the frequency response function of the full compensator is designed in one single step. This feature is particularly relevant when the system is single input-single output; in this case, the Wiener-Hopf equation (4.7) is *scalar*, and can be solved very efficiently by using a Fourier-transform-based approach. This solution technique is particularly advantageous from the numerical viewpoint, if compared to standard Riccati-based strategies. In the general case of multiple input-multiple output system, the Wiener-Hopf problem can be solved in the time domain by discretizing the corresponding integral equation and factorizing an appropriate Toeplitz matrix.

It is worth noting that the spectra of the noise n and of the disturbance d appear in their functional form in the coefficients of the equation. Therefore, these noises need not be white, and accounting for the time structure of the noise and disturbance becomes straightforward. This is a key feature that allows to take into account modeling errors in the term n by using directly the *measured* statistics of n, instead of forcing the statistics to obey the dynamics of the system (as in the Kalman approach). In a similar manner, it is straightforward to introduce a frequency-dependent weighting as well as the dynamics of the sensors by letting C depend on the frequency.

From the computational viewpoint, the construction of the coefficients in (4.7) requires the input-to-state frequency function of the system, $H(f)$, and the term $C\phi_{nn}(f)$, which corresponds to the cross-spectrum between the noise n and its measurements; equivalently, the cross-correlation between state noise and its measurements may be available. These two quantities can be computed by using DNS or, in certain situations, may be obtained experimentally.

4.1.3 Analytical example

Let us consider the following scalar, stable system:

$$\begin{aligned}\dot{x} &= -x + u + w\\ y &= x + v.\end{aligned}$$

The design problem is stated as the search of a feedback compensator that minimizes the expectation:

$$J = E\{x^2 + u^2\}$$

when w and v are white Gaussian noises having unit intensity. Standard LQG theory reviewed in Chap. 2 provides straightforwardly the result: both Riccati equations associated to the control and estimation problems read

$$p^2 + 2p - 1 = 0$$

and the stabilizing solution is $p = -1 + \sqrt{2}$. The state-space representation of the compensator reads

$$\begin{aligned}\dot{o} &= (1 - 2\sqrt{2})o + (\sqrt{2} - 1)y\\ u &= (1 - \sqrt{2})o\end{aligned}$$

and the corresponding frequency response function reads

$$K_{LQG}(j\omega) = -\frac{(\sqrt{2}-1)^2}{j\omega - 1 + 2\sqrt{2}}. \tag{4.9}$$

Let us now follow the approach outlined in the previous section. Notice that the state noise n, as reported in fig. 4.1, acts after the system dynamics. Therefore, its spectral density function may be directly computed from that of w by means of relation (1.7):

$$\phi_{nn}(j\omega) = \frac{1}{\omega^2 + 1}.$$

Upon substitution of the system frequency response in (4.7) one obtains the following Wiener-Hopf equation:

$$\frac{(\omega^2+2)^2}{(\omega^2+1)^2}\overline{K}_+ + \Lambda_- = -\frac{1}{-j\omega+1}\frac{1}{\omega^2+1}$$

which is the same as the one reported in the example (3.13). Therefore, its solution reads

$$\overline{K}_+(j\omega) = -\frac{(j\omega+1)}{(\sqrt{2}+1)^2(j\omega+\sqrt{2})^2}$$

and the frequency response of the Wiener-Hopf compensator can be recovered from (4.8), to obtain:

$$K_{WH}(j\omega) = -\frac{(\sqrt{2}-1)^2}{j\omega - 1 + 2\sqrt{2}}, \tag{4.10}$$

which is the same result as in (4.9).

4.2 The average linear response of a turbulent channel flow to wall forcing

Any linearized stable model of the flow system, given in the form of impulse response function (or, equivalently, frequency response function), can be used in the IMC framework outlined in the previous section; for instance, it may be obtained from a state-space form of the dynamical equations of the system at hand. In the present work, we use a recently proposed linearized model of the wall-forced turbulent channel flow [81] that represents, at a given Re, the average dynamics of the turbulent flow when impulsive wall forcing is applied. Definition of this *average linear response* is given in the following, and its numerical measurement is detailed.

4.2.1 Definition

We consider small perturbations to the statistically stationary turbulent channel flow in the form of non-homogeneous boundary conditions on the i-th component of the velocity at the walls, denoted by $u_{i,w}$. We assume that such perturbations are statistically stationary space-time white Gaussian noises, i.e. their autocorrelation function reads:

$$E\{u_{i,w}(x+\Delta x, z+\Delta z, t+\Delta t)u^*_{i,w}(x,z,t)\} = \delta(\Delta x, \Delta z, \Delta t)$$

In the linear setting, these perturbations have a small effect on the velocity field; hence, the perturbed field can be decomposed as

$$\begin{aligned} v_{tot}(x,y,z,t) &= \overline{v}(x,y,z,t) + v(x,y,z,t) \\ \eta_{tot}(x,y,z,t) &= \overline{\eta}(x,y,z,t) + \eta(x,y,z,t) \end{aligned}$$

where $\overline{v}, \overline{\eta}$ is the unperturbed flow field and v, η is the small perturbation due to wall forcing. The cross-correlation between the perturbed field and the wall forcing reads:

$$\begin{aligned} &E\{v_{tot}(x'+x, y, z'+z, t'+t)u^*_{i,w}(x',z',t')\} = \dots \\ &\qquad \dots \underbrace{E\{\overline{v}(x'+x, y, z'+z, t'+t)u^*_{i,w}(x',z',t')\}}_{=0} + \dots \\ &\qquad \dots + E\{v(x'+x, y, z'+z, t'+t)u^*_{i,w}(x',z',t')\} \\[1em] &E\{\eta_{tot}(x'+x, y, z'+z, t'+t)u^*_{i,w}(x',z',t')\} = \dots \\ &\qquad \dots \underbrace{E\{\overline{\eta}(x'+x, y, z'+z, t'+t)u^*_{i,w}(x',z',t')\}}_{=0} + \dots \\ &\qquad \dots + E\{\eta(x'+x, y, z'+z, t'+t)u^*_{i,w}(x',z',t')\} \end{aligned} \tag{4.11}$$

and the first terms on the right hand sides vanish because the undisturbed turbulent flow and the wall forcing are uncorrelated, being generated by different physical processes. In the linear setting, both the wall forcing and the perturbation fields are statistically stationary; hence, we can define the second terms on the right hand side as

$$\begin{aligned} H_{v,i}(x,y,z,t) &= E\{v(x'+x,y,z'+z,t'+t)u^*_{i,w}(x',z',t')\} \\ H_{\eta,i}(x,y,z,t) &= E\{\eta(x'+x,y,z'+z,t'+t)u^*_{i,w}(x',z',t')\}. \end{aligned} \tag{4.12}$$

It is well known from system theory that the input-output cross-correlation of a LTI system driven by a unit intensity white Gaussian noise equals the impulse response of the system. Hence, eq. (4.12) *defines* a linear time-invariant system representing the average response of the perturbation field v, η when driven by a (small) input $u_{i,w}$ at the walls.

The definitions in eq. (4.12) and (4.11) provide a convenient way to compute the response function, as noted by Luchini et al. in [81]. Exploiting the usual ergodicity assumption:

$$\begin{aligned} &H_{v,i}(x,y,z,t) = \dots \\ &\dots = \frac{1}{L_x L_z}\int_0^{L_x}\int_0^{L_z}\int \!\!\!\!\!\! M v_{tot}(x'+x,y,z'+z,t'+t)u^*_{i,w}(x',z',t')\,dt'\,dx'\,dz' \approx \dots \\ &\dots \approx \frac{1}{L_x L_z}\int_0^{L_x}\int_0^{L_z}\frac{1}{T}\int_0^{T} v_{tot}(x'+x,y,z'+z,t'+t)u^*_{i,w}(x',z',t')\,dt'\,dx'\,dz'. \end{aligned}$$

Hence, sampling on M discrete time points such that $T = M\Delta t$:

$$\begin{aligned} &H_{v,i}(x,y,z,p\Delta t) \approx \dots \\ &\dots \approx \frac{1}{L_x L_z}\int_0^{L_x}\int_0^{L_z}\frac{1}{M}\sum_{k=0}^{M-1} v_{tot}(x'+x,y,z'+z,(k+p)\Delta t)u^*_{i,w}(x',z',k\Delta t)\,dx'\,dz' \\ &\text{for} \quad p = 0,\dots,N. \end{aligned}$$

Fourier-transforming in homogeneous directions and rearranging indexes in the summation yields

$$\begin{aligned} &\hat{H}_{v,i}(\alpha,y,\beta,p\Delta t) \approx \frac{1}{M}\sum_{q=p}^{M-1+p} \hat{v}_{tot}(\alpha,y,\beta,q\Delta t)\hat{u}^*_{i,w}(\alpha,\beta,(q-p)\Delta t) \\ &\text{for} \quad p = 0,\dots,N,\ \forall \alpha,\beta. \end{aligned} \tag{4.13}$$

Eq. (4.13) provides an efficient way to compute the response function runtime, while performing a direct numerical simulation of the turbulent channel flow perturbed by white-noise wall forcing; a sufficiently long computation averages out the correlation between the unperturbed flow and the wall forcing in eq. (4.11), thus leading to the response function defined in (4.12).

4.2.2 Potential component of the response

Assume that the impulsive forcing at the wall, in a generic realization, has the form

$$v(x,-1,z,t) = \delta(x,z,t),$$

i.e. is applied on the wall-normal velocity at the wall. The velocity field $\mathbf{V}_0$ at the time of the impulsive forcing is divergence-free but does not satisfy the compatibility relations with the boundary data, since

$$\mathbf{V}_0 \cdot \mathbf{n} = 0 \neq \delta(x,z).$$

The incompressibility constraint causes the velocity field to instantaneously adapt to the impulsive wall forcing, correcting the field $\mathbf{V}_0$ with an irrotational field as

$$\mathbf{U}_0 = \mathbf{V}_0 + \nabla\phi.$$

$\mathbf{U}_0$ is divergence-free and satisfies the impulsive boundary conditions, while ϕ is referred to as the *correction potential* [75; 131]. The equation for ϕ can be derived from:

$$\begin{aligned} \nabla \cdot \mathbf{U}_0 = 0 \rightarrow \nabla \cdot \mathbf{V}_0 + \nabla \cdot \nabla\phi = 0 \rightarrow \Delta\phi = 0 \\ \mathbf{U}_0 \cdot \mathbf{n} = \mathbf{V}_0 \cdot \mathbf{n} + \nabla\phi \cdot \mathbf{n} = \delta(x,z) \rightarrow \nabla\phi \cdot \mathbf{n} = \delta(x,z) \end{aligned}$$

Fourier-transforming in homogeneous directions yields the following set of equations

$$\begin{aligned} \Big(\frac{d^2}{dy^2} - k^2\Big)\hat{\phi} &= 0 \qquad \forall \alpha,\beta \\ \hat{\phi}'(\alpha,-1,\beta) &= 1 \\ \hat{\phi}'(\alpha,1,\beta) &= 0 \end{aligned}$$

whose solution (up to an arbitrary constant) reads:

$$\hat{\phi}(\alpha,y,\beta) = -\frac{\cosh(k(1-y))}{k\sinh(2k)} \qquad k^2 = \alpha^2 + \beta^2; \tag{4.14}$$

furthermore, note that $\phi = 0$ is imposed at $k = 0$, in order to satisfy the integral incompressibility constraint. It is noteworthy that ϕ is deterministic and does not depend either on $\mathbf{V}_0$ or on Re, whereas the full response depends on Re for $t > 0$.

4.2.3 Numerical measurement of the response function

Two well resolved direct numerical simulations, at $Re_\tau = 100$ and $Re_\tau = 180$, have been performed to numerically measure the response function (4.12) to wall forcing with the wall-normal velocity component. The simulations are run using a modified turbulent channel flow solver, that provides zero-mean time and space random forcing on the v component at the lower wall. Specifically, random numbers

	Box size		Resolution				Response parameters			
Re_τ	L_x	L_z	N_x	N_z	N_y	Δt^+_{sim}	T^+	Δt^+	T^+_{av}	A_f
100	4π	2π	64	64	64	0.125	100	0.5	100000	0.0005
180	4π	$4/3\,\pi$	96	64	128	0.15	60	0.75	75000	0.000125

Table 4.1: Parameters used in the numerical measurement of the average linear response to wall forcing with wall-normal velocity; Δt_{sim} is the time step size employed in the simulations, while N_y is the number of discretization points in wall-normal direction.

are generated to provide, every time step Δt of the discretized response, random phase to the Fourier coefficients of wall-normal velocity at the wall. The small forcing amplitude A_f is constant in wavenumber space, and has been chosen in order for the perturbations to remain in the linear regime; the values chosen have been suggested by the previous linearity parametric study by Luchini et al. [81]. Simulations are performed using a constant time step Δt_{sim}. The cross-correlation between the perturbed flowfield and the white noise forcing at the wall is computed runtime, in order to perform a running average having length T_{av} to determine the response function. Further details about the domain and the space and time resolution of the simulations are reported in table 4.1. These simulations required approximately 2 months on 24 AMD Opteron quad-core machines, available on a dedicated cluster at the University of Salerno.

Potential component

The numerically measured response functions correctly reproduce the potential component of the response function. Fig. 4.4 compares the measured v-component of the response function at $t = 0$ ($H_{v,v}(x, y, z, 0)$) with the v-component of the velocity field obtained from the gradient of (4.14), for the case $Re_\tau = 100$. With the averaging time employed, agreement between the numerical result (a) and analytical solution (b) is shown; surfaces correspond to 10% of the maximum value in the volume, which is, in the measured case, $\approx 94\%$ of the analytical maximum. A similar agreement is obtained when comparing the analytical solution with the potential solution in the case $Re_\tau = 180$, in accordance with the observation that the potential response is Reynolds number independent; in this latter case, the measured maximum is $\approx 93\%$ of the analytical maximum.

Physical space representation of the response

A physical space representation of the measured response function is depicted in fig. 4.5 and 4.6, for the $Re_\tau = 100$ case. Figures correspond to two time instants, namely, $t^+ = 5$ and $t^+ = 15$; in these figures, flow is from bottom-left to top-right. Light and dark surfaces correspond to positive and negative values, respectively. These figures show that the v component of the response is symmetric

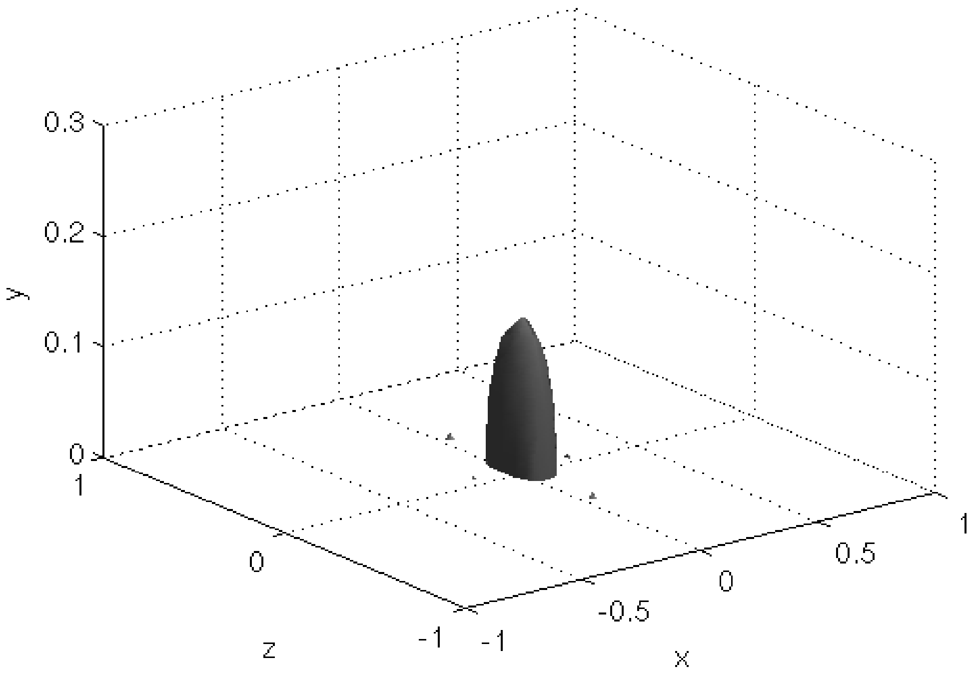

(a)

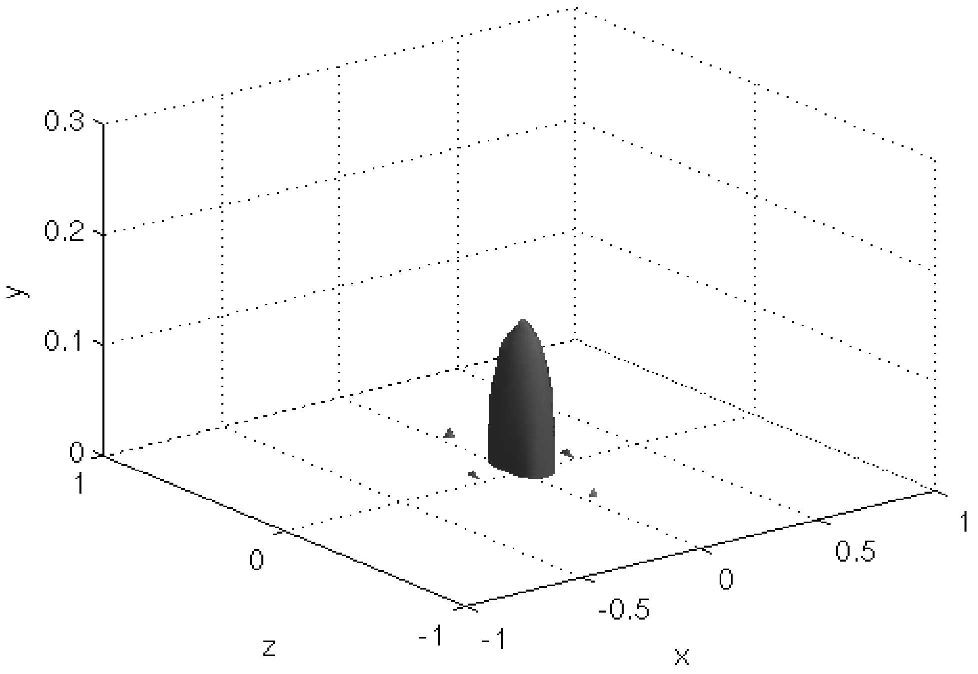

(b)

Figure 4.4: Potential component of the average linear response of the turbulent channel flow to wall forcing with the v component, $Re_\tau = 100$; represented is the lower half channel, in the subset $x \in [-1, 1], \;\; z \in [-1, 1]$. (a): $H_{v,v}(x, y, z, 0)$ computed numerically; (b): analytical solution. Isosurfaces at the 10% of the maximum value, which in the measured case is $\approx 94\%$ of the one in the analytical case.

(on average) with respect to the $x - y$ plane, while the η component is antisymmetric. The average impulse response field is convected downstream by the flow; since this impulse response is, by construction, that of a stable system, it asymptotically goes to zero as time goes to infinity. This is coherent with the fact that, at fixed averaging time, the signal-to-noise ratio decreases with time because the response amplitude decreases, while the background noise is constant; therefore, it is necessary to increase the level of the isosurface in the figures in order to highlight the average deterministic part. But for the potential part of the response, which is defined in the whole domain, it appears that the average linear response is localized in the near-wall region. Similar features were noted in [81], for a response computed at $Re_\tau = 180$. Furthermore, in that work it was also shown that the decay rate of the average response is significantly faster than that of either the laminar response, or of the so-called pseudo-turbulent response (obtained from the Orr-Sommerfeld-Squire equations linearized about the mean turbulent profile). This feature is due to the capability of the average linear response to account for the average effect of turbulent diffusion on the velocity field generated by the impulsive forcing.

Spectral space representation of the response

Absolute values of the Fourier coefficients of the response at the representative values of $y^+ = 10$ and $t^+ = 15$ are reported against the wavenumber pair (α, β) in fig. 4.7 (a) and (b), for the case $Re_\tau = 100$. Figures show that the response function is localized in spectral space; this feature was found in the near wall region up to $y^+ \approx 30$, for the two values of Re considered. As far as the time window where the response function is significant is concerned, fig. 4.8 shows the energy norm $||H||_E$ as a function of time, for the two Re considered; after the initial instant – corresponding to the potential response – it is found that the energy norm of the response decreases with time and tends to saturate at $t^+ \approx 50$ for both Re, suggesting that for larger time separations the energy is due to the background noise that has not been averaged out yet.

4.3 State noise measurements

It has been noted in Sec. 4.1 that the solution of the compensator design problem requires the knowledge of the cross-correlation between the state noise and its wall measurements in the *uncontrolled* flow:

$$\begin{aligned} R_{\hat{\tau}_x,\hat{n}} &= E\{\hat{\tau}_x(t+\tau)\hat{n}^H(y,t)\} \\ R_{\hat{\tau}_z,\hat{n}} &= E\{\hat{\tau}_z(t+\tau)\hat{n}^H(y,t)\} \\ R_{\hat{p},\hat{n}} &= E\{\hat{p}(t+\tau)\hat{n}^H(y,t)\} \end{aligned}$$

for each (α, β); note that, using the state variables introduced in Chap. 2, the noise term may be splitted as $\hat{n} = (\hat{n}_v,\ \hat{n}_\eta)^T$, emphasizing the terms acting on the velocity

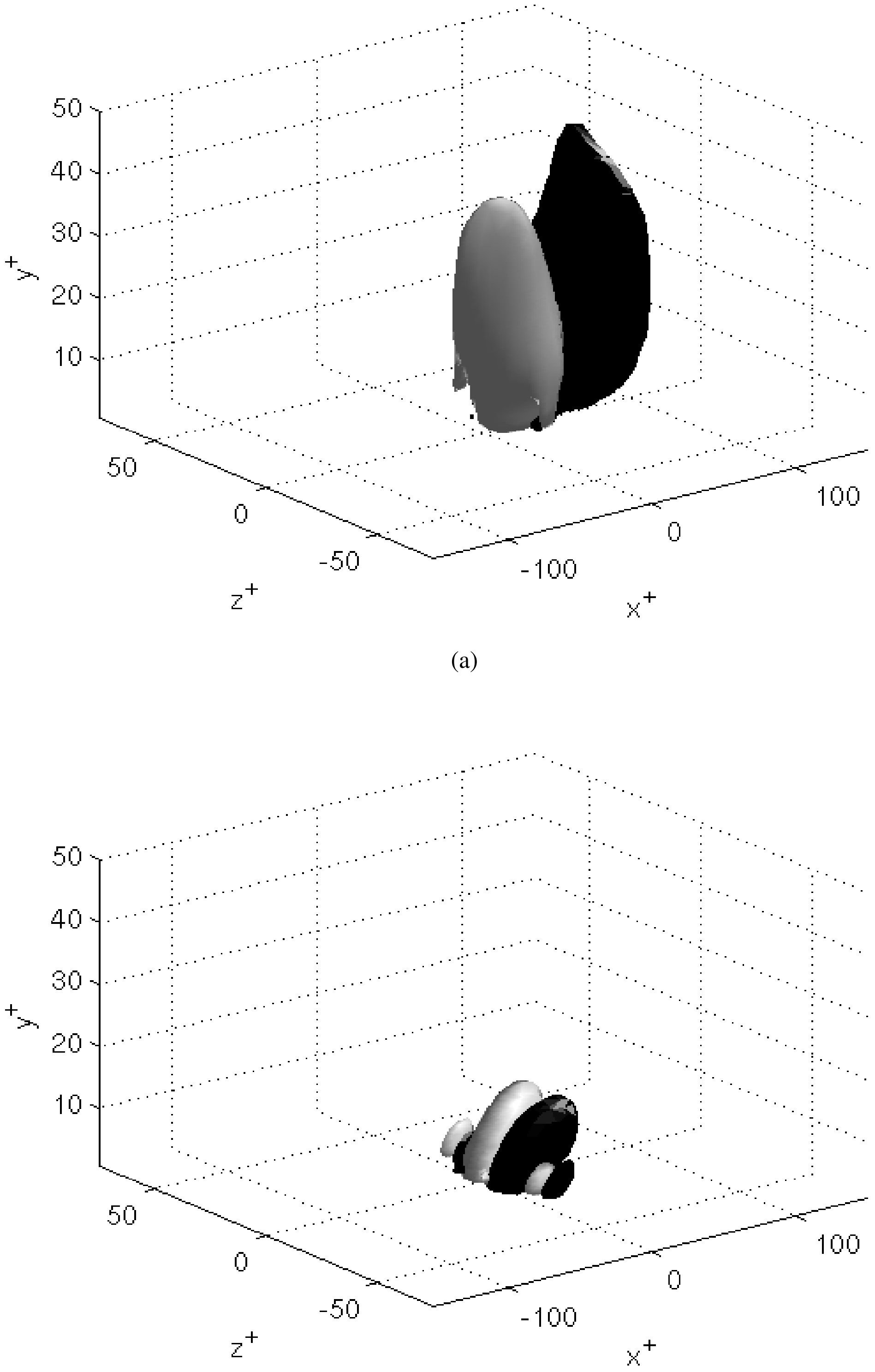

(a)

(b)

Figure 4.5: Average linear response of the turbulent channel flow to lower wall forcing with the v component, $Re_\tau = 100$; represented is the lower half channel, in the subset $x^+ \in [-150, 150]$, $z^+ \in [-75, 75]$. (a): $H_{v,v}(x, y, z, t^+ = 5)$, isosurfaces at $\pm 8\%$ of the maximum value (light to dark gray); (b): $H_{\eta,v}(x, y, z, t^+ = 5)$, isosurfaces at $\pm 8\%$ of the maximum value (light to dark gray).

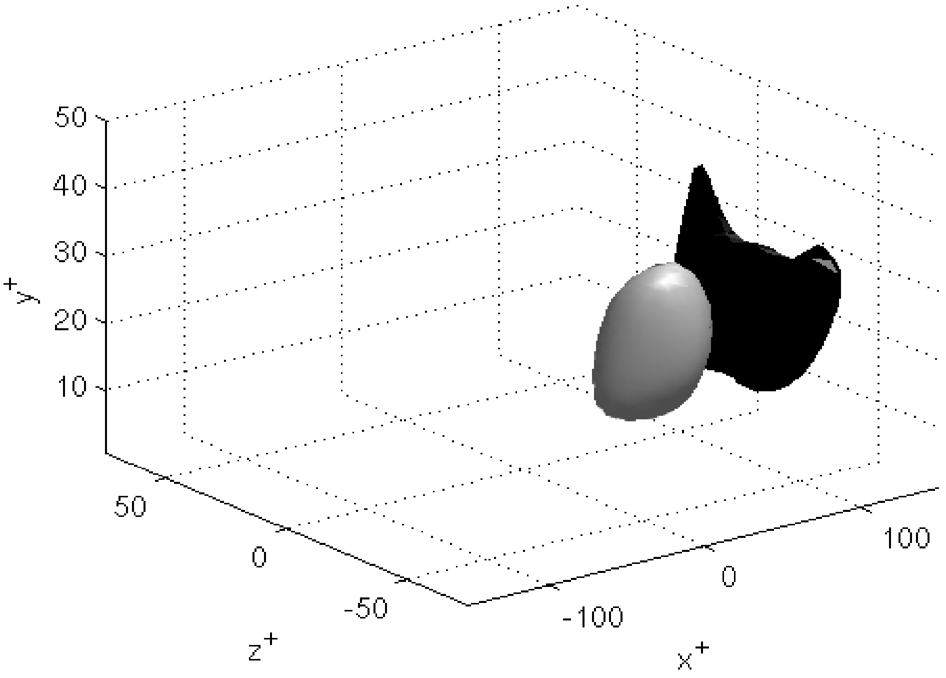

(a)

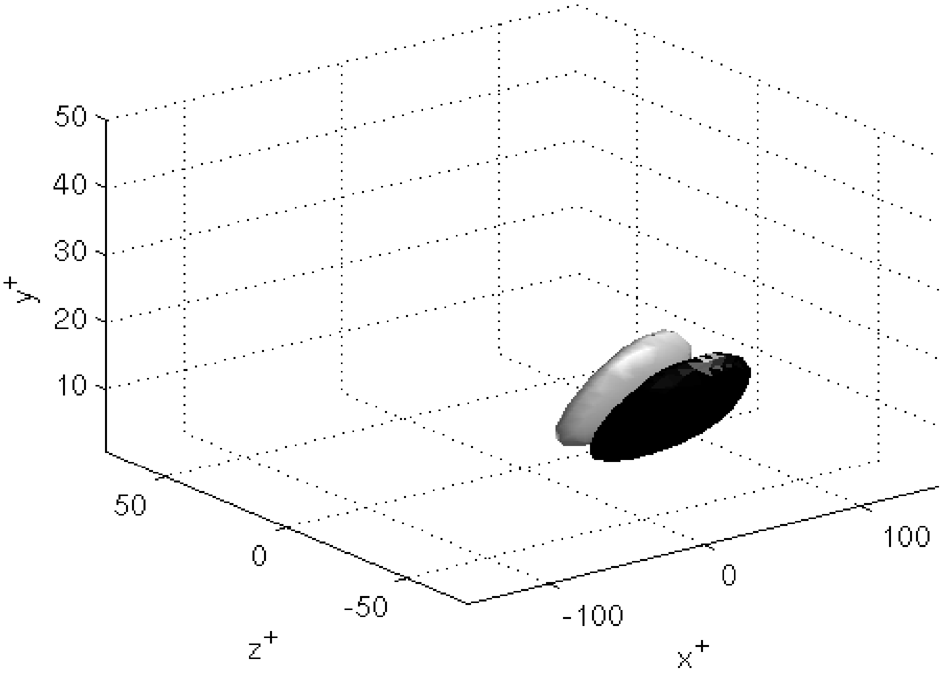

(b)

Figure 4.6: Average linear response of the turbulent channel flow to lower wall forcing with the v component, $Re_\tau = 100$; represented is the lower half channel, in the subset $x \in [-150, 150]$, $z \in [-75, 75]$. (a): $H_{v,v}(x, y, z, t^+ = 15)$, isosurfaces at $\pm 40\%$ of the maximum value (light to dark gray); (b): $H_{\eta,v}(x, y, z, t^+ = 15)$, isosurfaces at $\pm 40\%$ of the maximum value (light to dark gray).

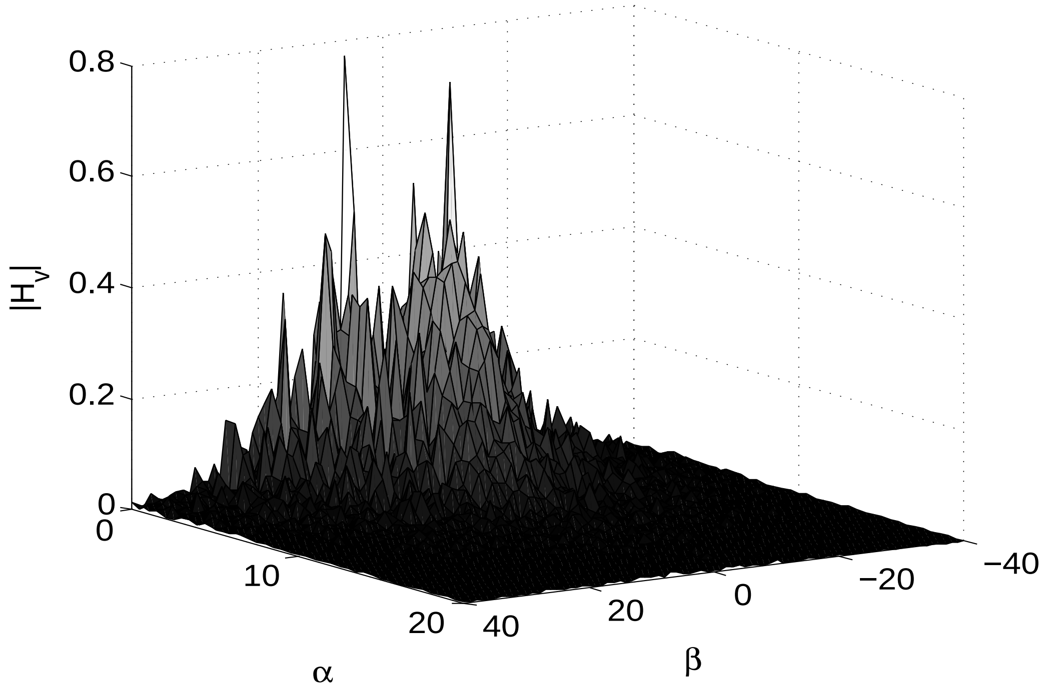

(a)

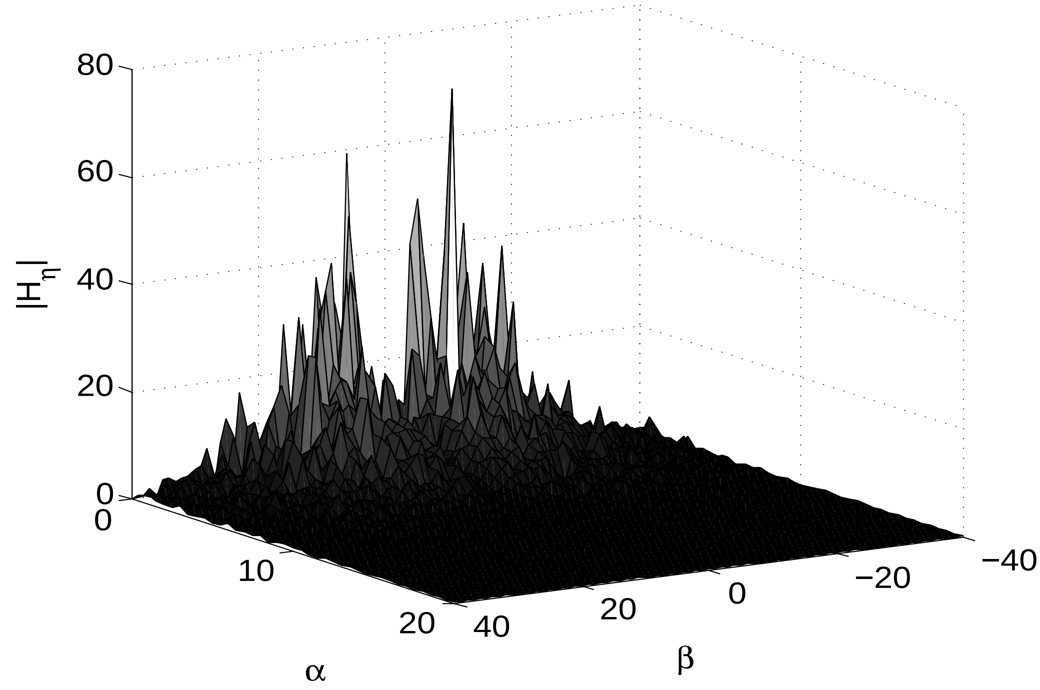

(b)

Figure 4.7: (a) Absolute value of the Fourier coefficients of $\hat{H}_{v,v}(\alpha, \beta; y^+ = 10; t^+ = 15)$; (b) absolute value of the Fourier coefficients of $\hat{H}_{\eta,v}(\alpha, \beta; y^+ = 10; t^+ = 15)$. Results for the average linear response computed at $Re_\tau = 100$. The subset $\alpha \in [0; 20]$ and $\beta \in [-40; 40]$ is represented. Only the half-plane $\alpha \geq 0$ is represented because of the Hermitian symmetry of the (real) response function.

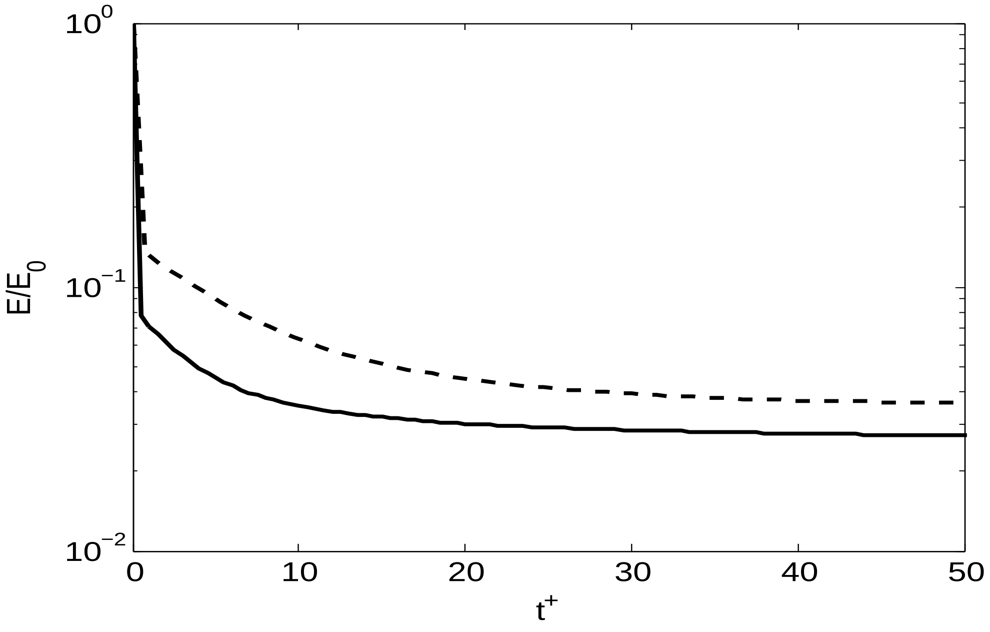

Figure 4.8: Normalized energy of the response functions at $Re_\tau = 100$ (solid) and $Re_\tau = 180$ (dashed). Energy of the responses eventually saturates at $t^+ \approx 50$.

	Box size		Resolution			Noise parameters	
Re_τ	L_x	L_z	N_x	N_z	N_y	Δt^+_{noise}	T^+_{noise}
100	4π	2π	64	64	64	0.5	100
180	4π	$4/3\,\pi$	96	64	128	0.75	150

Table 4.2: Parameters used in the numerical measurement of the state noise-measurement correlation.

and vorticity equations. This information can be computed runtime from a DNS of a turbulent channel, or in a post-processing step. Note that this correlation has the important advantage that the independent variables are 4 (namely, α, β, y, τ) in contrast to the state-noise information used in Chap. 3 in the design of the Wiener filter where the independent variables were 5; this feature reduces the dimensionality of the problem, and allows for easier handling of the corresponding database.

The state noise-measurement correlations have been computed for $Re_\tau = 100$ and $Re_\tau = 180$. Parameters of the discretization in the channel flow simulations, as well as time resolution Δt_{noise} and maximum time window $[-T_{noise}, T_{noise}]$ are reported in table 4.2. The spatial structure of the computed state noise-measurement correlation is reported in fig. 4.9, 4.10 and 4.11, at zero time lag; surfaces of constant value at 20% of the maximum are represented. As may be expected, the v part of the state noise-measurement correlations with τ_x and p is statistically symmetric with respect to the $x-y$ plane, while the η part is antisymmetric. Conversely, the v part of the state noise-measurement correlations with τ_z is antisymmetric with respect to the $x-y$ plane, while the η part is symmetric. These correlations are localized in space, meaning that measurements with either one of the available wall quantities at a given point are correlated to the flow state up to a certain extent in wall-normal, streamwise and spanwise direction. This feature is directly inherited by the autocorrelation of wall measurements, as highlighted in recent work [57; 102]. These works also quantified the extent of such autocorrelations as a function of the time separation; again, this feature is directly inherited by the time structure of the correlations computed in the present work, which is exemplified, for a given wall-normal position, in fig. 4.12.

4.4 Single input - single output optimal compensators: a parametric study

Optimal compensators are designed for the single input-single output case with drag reduction purposes. Actuation is performed with the wall-normal velocity component at the lower wall, and either one of the wall shear stress components or pressure are measured. As noted in the previous sections, this case requires the solution of a scalar Wiener-Hopf problem for each wavenumber pair; this feature allows us to perform a wide parametric study of the effectiveness of compensators, with limited computational effort at the compensator design stage.

4.4.1 Compensator kernels

Compensators are designed for $Re_\tau = 100$ and $Re_\tau = 180$. Two different state weighting matrices are used in the cost functional (2.13), corresponding to the energy and dissipation norms of the state. Additional weighting in wall-normal direction of the energy (as suggested, for instance, in [50]) is not employed here. The "tunable" parameters in the control design are the control weight, R, and the measurement noise intensity, ϕ_{dd}.

Leveraging the fact that the average response function of the turbulent channel flow is localized in spectral space (see Sec. 4.2), optimal compensators are designed for a reduced set of wavenumbers, $|\alpha| \leq \overline{\alpha}$, $|\beta| \leq \overline{\beta}$. The response functions used for the compensator design are those described in Sec. 4.2, as well as the state noise-measurement correlations are those presented in Sec. 4.3. Prior to Fourier transformation to frequency domain, both the response function and the state noise correlations are windowed with a `cos` function, to prevent leakage and smooth out the noise at large separation times. After completing the design in frequency domain of these optimal compensators, their frequency response is inverse Fourier transformed to obtain the corresponding impulse response function. Instead of developing a minimal state space realization for the optimal compensator (whose equations would be integrated together with the flow equations), the control action

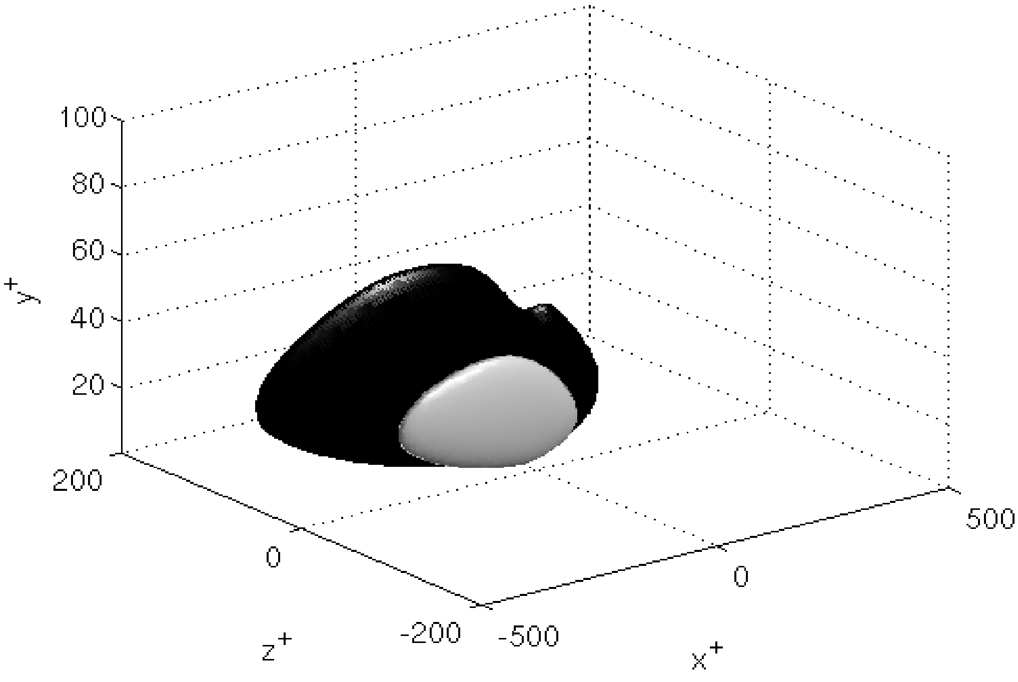

(a)

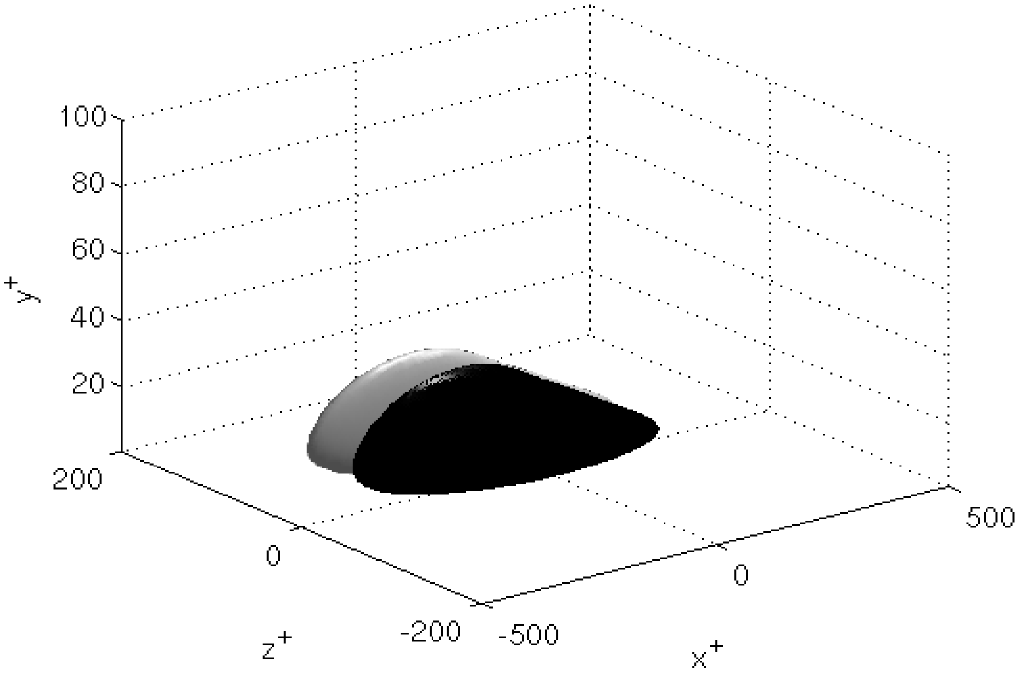

(b)

Figure 4.9: Surfaces at $\pm 25\,\%$ (light-dark gray,respectively) of the maximum for the state noise-measurement correlation, at zero time lag. Measurement is streamwise wall friction τ_x; (a) v component; (b) η-component. Dependent variables x, y and z normalized with viscous units. Results at $Re_\tau = 100$, $x^+ \in [-500, 500]$, $z^+ \in [-200, 200]$.

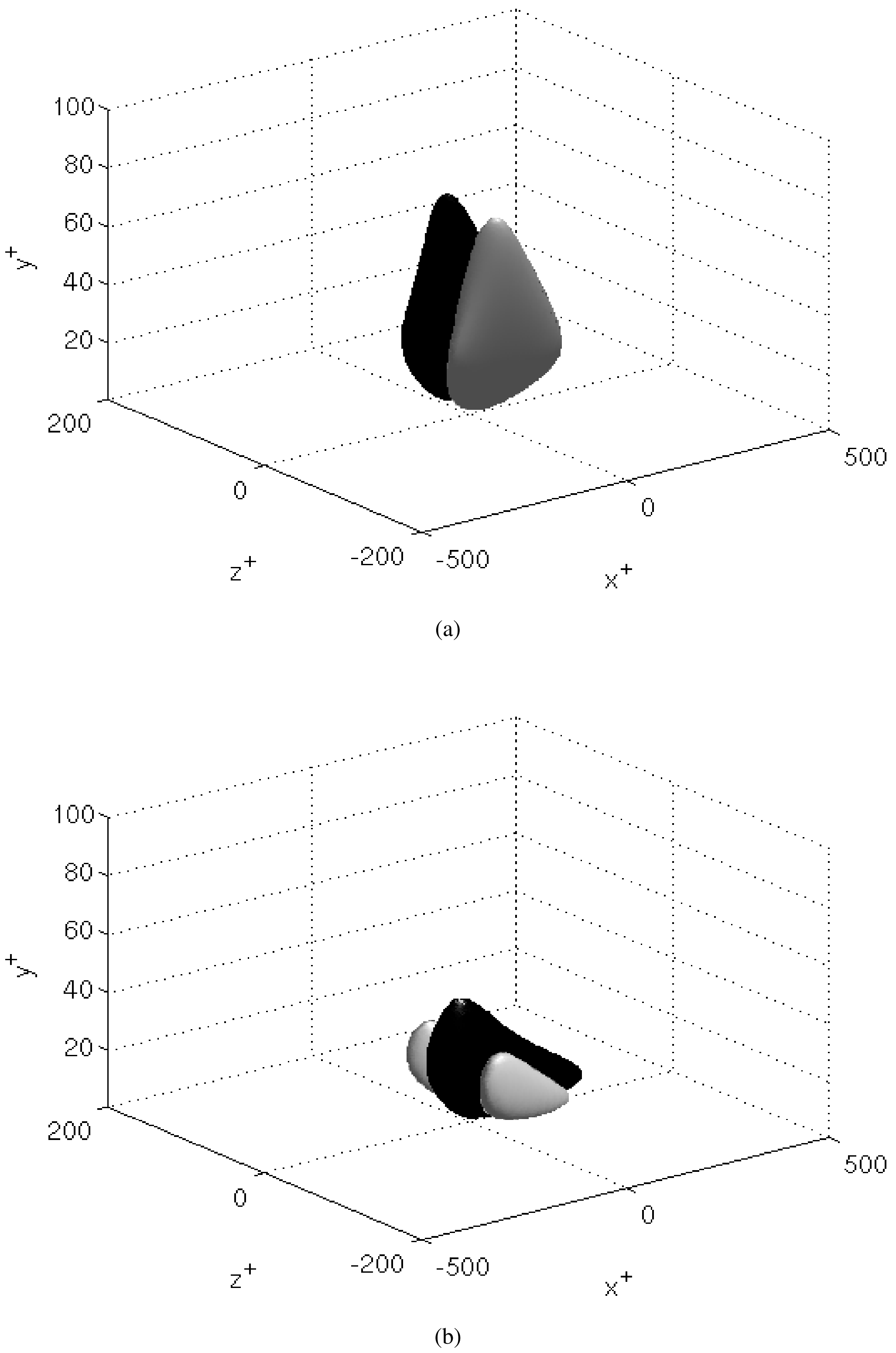

(a)

(b)

Figure 4.10: Surfaces at $\pm 25\,\%$ (light-dark gray,respectively) of the maximum for the state noise-measurement correlation, at zero time lag. Measurement is spanwise wall friction τ_z; (a) v component; (b) η-component. Dependent variables x, y and z normalized with viscous units. Results at $Re_\tau = 100$, $x^+ \in [-500, 500]$, $z^+ \in [-200, 200]$.

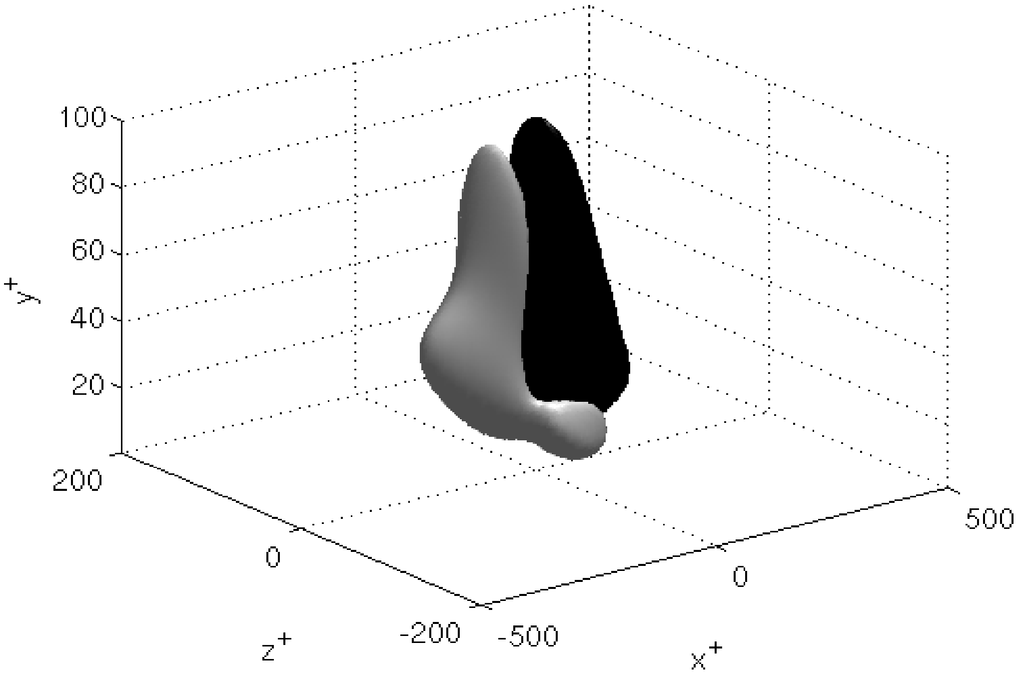

(a)

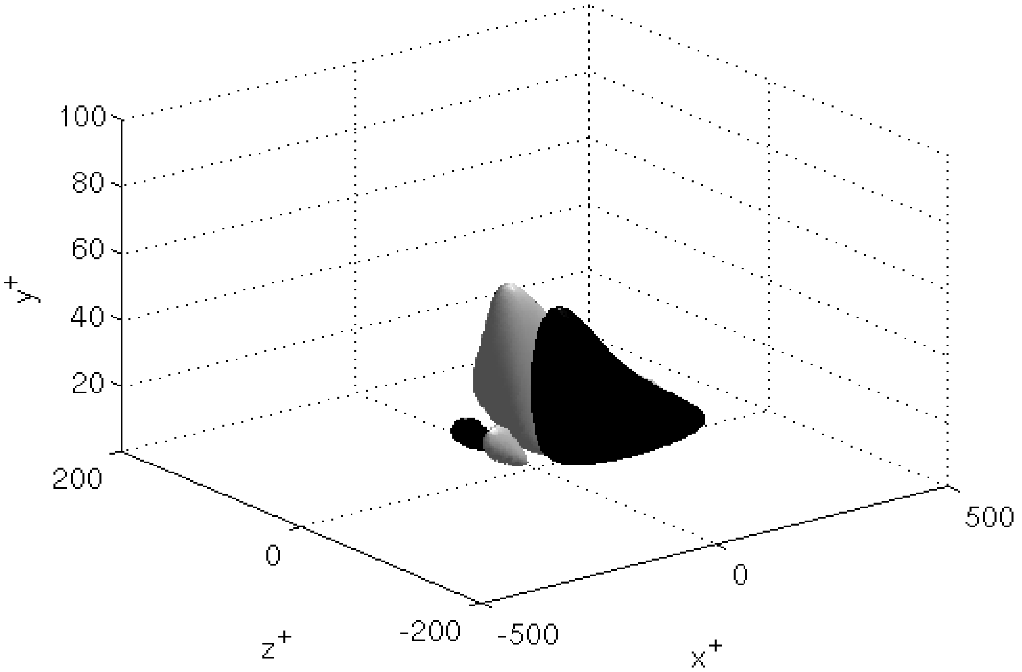

(b)

Figure 4.11: Surfaces at $\pm 25\,\%$ (light-dark gray,respectively) of the maximum for the state noise-measurement correlation, at zero time lag. Measurement is pressure fluctuation p; (a) v component; (b) η-component. Dependent variables x, y and z normalized with viscous units. Results at $Re_\tau = 100$, $x^+ \in [-500, 500]$, $z^+ \in [-200, 200]$.

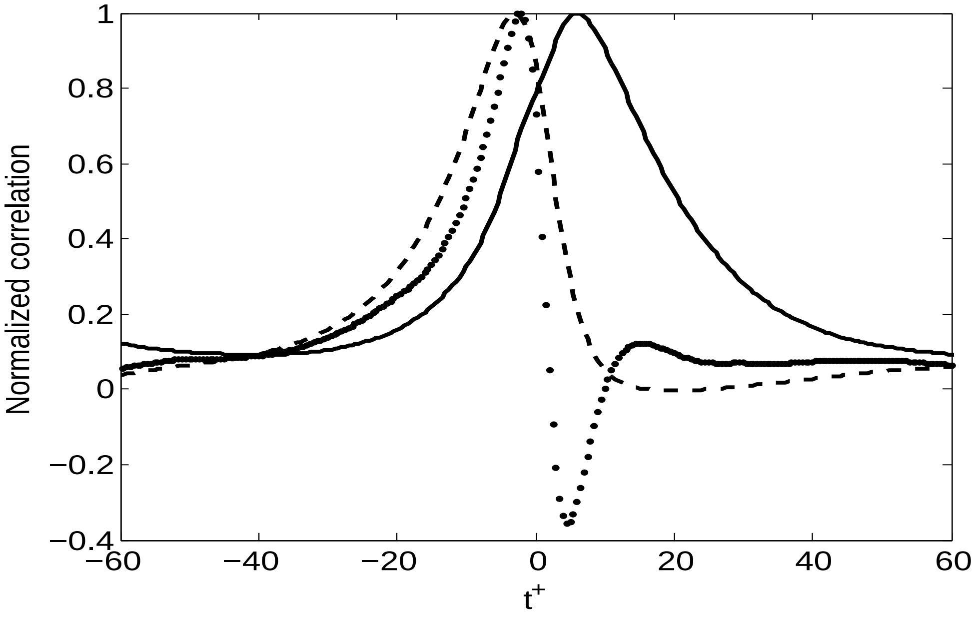

Figure 4.12: Time dependence of the normalized correlation between wall measurement and state noise at $y^+ = 10$, at zero separation in spanwise and streamwise directions. Dependent variable t normalized with viscous units. Solid line: correlation between τ_x and v; dashed line: correlation between τ_z and η; points: correlation between p and v. Results at $Re_\tau = 100$.

			τ_x		τ_z		p	
Re_τ	$\overline{\alpha}$	$\overline{\beta}$	Δt^+_{ker}	T^+_{ker}	Δt^+_{ker}	T^+_{ker}	Δt^+_{ker}	T^+_{ker}
100	20	40	0.5	12.5	0.5	12.5	0.5	37.5
180	12	54	0.75	18.75	0.5	18.75	0.75	56.25

Table 4.3: Parameters employed in the compensator design.

is computed runtime by direct application of the discretized form of the convolutional relation:

$$\hat{v}_{wall}(\alpha, \beta, t) = \int_0^t \hat{K}(\alpha, \beta, \tau)\hat{m}(\alpha, \beta, t - \tau)\, d\tau \qquad (4.15)$$

for each wavenumber pair. Here $\hat{m}(\alpha, \beta, t)$ denotes the history of the Fourier coefficients of a generic measurement, i.e. $\hat{\tau}_x$, $\hat{\tau}_z$ or $\hat{p}$, and $\hat{K}(\alpha, \beta, t)$ is the compensator impulse response function, parametrized with the wavenumber pair. Equation (4.15) is discretized with a time resolution Δt_{ker} and truncated at a finite length T_{ker}, corresponding to a truncation of the response function of the optimal kernel. Numerical values of all the parameters mentioned above are reported in table 4.3.

The spatial structure of representative compensator kernels, at zero time lag and for the measurements of τ_x, τ_z and p, are reported in fig. 4.13, 4.14 and 4.15, respectively. Kernels designed to use streamwise skin friction or pressure show a symmetry with respect to the $x - K$ plane, while kernels designed to use the spanwise skin friction component are antisymmetric. Note also that the compensator kernels are localized in physical space. This feature, also noted by other authors [49; 76], and predicted theoretically in [4] for the LQG framework, is useful as it indicates that the kernel requires wall information in the vicinity of the actuator only. Therefore, in a practical implementation, it may be sufficient to use a spatially truncated kernel in order to obtain sub-optimal compensators, without excessive degradation of the compensator performance. This procedure was successfully verified in [49] in control of transitional plane Poiseuille flow using state-feedback optimal controllers. As a final remark, note that some noise is present in the spatial structure of the kernels obtained with the present Wiener-Hopf procedure. This noise comes directly from the use of measured statistics of the flow in the design procedure, and eventually would disappear provided that the averaging time goes to infinity. Since the signal-to-noise ratio for the computed kernels is relatively high ($\approx O(10)$) we decide not to apply further spatial filtering to the present results.

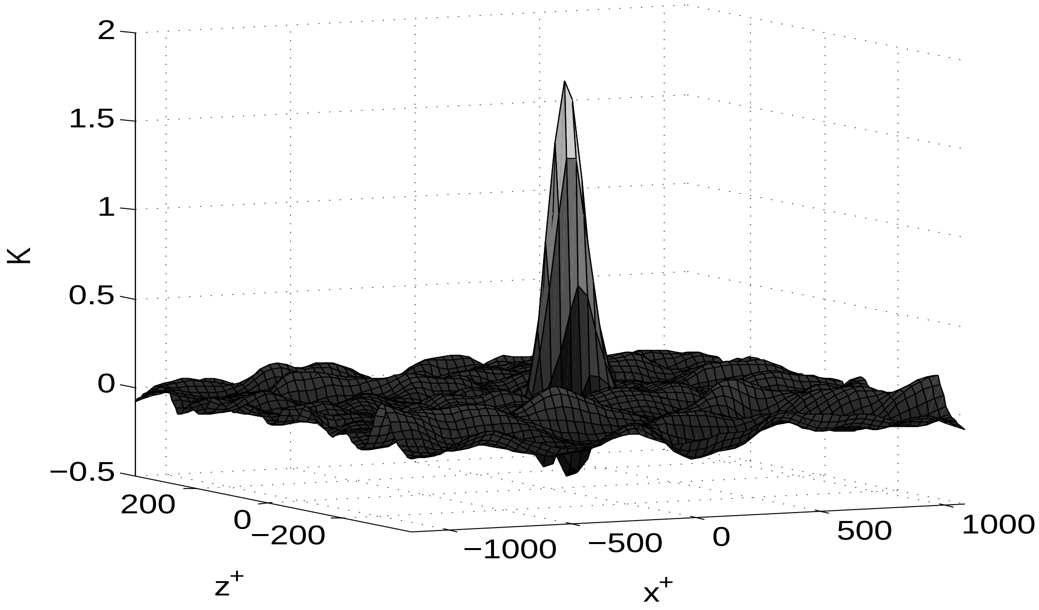

Figure 4.13: Spatial representation of the compensator kernel at zero time lag, $K(x, z, 0)$; measurement is the streamwise wall friction. Dependent variables x and z normalized with viscous units. Result at $Re_\tau = 180$; the full computational domain is represented.

4.4.2 Performance assessment

More than 300 direct numerical simulations of controlled turbulent channel flows have been performed, in order to assess the drag reducing capability of feedback compensators designed with different parameters; these simulations required

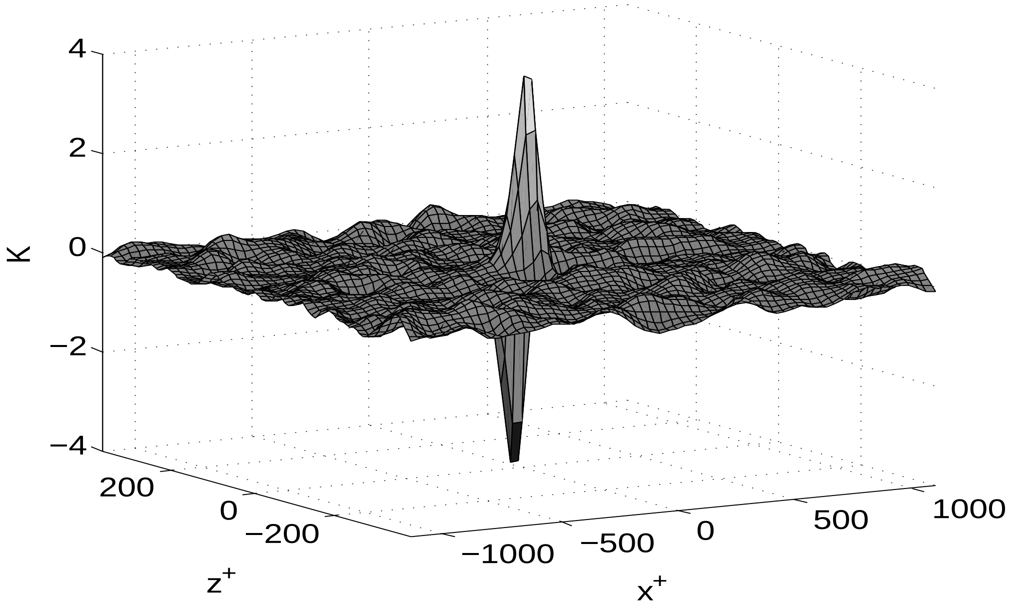

Figure 4.14: Spatial representation of the compensator kernel at zero time lag, $K(x, z, 0)$; measurement is the spanwise wall friction. Dependent variables x and z normalized with viscous units. Result at $Re_\tau = 180$; the full computational domain is represented.

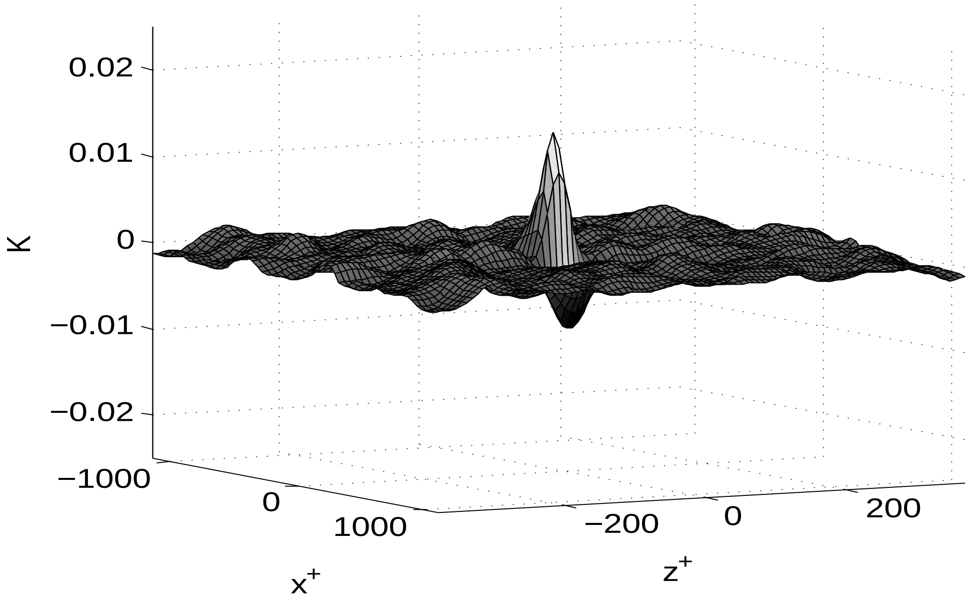

Figure 4.15: Spatial representation of the compensator kernel at zero time lag, $K(x, z, 0)$; measurement is the wall pressure fluctuation. Dependent variables x and z normalized with viscous units. Result at $Re_\tau = 180$; the full computational domain is represented.

	D-norm			E-norm		
Re_τ	τ_x	τ_z	p	τ_x	τ_z	p
100	2%	0%	0%	0%	0%	0%
180	8%	6%	0%	0%	0%	0%

Table 4.4: Best performance drag reduction results, as a function of Re, state weighting and measurement. Accuracy of the drag reduction is estimated to be $\approx \pm 1\%$. The values 0% indicate that no measurable difference in the average skin friction was obtained with respect to the uncontrolled case.

approximately 2 months of computational time on 64 AMD Opteron quad-core machines, available as part of a cluster dedicated to the simulation of wall turbulence at the University of Salerno. Simulations at a given Re are initialized with the same initial condition, corresponding to an instantaneous flowfield from a fully developed turbulent channel flow. Drag reduction results, averaged over at least 1500 viscous time units, are compactly reported in table 4.4.

A first noteworthy result from table 4.4 is that the unweighted energy norm is ineffective in providing drag reduction results. This fact is coherent with previous LQG-based results in literature, specifically with those of Lim [76], whose only reported drag reduction results at $Re_\tau = 100$ are obtained with weighting functions derived from the output equation in his state-space model; similar weighting was successfully used by Lee et al. [74], in a LQG-Loop Transfer Recovery formulation designed to reduce drag in $Re_\tau = 100$ turbulent channel flow. The present $Re_\tau = 180$ results strengthen the previous ones, indicating that the energy norm is not appropriate when using linear feedback control with wall-based linear estimators for turbulent drag reduction purposes.

Conversely, weighting functionals derived from the dissipation norm appear to be effective. This fact is reasonable, as dissipation norm is related to the mean skin friction in the uncontrolled case, as shown in Sec. 2.3.2. It is also interesting to note that the performance of such controllers improves as Reynolds number increases. This "inverse" Re-effect may be explained by the following argument. The zero-net mass flux control action targets directly the rate of dissipation pertaining to turbulent fluctuations; the modification of the average profile - along with the corresponding reduction in skin friction drag - is a secondary effect due to nonlinear interactions between fluctuations and the mean flow. In the uncontrolled case, the percentage contribution of the mean flow and flow fluctuations to the total rate of dissipation is reported in table 4.5. In this table, it is shown that the contribution of the flow fluctuations to the average dissipation rate *increases* with Re. Therefore, it is reasonable to expect that the dissipation norm may be more effective for control design purposes even at higher values of Re, up to a certain saturation limit; it is argued that this is the reason for the inverse effect on drag reduction reported in table 4.4.

Finally, from table 4.4 it appears that compensators using the pressure feedback measurement are not effective, with the two state weighting used. The estimator in

Re_τ	$\sum_{\alpha,\beta} D(\alpha,\beta)$	D_{mean}
100	26.8%	73.2%
180	39.5%	60.5%

Table 4.5: Contribution of flow fluctuations and mean flow to the total dissipation, as a function of Re; see Sec. 2.3.2.

the form of a Wiener filter is automatically embodied in the present compensator design procedure; in light of the estimation results in Chap. 3, this result is not surprising, and suggests that the pressure measurement alone is not sufficient in providing flow information to build an effective feedback control signal when using the present objective functionals.

4.4.3 Best performance results

Performance

The best performing kernel led to drag reduction up to $\approx 8\%$, using streamwise skin friction measurements; this value is estimated to be accurate within $\pm 1\%$. The optimal choice of "tuning" parameters corresponding to this best-performance kernel is $R = 0.04$ and $\phi_{dd} = 0.04$. The initial transient of the plane-averaged skin friction drag is reported in fig. 4.16; it is shown that the flow rapidly experiences drag reduction in the first 20 viscous time units, and then slowly moves towards a statistically stationary steady state. In steady conditions, a reduction of $\approx 7\%$ of the rate of dissipation of kinetic energy associated to flow fluctuations was measured.

The instantaneous power spent for the control action may be conservatively defined as [12]:

$$P_\phi = \int_A \Big(|v_{wall}| \frac{\rho \phi^2}{2} + |v_{wall}(p - \overline{p})| \Big) dA,$$

where A is the area where the control action is applied, ρ is the fluid density and $\overline{p}$ is the average wall pressure. The power reduction index (expressing the net power saved when applying the controller) is defined as:

$$P.R. = 100 \frac{P_r - P_c}{P_r},$$

where P_c is the sum of the time average of P_ϕ and the (reduced) power required to drive the flow against viscous stresses in the controlled flow, while P_r is the power required in the uncontrolled case to drive the flow against viscous stresses. P_ϕ was found to be $\approx 0.2\%$ of P_r; the associated power reduction index was found to be $P.R. \approx 7.7\%$.

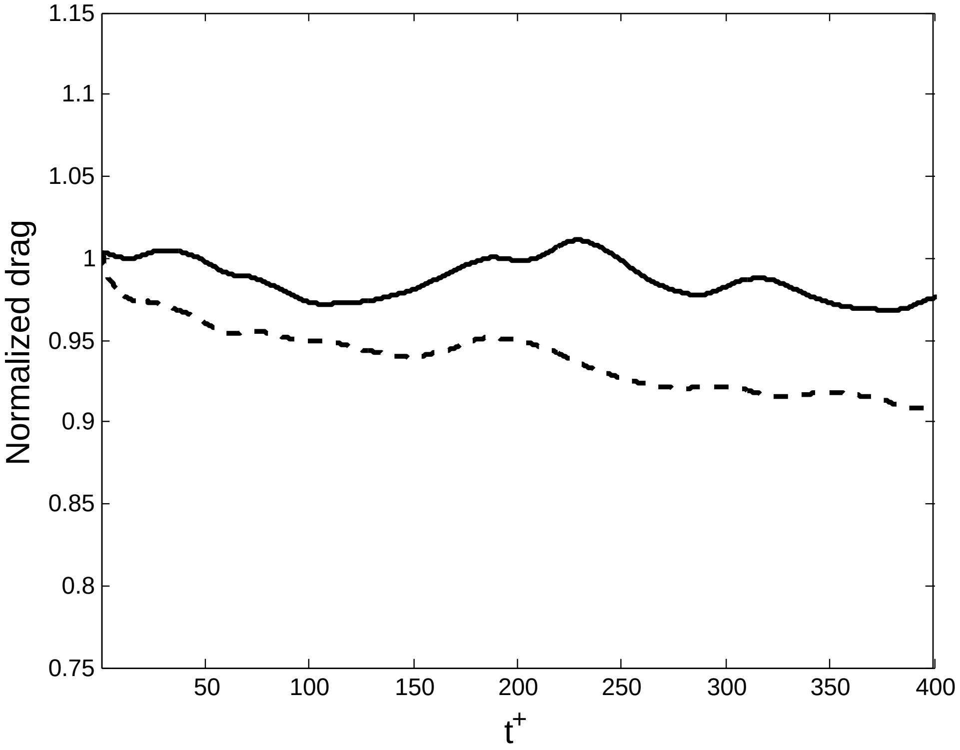

Figure 4.16: Temporal transient response of the normalized wall-averaged skin friction drag at the lower wall, against viscous time units; control action is initiated at $t^+ = 0$; uncontrolled (solid), controlled (dashed) flow.

ϕ_{dd}	0.08	0.04	0.02
$\%D.R.$	5%	8%	0%

Table 4.6: Effect of ϕ_{dd} on the drag reduction performance.

T^+_{ker}	18.75	15	11.25
$\%D.R.$	8%	8%	8%

Table 4.7: Effect of T_{ker} on the drag reduction performance.

Sensitivity with respect to to design parameters

We briefly present here the effect of small variations of tuning and design parameters presented in table 4.3. The only parameter which is not considered in the present study is the time resolution of the impulse response of the kernel, Δt_{ker}. This value is kept fixed in the whole design procedure, from the measurement of the average impulse response to the design of the kernel; however, in this $Re_\tau = 180$ case the time resolution is $\Delta t^+_{ker} = 0.75$, which corresponds to about three-four times the typical time step size to perform well-resolved DNS at comparable Reynolds number. This choice was considered a good compromise between the time resolution requirements and the associated dimensions of the various databases used in the kernel design procedure.

The single variation of the control weight, keeping all the other parameters fixed, does not significantly affect the drag reduction performance, which is nearly equal to $\approx 8\%$ for $R \in [0.005, 0.08]$. On the other hand, table 4.6 shows the effect of a small variation of the noise disturbance intensity ϕ_{dd} on the drag reduction performance; it is shown that a lower limit for ϕ_{dd} exists, below which the performance is degraded. Reduction of the time extension of the kernel does not affect the drag reduction performance; in fact, results shown in table 4.7, highlight that a reduction of 40% of T_{ker} does not cause a measurable degradation of the kernel's performance, thus indicating that the time window length was chosen conservatively. Finally, effects of the reduction of the limit wavenumbers for the actuation are shown in table 4.8; it is shown that it is necessary to reduce by 50% the wavenumbers interested by the actuation in both directions in order to obtain a performance degradation to 6%. This confirms that the wavenumber array used in the present investigation was chosen conservatively.

	$(\overline{\alpha}, \overline{\beta})$	$(0.75\overline{\alpha}, 0.75\overline{\beta})$	$(0.5\overline{\alpha}, 0.5\overline{\beta})$
$\%D.R.$	8%	8%	6%

Table 4.8: Effect of wavenumber truncation on the drag reduction performance.

Statistics of the controlled flow

Statistics of the controlled flow are computed using an ensemble of 10 velocity fields, saved over a time window of 1500 viscous time units after the initial transient. In the presentation of the results, note that the plus superscript indicates variables made nondimensional with the *actual* friction velocity, e.g. in the controlled case the friction velocity of the controlled flow is used.

Fig. 4.17 compares the mean velocity profiles, represented in the law-of-the-wall form, of the uncontrolled and controlled flow. It is shown that the controlled flow exhibits a logarithmic layer, having nearly the same slope of that in the reference case, and shifted upward; this is a common feature of a variety of wall flows in drag reducing conditions [26; 74].

Fig. 4.18 to 4.20 show the wall-normal behavior of the diagonal components of the Reynolds stress tensor, while fig. 4.21 compares the term $-\langle uv \rangle$ for the uncontrolled and controlled flow. The control action, in general, reduces the fluctuation intensity, in particular in the near-wall region; a notable exception is the spanwise fluctuation intensity $\langle ww \rangle$, which appears not to be evidently affected by the control. Furthermore, note that - owing to the non-homogeneous boundary condition on the wall-normal velocity component - the fluctuation intensity $\langle vv \rangle$ is non-zero at the wall (fig. 4.19). The only nonzero off-diagonal component of the Reynolds stress tensor is mildly reduced in the controlled case over the whole channel half-width. This effect corresponds to a reduction in the production of turbulent kinetic energy, especially in the buffer layer where peaks are evident for both the uncontrolled and controlled case in fig. 4.24.

It is interesting to compare the anisotropy pattern of the controlled and uncontrolled flow. The level of anisotropy can be quantified by introducing the normalized anisotropy tensor [84]

$$a_{ij} = \frac{\langle u_i u_j \rangle}{\langle u_k u_k \rangle} - \frac{1}{3}\delta_{ij}.$$

Note that this tensor, by definition, has zero trace. Therefore, it is uniquely characterized by its second and third invariants, II_a and III_a, that may be computed to produce anisotropy invariant maps (also known as “Lumley triangles”). These maps are shown in fig. 4.22 and 4.23. Each point in the map corresponds to a given location in wall-normal direction; thin black curves define the area in the $III_a - II_a$ plane corresponding to the states of physically realizable turbulence. In particular, the upper straight line corresponds to flow states characterized by two-component turbulence, while the left and right curve lines correspond to axisymmetric turbulence strained by compression or expansion, respectively. Fig. 4.22 shows the usual anisotropy pattern for a turbulent channel flow, where the flow state moves from a two-component state (in the near wall region up to $y^+ \approx 10$) towards a state characterized by turbulence strained by axisymmetric expansion. In the controlled case, the flow anisotropy moves from a pure one-component state at the wall (due to the control action) to an intermediate state far from the two-component state in the

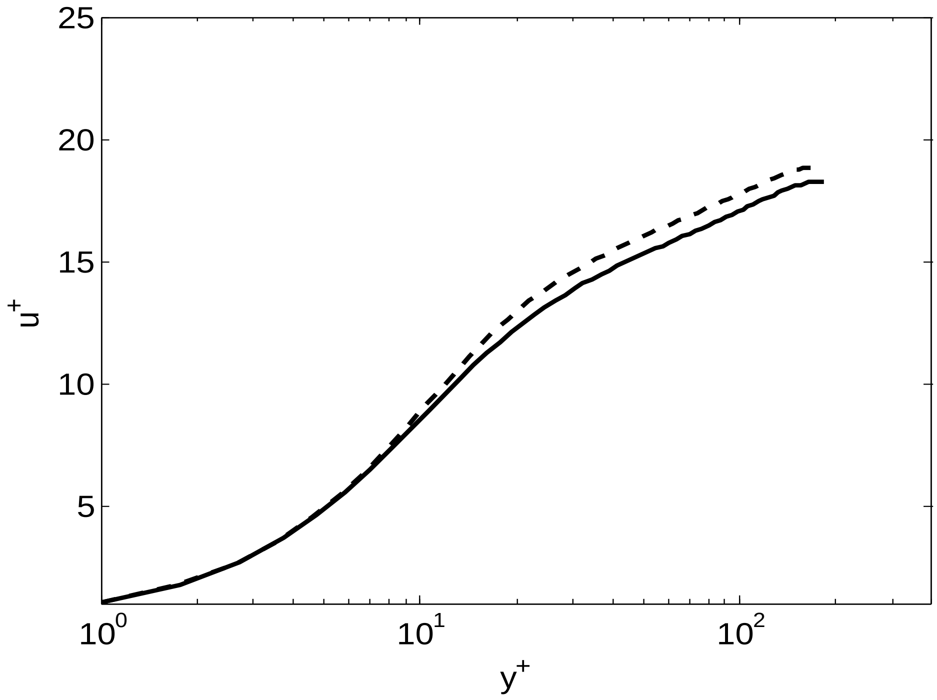

Figure 4.17: Mean velocity profile in the law-of-the-wall form; uncontrolled (solid) and controlled (dashed).

viscous sublayer, to eventually move towards the same pattern of the uncontrolled case in the center of the channel. It has been recently noted by Frohnapfel et al. in [37] that a common feature of turbulent flows experiencing high drag reduction (typically, as an effect of polymer injection) is the tendency of the near-wall flow fluctuations towards a one-component state in the mean flow direction, and a consequent tendency of the fluctuations far away from the wall to move towards the right boundary of the Lumley triangle. We note here that, when wall actuation is performed with wall blowing/suction with the wall-normal velocity component, this condition is not satisfied, as shown in fig. 4.23; this is due to the fact that the controlled flow will not experience a two-component condition in the near wall region, and therefore the anisotropy pattern is dramatically changed.

4.5 Conclusions

In this chapter, a linear model of the turbulent channel flow – in the form of the average impulse response to wall forcing – has been used in the design of optimal compensators aimed at skin friction drag reduction. A special formulation of the optimal compensator problem in frequency domain has been employed; this formulation is particularly attractive in the present very high-dimensional setting, where it reduces the compensator design procedure to solving a sole scalar Wiener-

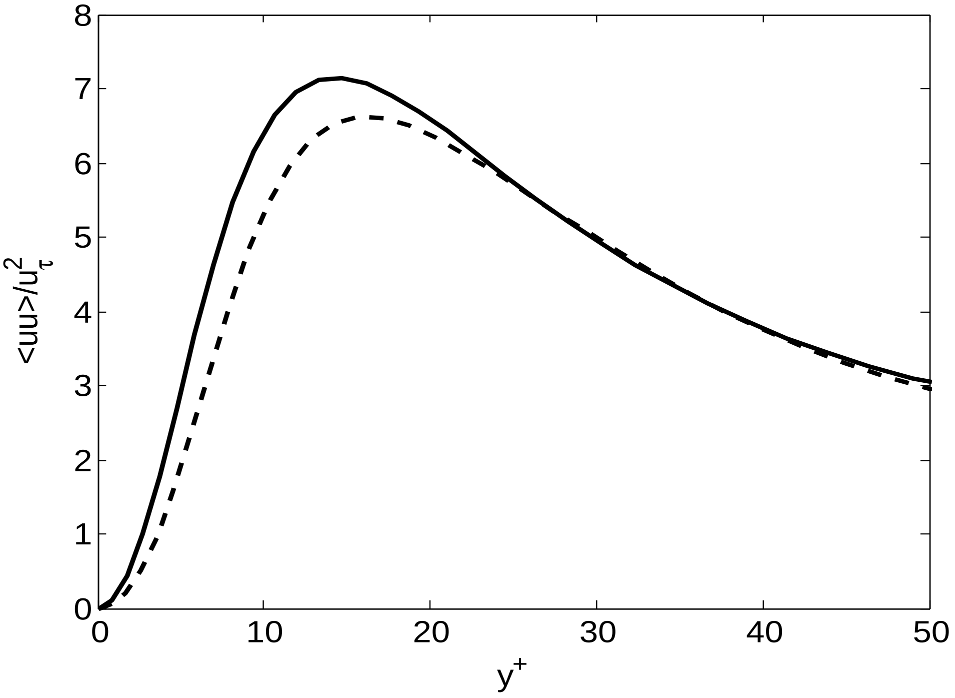

Figure 4.18: Reynolds stresses $\langle uu \rangle^+$. Comparison of the uncontrolled (solid) and controlled (dashed) flow.

Hopf equation. Furthermore, the compensator frequency response is designed in one single step, without the need to resort to the separation theorem.

The designed compensators have been tested at two different values of Re, using two different weighting functions and either one of all the possible wall measurements. It has been confirmed, even at the higher value of Re, that objective functionals built on the energy norm of the flow fluctuations do not yield effective compensators. On the other hand, objective functionals built from the dissipation norm have been found to be effective, and in particular more effective at $Re_\tau = 180$ than at $Re_\tau = 100$. Compensators using the measurement of wall pressure alone were found uncapable of reducing drag.

Overall, the performance of compensators described in the present chapter is poor. Well designed passive control devices (e.g. riblets) offer comparable performance but do not need feedback. However, considering that the estimator embodied in the present compensator is in fact a Wiener filter accounting for the full time-space structure of the state noise, and in light of the results of Chap. 3, it can be deduced that the limited performance can be attributed to the choice of the cost functions. Although objective functionals based on the dissipation norm may provide better performances at even higher Re, larger drag reductions were obtained by other authors in the LQG setting by using particular state weighting matrices derived from the output relations.

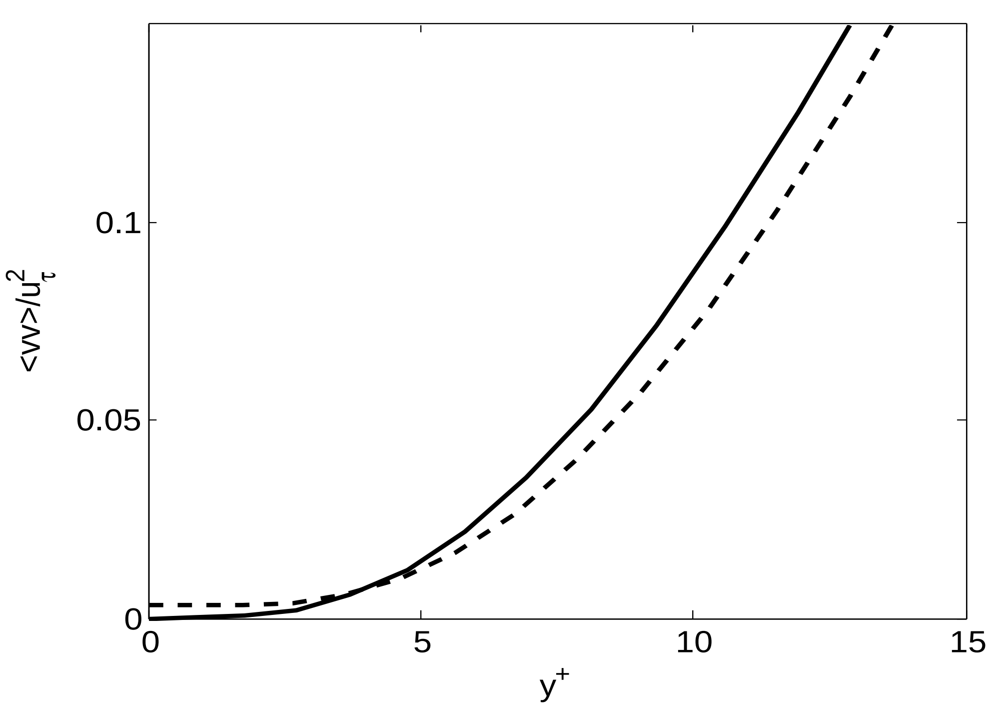

Figure 4.19: Reynolds stresses $\langle vv \rangle^+$. Comparison of the uncontrolled (solid) and controlled (dashed) flow.

However, the design methodology presented in this chapter has proved to be very effective and computationally efficient, if compared to standard Riccati-based techniques. Therefore, it may be exploited in the future to ease the compensator design procedure, thus allowing a wide parametric study on a broader variety of objective functionals. Furthermore, the present frequency-domain formulation may be applied to different flow control problems (e.g. subcritical transition control) whenever dealing with very high dimensional systems with a limited number of actuators and sensors.

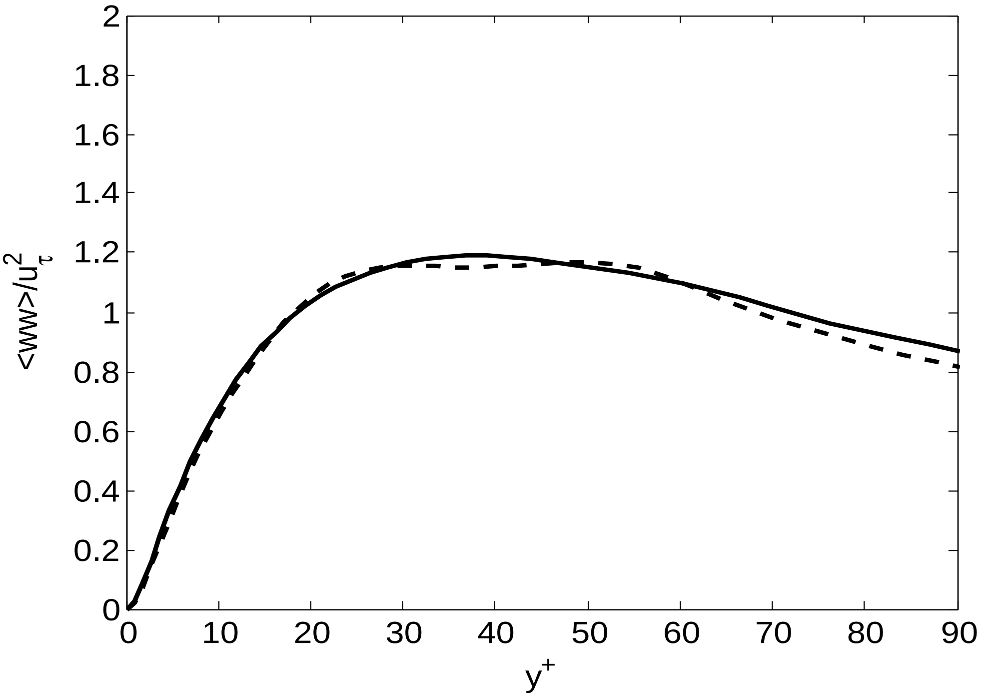

Figure 4.20: Reynolds stresses $\langle ww\rangle^+$. Comparison of the uncontrolled (solid) and controlled (dashed) flow.

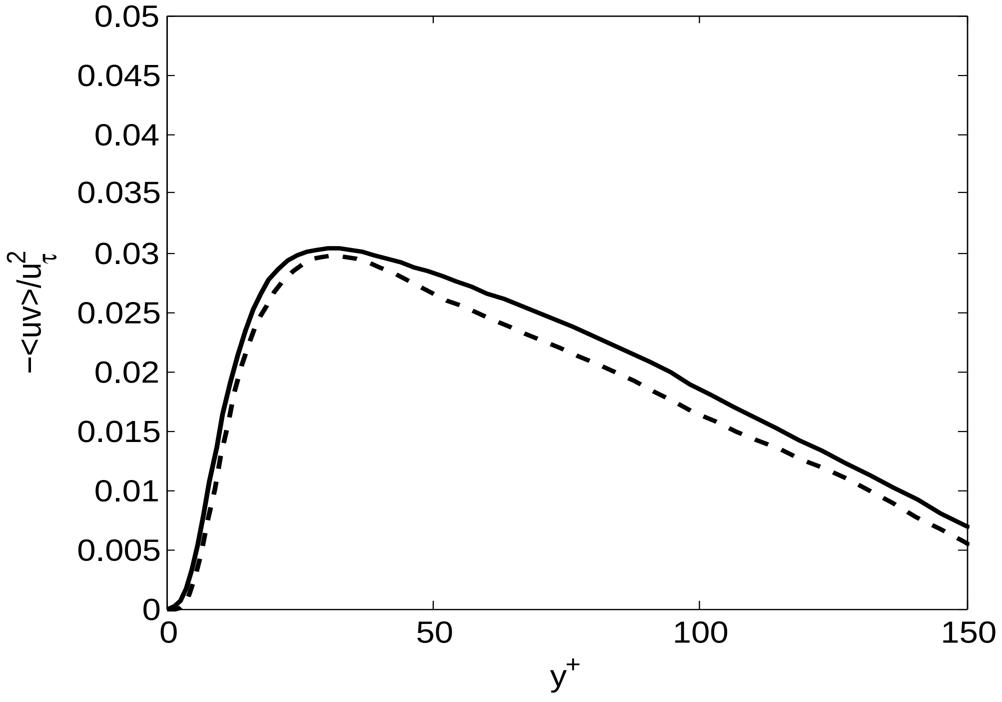

Figure 4.21: Reynolds stresses $\langle uv\rangle^+$. Comparison of the uncontrolled (solid) and controlled (dashed) flow.

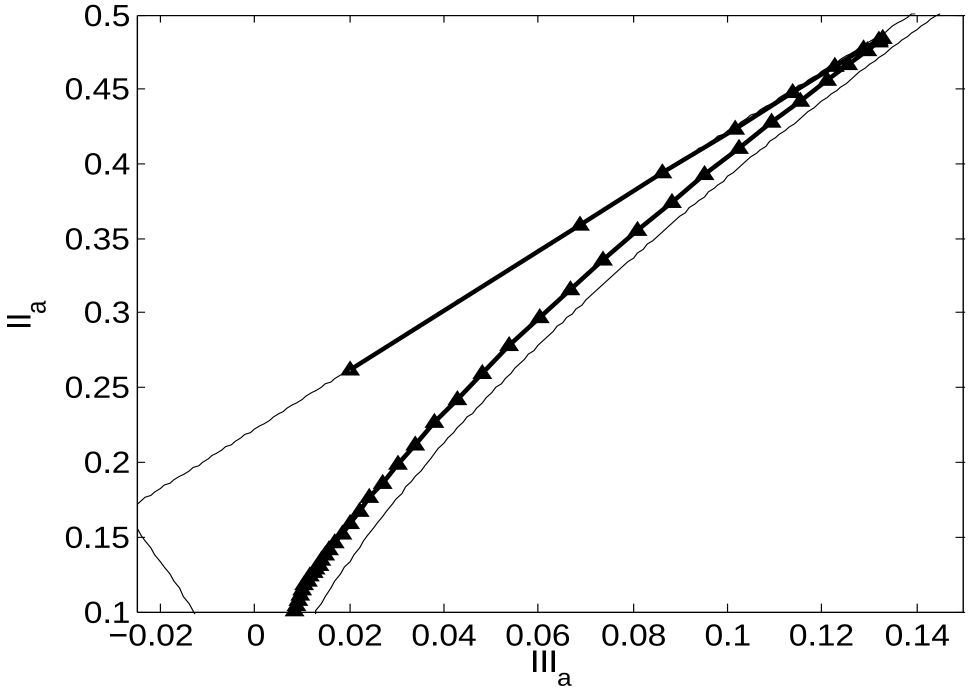

Figure 4.22: Reynolds stresses $\langle vv \rangle^+$. Top: comparison of the uncontrolled (solid) and controlled (dashed) flow.

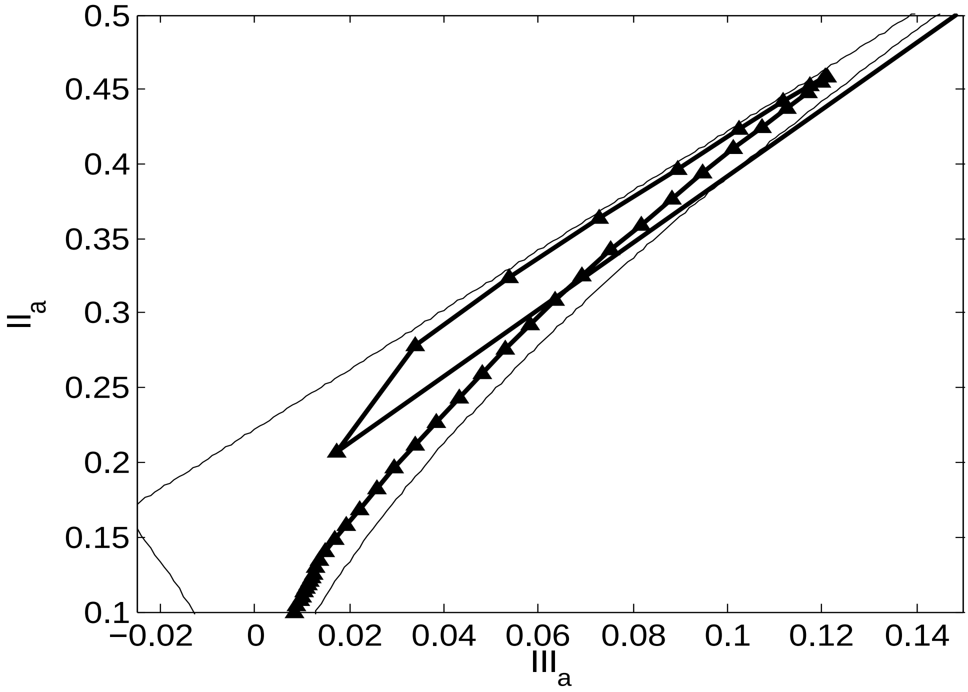

Figure 4.23: Reynolds stresses $\langle vv \rangle^+$. Top: comparison of the uncontrolled (solid) and controlled (dashed) flow.

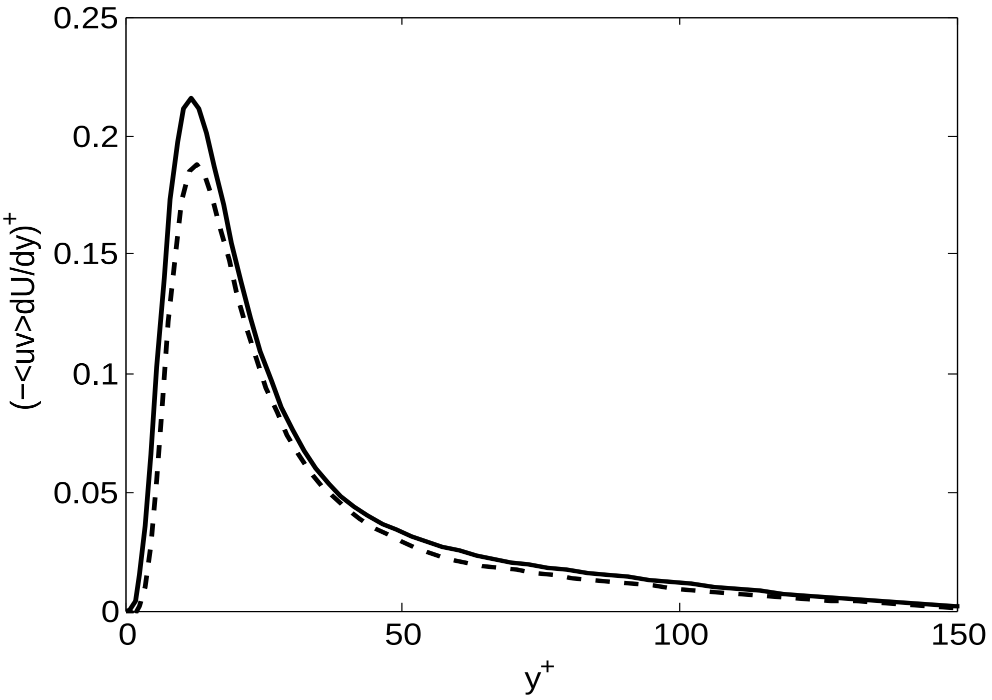

Figure 4.24: Production of turbulent kinetic energy. Comparison of the uncontrolled (solid) and controlled (dashed) flow.

Chapter 5

Conclusions and future developments

The present work has considered the problem of the optimal estimation and control of wall turbulence. After a discussion of the state-of-the-art results, key issues have been outlined and addressed throughout the thesis.

A first open question is the optimal linear *estimation*, that has been recently addressed in the framework of Kalman filtering theory [24]. Results presented in that work were based on the central assumption of whiteness of the state noise acting on the linearized equations, thus resulting in a truncation of the time-structure of the state noise autocorrelation. It was natural to ask whether the poor linear estimation performance described in [24] is due to the noise structure truncation, or to the use of a linear dynamical system as a state estimator. Results obtained in this thesis suggest the reason to be the latter. In fact, it has been shown that Wiener filters, specifically designed with an efficient frequency-domain approach to account for the full time-space structure of the state noise, did not outperform significantly standard Kalman filters. Thus, it seems reasonable to blame the linearity assumption for their rather poor performance. Indeed, linear dynamics of the state estimators is decoupled in wavenumber space, and the nonlinear triadic interactions among different wavenumbers are therefore completely missed; apparently, knowledge of the time structure of the state noise is not sufficient to compensate for this effect. Note also that this observation is in agreement with the findings presented in [24] when using extended (nonlinear) Kalman filters. These estimators were designed with a standard Riccati procedure, and then *ad-hoc* modified by reintroducing the nonlinearity of the original equations. Such nonlinear estimators outperformed linear Kalman filters, but at the additional cost of a DNS to provide the state estimate. Such nonlinear estimators, unless their order is not reduced appropriately, are clearly not feasible in applications.

On the other hand, it was shown by initial attempts [50], and at substantially higher values or Re in App. A of this thesis, that LQR controllers – requiring full-state information – perform relatively well in friction reducing drag with a net energy saving, provided that an appropriate objective functional is selected in the design procedure. Hence, a possible route towards improving the performance of feedback compensators for turbulent drag reduction would be the optimization of static state-feedback controllers, and the design of nonlinear (possibly reduced-order) estimators for the flow state.

From the point of view of the design and test of optimal *compensators*, several issues have been addressed in this thesis. The recently proposed average linear response of the turbulent channel flow to wall forcing has been employed as a model for the forced flow system. This model has the feature of being *measured* directly from a DNS of turbulent channel flow or, at least in principle, from a laboratory experiment (see, for instance, the work by Hussain and Reynolds [52; 53; 112]). This model, given in the form of impulse response function, would require a state-space realization prior to applying standard Riccati-based techniques for the controller and estimator design. In order to avoid this procedure, which would be impractical considering the dimensions of the problem, a novel formulation of the optimal compensator design problem was employed. This formulation, first proposed by Luchini [79], is based on a frequency-domain approach; it represents the dual formulation in frequency domain of the optimal compensator problem for asymptotically stable systems, and offers several advantages. First, it allows designing an optimal compensator in a sole step, through the solution of a certain Wiener-Hopf problem, without the need to resort to the separation theorem. Secondly, the Wiener-Hopf equation to be solved is a scalar equation when the system is single-input/single-output, no matter the dimensions of the state; in this case, solving the compensator design problem is computationally far more efficient than the solution of two high-dimensional Riccati equations. Moreover, note also that, in the present control setting, the Wiener-Hopf problem is always well-posed provided that the weight on the control and the measurement disturbance intensity are nonzero. The present frequency-domain approach effectively avoids the need of handling systems having large dimensions of the state, thus answering one of the important issues raised in the recent review by Kim & Bewley [65]. Since it is built in the frequency domain, the present procedure allows for the design of LTI compensators only; however, this is not considered a limitation, as LTI compensators are easier to implement in practice (even with analog circuitry). Finally, the present formulation accounts for the temporal structure of the noise on the state, when this is important; moreover, dynamics of the measurement sensors may be easily accounted for by substituting their frequency response function in the appropriate coefficients of the Wiener-Hopf equation, without increasing the dimensionality of the problem.

The performance of single-input/single-output optimal compensators has been thoroughly verified by testing different weighting functions, as well as measurements of wall friction and pressure, for different values of the Reynolds number. In agreement with the results previously reported in literature, it has been shown that the unweighted energy norm is not a good choice for the construction of an objective functional that yields drag reduction. Conversely, a functional based on the rate of dissipation of fluctuations energy has been proposed, and shown to be increasingly more effective with increasing Reynolds number. Finally, it was shown that, with this choice of objective functional, only compensators working with measurements of wall friction components led to drag reduction.

In general, performance obtained in the present work in terms of drag reduction is rather poor. In light of the results of the Wiener filter, this fact may not be attributed to the estimation capabilities of the present compensators, as compared to Kalman filters developed by other researchers in previous work. Moreover, the use of an improved model of the flow system, based on measured average dynamics of the flow in response to wall actuation, did not provide substantial improvement. It is therefore natural to attribute this poor drag reduction performance to the objective functionals employed in this work. Most of recent results that obtained significant drag reductions [76] are based on objective functionals derived from quadratic forms of the measured variables; other kinds of objective functionals, different from the norms employed in this work, have been suggested in [65]. Therefore, a possible extension of the present thesis is to leverage the computational effectiveness of the Wiener-Hopf approach to test a large number of cost functions. Furthermore, the dissipation-based functional presented here should be used at higher Re, in order to establish to what extent compensators effectiveness increases with Re.

Most of the drag reduction results presented in the literature used wall actuation and wall-normal transpiration as a natural choice. However, assuming that the interpretation proposed in [37] is valid, the anisotropy patterns shown in Chap. 4 suggest that a condition of high drag reduction will never be attained when the wall-normal velocity is used as the control input. Therefore, we suggest here that a possible route to increasing the performance of feedback compensators may be that of changing actuation component, for instance employing active feedback with a wall distribution of spanwise velocity. Although spanwise forcing may be difficult to implement, in partial support of this statement we note that substantial drag reductions have been obtained with spanwise forcing when using feedforward control strategies, such as spanwise wall oscillations [104] or streamwise-traveling waves of spanwise velocity at the wall [101; 106].

The work presented in this thesis may be further extended in several directions. The Wiener filtering approach to state estimation can be naturally augmented by using multiple measurements of both skin friction components and pressure. In this case, the resulting Wiener-Hopf equation for the filter frequency response will have a matrix multiplicative coefficient and, therefore, will have to be necessarily solved in time domain; this procedure is entirely feasible, provided that efficient algorithms for the Cholesky factorization of the resulting block-Toeplitz matrix are available. In an analogous fashion, the optimal compensator design can be extended to the multiple input-multiple output case; again, this extension leads to a Wiener-Hopf problem with matrix coefficients, and the corresponding spectral factorization should be performed via a time-domain algorithm. A further extension of the present approach is the use of a robust control design technique in the IMC framework. Finally, the optimal compensator design technique presented in this thesis can be employed, in general, whenever a linear control problem has to be solved, given noise statistics and a linear model of the system; an example situation may be when intermediate linear control problems have to be solved in a nonlinear optimization procedure.

Though most of the results obtained in the present work do not appear encouraging at first sight, feedback control of wall turbulence is on the very edge of research in flow control, and much more efforts are needed to devise successful control and estimation strategies. In the framework of linear control theory, it is our hope that the present work will help developing viable design techniques for general flow control applications, while suggesting possible routes to be explored in future research on control of wall turbulence.

Appendix A

LQR-control of wall turbulence: flow statistics and Re-effects on drag reduction

We study via DNS the performance of Linear Quadratic Regulators (LQR) designed to reduce turbulent friction drag in a plane channel flow. Actuation is performed via wall blowing/suction with zero net mass flux. We report the first simulations of controlled flow at moderate Reynolds numbers, and establish that the amount of drag reduction decreases with Re. The controlled flow is given a statistical description, that enables us to discuss similarities between LQR control and opposition control.

Introduction

The reduction of turbulent skin friction drag is particularly appealing in many industrial applications – such as those in aeronautics and naval industry – where a slight improvement of the hydro- or aerodynamic efficiency of vehicles has the potential of greatly reducing the operating costs. Passive and active feed-forward control techniques for drag reduction have been developed in the past, and have met with various degree of success [40]. Recently, active feedback control techniques have been considered; owing to their feedback nature, such techniques have the potential for yielding significant performance with limited control effort. Most of the recent attempts to feedback-control a turbulent wall flow have addressed simple flows in elementary geometries, such as the plane channel flow, and have explored via Direct Numerical Simulation (DNS) different control approaches. Features of MEMS-based actuators, to be used in prospective applications, most naturally suggest distributed wall blowing/suction with zero net mass flux as the actuation technique of choice.

Choi et al. [26] introduced more than ten years ago a control strategy that uses such actuation, and that is today referred to as opposition control: at each time instant and at each wall position, the wall-normal velocity component is set as opposite to the one measured at some distance above. Provided this distance is properly chosen, this technique has been shown to yield as much as 25% drag reduction, with a net energy saving. Drag reduction was shown to occur [26] through the weakening the near-wall streamwise vortical structures, since the wall forcing counteracts their induced velocity field. Opposition control has since then been considered by other authors [45; 109], and in particular Iwamoto et al. [55] addressed the effect of changing Reynolds number on the performance of opposition control, finding a limited performance penalty when Re_τ (based on friction velocity and half the channel width) is increased from 100 to 650.

Leveraging modern control theory is a more recent approach, that does not rely on physical intuition: it simply requires a linear model of the system to be available, and a proper objective function. Bewley et al. [12] and Högberg et al. [49; 50] applied optimal control theory to the design of full-order LQR controllers for transitional and low-Reynolds number turbulent channel flow. They used the same kind of wall forcing, i.e. distributed blowing/suction, and obtained encouraging results. Drag reduction results have been reported also by Cortelezzi & Speyer [31] and Lee et al. [74]; these authors focused on the design of reduced-order compensators, to help handling the huge computational cost of the compensator design procedure.

There is thus an active research line devoted to designing model-based controllers for turbulent drag reduction through wall-based actuation. To date, however, a statistical characterization of the LQR-controlled flow is still missing. Indeed, reports of control theoretic approaches mainly focused on the design procedure of the controller itself, and the closed-loop system made by the turbulent flow plus its controller was considered as a black box, looked at through the chosen objective function and the corresponding performance in terms of drag reduction. It is a first aim of the present paper to provide some additional physical insight as to how a LQR controller affects the turbulent flow; in particular, we will discuss the degree of similarity to the opposition control in terms of flow statistics and drag reduction mechanism. A second, and not totally unrelated aim is to discuss how drag reduction performance depend on the value of the Reynolds number. Indeed available data for LQR control concern low values of Re only, owing to the huge computational costs involved, and the highest simulated Reynolds number in the context of turbulent plane channel flow is $Re_\tau = 100$. While inner scaling could be advocated to suggest that positive performances extrapolate to higher Re, a careful scrutiny of this aspect is essential to motivate further efforts and developments in this area, and to assess how far the LQR control of turbulent wall flows can actually reach.

The structure of the paper is as follows. In §A a brief description of the flow and the related control problem will be given, as well as a discussion of the control parameters. Section §A focuses on the initial response of the system to the control action. Sections §A and §A are devoted to the analysis and discussion of the statistics of the controlled turbulent channel flow, and to a performance assessment. Section §A discusses the drag reduction mechanism, and a concluding discussion is given in §A.

Problem formulation

We shall consider the incompressible flow in an indefinite plane channel, with control at the walls made by a distribution of wall blowing/suction with zero net mass flux. The flow is simulated via DNS in a bi-periodic computational box with size $[0, L_1] \times [0, 2\delta] \times [0, L_3]$ in the streamwise (x_1), wall-normal (x_2) and spanwise (x_3) directions, respectively. The corresponding velocity components are denoted by u, v and w. When convenient, the x_2 direction will be denoted with y.

The design procedure for the controller follows closely the one proposed by Högberg et al.[49], to which the reader is referred for details. The governing incompressible Navier-Stokes equations are linearized around the laminar Poiseuille solution $U(x_2)$ and rewritten in the well-known v-η formulation, where η denotes the wall-normal vorticity component. Fourier transforming the v and η equations in the homogeneous directions x_1 and x_3 yields:

$$\begin{aligned} \Delta\dot{\hat{v}} &= [-i\alpha U\Delta + i\alpha U'' + \Delta\Delta/Re]\hat{v} = \mathbf{L}\hat{v} \\ \dot{\hat{\eta}} &= [-i\beta U']\hat{v} + [-i\alpha U + \Delta/Re]\hat{\eta} = \mathbf{C}\hat{v} + \mathbf{S}\hat{\eta} \end{aligned} \tag{A.1}$$

which corresponds to a transformation into the Orr-Sommerfeld-Squire form. Here α and β denote the wavenumber in x_1 and x_3 directions, respectively, and $\Delta = \partial^2/\partial x_2^2 - \alpha^2 - \beta^2$; variables with the hat are Fourier coefficients, the dot denotes time differentiation, and the Reynolds number Re is defined with the bulk velocity U_b and the channel half-width δ.

The system (A.1) is then recast in state-space form with a lifting procedure[49]. The differential system

$$\dot{x} = Ax + B\dot{\phi} \tag{A.2}$$

is obtained, where x is the state and the control input $\dot{\phi}$ is the time-derivative of the wall blowing/suction velocity at the channel walls.

Controllers are designed by applying optimal control theory to this system. In particular, the problem is stated as the search for a proportional (in Fourier space) controller K such that the control law $\dot{\phi} = Kx$ minimizes a suitable quadratic cost functional, as the following:

$$J = \int_0^{+\infty} (x^H Q x + \dot{\phi}^H R \dot{\phi})\, dt, \tag{A.3}$$

where the hermitian positive semidefinite matrix Q and the hermitian positive definite matrix R are design parameters. The optimal control problem is thus reduced to the minimization of the functional J, constrained by the state-space equation (A.2). It can be shown [36] that the optimal feedback gain matrix K can be found by

$$K = -R^{-1}B^H Z,$$

where Z is the so-called stabilizing solution to the following algebraic Riccati equation:

$$ZA + A^H Z - ZBR^{-1}B^H Z + Q = 0. \tag{A.4}$$

The optimal control problem is completely defined by the system dynamics (matrix A), the actuation technique (matrix B), and the state and input weighting matrices Q and R. In order to obtain a linear representation which is, in some sense, closer to the real flow system, the mean flow profile of the uncontrolled turbulent flow is used in the definition of A. The importance of using the actual mean flow profile has been highlighted by Högberg et al.[50], where a controller scheduled on a set of velocity profiles between the laminar and mean turbulent one led to relaminarization of $Re_\tau = 100$ turbulent channel flow. The dependence of the control performance on the choice of the cost functional has been discussed in previous work[12] suggesting that, in the present infinite-horizon setting, it is senseful to employ an objective function derived from the kinetic energy of the flow perturbations, in the following weighted form:

$$\mathbf{E}(\alpha, \beta) = \frac{1}{8k^2} \int_{-1}^{1} w(x_2) \Big(k^2 |\hat{v}|^2 + |\frac{\partial \hat{v}}{\partial x_2}|^2 + |\hat{\eta}|^2 \Big) \, dx_2$$

The function $w(x_2)$ is an arbitrary weighting function that can be used as a tailoring parameter in the controller design process. Kim & Lim[66] suggested that a control system targeting the linear coupling term $\mathbf{C} = -i\beta U'$ in the Orr-Sommerfeld-Squire equations would be effective in suppressing the self-sustained cycle of wall turbulence. Following Högberg et al.[50], we choose a weighting function of the form $w(x_2) = 1 + U'(x_2)^2$ to target indirectly the coupling term $\mathbf{C}$, with the additional advantage of having an increased weight on near-wall states, more prone to be affected by wall-based control. The selection of the control weighting matrix R is a practical matter, that in the design of real control systems involves accounting for technical specifications of the actuators. In the present idealized setting, we use a matrix $R = \rho I$, I being the identity matrix, and $\rho = 0.01$. This value allowed us to keep the maximum magnitude of the wall blowing/suction velocity below the reasonable limit of 15% of the bulk velocity, for the considered values of Re.

The solution to the optimal control problem described above involves solving equation (A.4) for each wavenumber pair (α, β): thanks to decoupling in Fourier space, the entire control problem requires the solution of a large number of one-dimensional problems. Controllers are reconstructed for the full velocity and vorticity fields v and η. Fourier transforming back to physical space yields the so-called

case	Re	Re_τ	N_1	N_2	N_3	Δx_1^+	$\Delta x_{2,m}^+$	Δx_3^+	Δt^+
L	1450	100	128	64	128	9.8	5.4	4.9	0.31
M	3333	200	256	128	256	9.8	5.4	4.9	0.29
H	6882	400	512	256	512	9.8	5.4	4.9	0.19

Table A.1: Parameters of the spatial and temporal discretization (quantities with $+$ superscript are made nondimensional with inner variables of the uncontrolled flow); $\Delta x_{2,m}$ is the maximum grid spacing in the wall-normal direction.

control convolution kernels; these two kernels $\mathbf{K}_v$ and $\mathbf{K}_\eta$ relate the control signal $\dot{\phi}(x,z,t)$ at a given time to the v and η fields in the whole domain via the following convolution integrals:

$$\begin{aligned}\dot{\phi}(x,z,t) = &\int \mathbf{K}_v(x-\overline{x},\overline{y},z-\overline{z})v(\overline{x},\overline{y},\overline{z},t)\ d\overline{x}d\overline{y}d\overline{z}\\ &+\int \mathbf{K}_\eta(x-\overline{x},\overline{y},z-\overline{z})\eta(\overline{x},\overline{y},\overline{z},t)\ d\overline{x}d\overline{y}d\overline{z}.\end{aligned} \tag{A.5}$$

Computing the control kernels requires the efficient solution of a large number of algebraic Riccati equations (A.4), one for each wavenumber pair. These equations are solved using the Schur method [32]; the flop count of this method can be estimated to be $O(N^3)$, where N is the number of states. The overall complexity of the algorithm for the computation of the whole kernel, exploiting hermitian symmetry in Fourier space, is $O(4N_1 \cdot N_3 \cdot N_2^3)$, where N_1 and N_3 denote the number of modes in streamwise and spanwise directions, respectively, whereas N_2 is the number of points in the wall-normal direction.

The controlled channel flow is simulated numerically with DNS by using the computer code and computing system developed by Luchini & Quadrio[80]. The code is a parallel solver of the Navier-Stokes equations for the incompressible flow in a plane channel. Time advancement employs the usual semi-implicit approach, where nonlinear terms are advanced explicitly with a low-storage Runge-Kutta scheme, and viscous terms are advanced implicitly. The mixed spatial discretization employs Fourier expansions in wall-parallel directions, and fourth-order accurate compact explicit finite difference schemes discretize the wall-normal direction. The locality of finite difference operators in physical space allows to exploit a simple partitioning of the data among different computing machines, with excellent parallel performance. The amount of communication is reduced by a carefully designed parallel algorithm, so that the code can run on a computing system assembled without expensive networking hardware.

Direct numerical simulations of the controlled turbulent channel flow are performed at three values of the Reynolds number, namely $Re = 1450$, $Re = 3333$ and $Re = 6882$. The simulation with the lowest Re will be referred to in the following as case **L**; the one with the medium value as case **M**, and the one with the highest value of Re as case **H**. In all the three simulations the computational domain has dimensions of $L_1 = 4\pi\delta$ and $L_3 = 2\pi\delta$. The integration time for cases **L**, **M** and

H is $TU_b/\delta = 1500$, $TU_b/\delta = 1000$ and $TU_b/\delta = 500$, respectively. The spatial resolution is kept constant in inner units as Re increases; details on the number of modes / points employed in each simulation and its space-time resolution are reported in Table A.1. The initial condition for every simulation is a velocity field of a fully developed turbulent channel flow, each adapted to the required value of Re. The temporal integration scheme used to advance the governing equations is also used to integrate the control derivative $\dot{\phi}(\hat{x_1}, \hat{x_3}, t)$ from a zero initial condition to obtain the control history.

Initial response to control action

When the controller is turned on at $t = 0$, the turbulent flow exhibits a transient response before ultimately reaching a new statistically stationary equilibrium state. It is interesting to focus on the transient response of the longitudinal shear stress. Figure A.1 (top) shows the initial evolution of the space-averaged friction in response to the control action; here quantities are made non-dimensional with the *friction velocity of the uncontrolled flow*, since this is the appropriate reference velocity when $t \to 0^+$. The three responses peak at $t^+ \approx 4$ and, more importantly, responses in cases **M** and **H** almost collapse. The response for case **L** presents the same qualitative behavior, but with quantitative differences, and this may be a low-Reynolds-number effect. This result suggests that the initial transient response of the wall shear stress is a property associated to the inner layer of the uncontrolled turbulent flow.

A similar behavior is found in the initial history of the control power P_ϕ, defined as[12]:

$$P_\phi = \int_A \Big(|\phi| \frac{\rho \phi^2}{2} + |\phi(p - \overline{p})| \Big) dA,$$

where A denotes the area where control is applied (both channel walls in the present case), $p - \overline{p}$ denotes the fluctuation around the mean pressure, and ρ is the density of the fluid. Fig. A.1 (bottom) shows the initial transient of P_ϕ^+. The three curves peak at $t^+ \approx 1$; moreover, the responses in case **M** and **H** almost collapse, are not monotonic in the interval $0 < t^+ < 5$.

The initial response of other quantities characterizing the flow, namely, turbulent kinetic energy and dissipation, did not reveal the same scaling. This is an expected result, explained with the integral nature of energy and dissipation, that involves contributions from fluctuations residing both in the inner and the outer layer.

Statistics

After the initial transient has elapsed, the LQR-controlled channel flow features peculiar statistics. These are discussed in the following, where variables with the

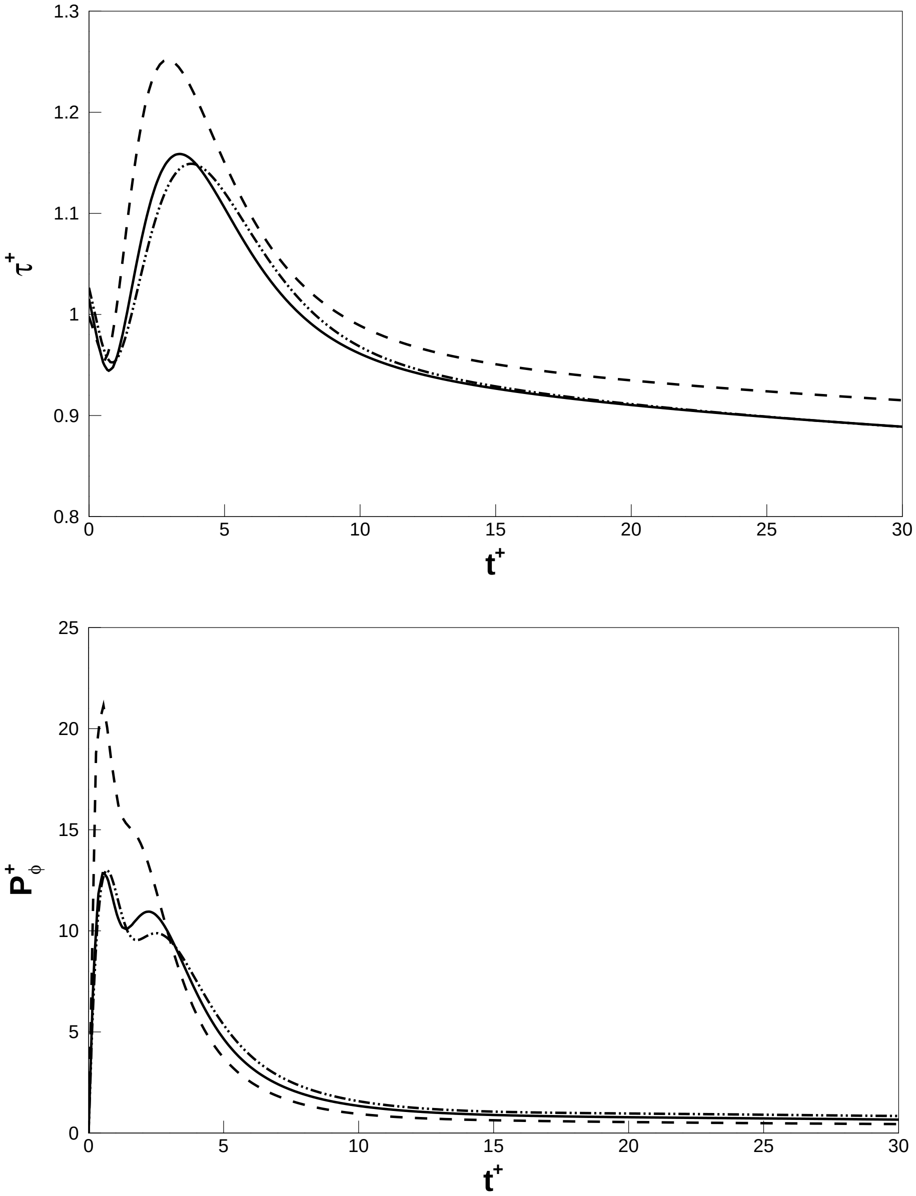

Figure A.1: Top: Initial response of the space-averaged wall shear stress τ^+. Bottom: initial history of the control power P^+_ϕ. Case **L** (dashed), case **M** (solid), and case **H** (dot-dashed). Each curve is obtained by ensemble averaging over the two walls and over 10 realizations of the initial transient, starting from independent initial conditions. Quantities are made non-dimensional with wall variables of the uncontrolled flow.

$+$ superscript are now made non-dimensional with the viscosity and the *friction velocity of the controlled flow*.

We first look at the mean velocity profile U^+. A Taylor series expansion of the ratio U^+/y^+:

$$\frac{U^+}{y^+} = 1 + \frac{1}{2Re_\tau}\left[\frac{\delta}{u_\tau^2}\langle u_{y,w}\phi\rangle - 1\right]y^+ + \dots$$

highlights the effects of the control on the mean velocity profile. In this expression, $\langle\cdot\rangle$ is the averaging operator over time and homogeneous directions, and $u_{y,w}$ denotes the wall-normal derivative of the streamwise velocity at the wall. In the controlled case, the first-order coefficient $-1/2Re_\tau$ is modified by the presence of the non-zero term $\langle u_{y,w}\phi\rangle$. Its effect on the near-wall behavior of the mean velocity profile is shown in fig. A.2 (top), where the ratio U^+/y^+ is reported against y^+ for both the uncontrolled and controlled flows, in case **M**. The effect of the control is evident for $y^+ < 10$, and it is shown qualitatively that an increase in the size of the buffer layer is accompanied by a decreased thickness of the layer where the mean velocity profile is linear. The term $\langle u_{y,w}\phi\rangle$ is a function of Re_τ itself, and an increase of the Reynolds number emphasizes its effect, as shown in fig. A.2 (bottom); this figure also shows that, for all the Reynolds numbers considered,

$$\langle u_{y,w}\phi\rangle < \frac{u_\tau^2}{\delta} = -\frac{1}{\rho}\frac{d\overline{p}}{dx},$$

where $d\overline{p}/dx$ is the mean pressure gradient. It is noteworthy that the wall-normal velocity component ϕ at the wall depends, after its definition eq. (A.5), on the flow and its history; as a consequence, statistics of ϕ inherit in a nontrivial way features of the whole turbulent field. Hence, modifications of the near-wall behavior of mean velocity profiles may be associated to a strengthened coupling between the inner and outer layer with respect to the uncontrolled flow.

Semilogarithmic plots of the mean velocity profile for the uncontrolled and controlled flow are reported in fig. A.3. The controlled flow exhibits a log layer, with the same slope as the uncontrolled. An upward shift in the log layer is shown in fig. A.3 (top); this feature has been noticed in a large variety of drag-reduced turbulent wall flows. As expected, increasing the Reynolds number is associated to an increased extent of the logarithmic region.

We note here that similar effects were shown by Choi et al. [26] when using opposition control. In their work, the upward shift in the log law was attributed to an increased size of the viscous sublayer in presence of the control; this argument was supported with plots (similar to the present fig. A.2) where an increased size of the region where $U^+/y^+ \approx 1$ was reported. In the present case, the departure of the mean velocity profile from linearity is much more evident; however, the region where viscous stresses are dominant is thickened by the control. This can be noticed from fig. A.4, where the component $\langle uv\rangle^+$ of the Reynolds stress tensor is reported against y^+. Fig. A.4 (top) compares the $\langle uv\rangle^+$ profile of the controlled and

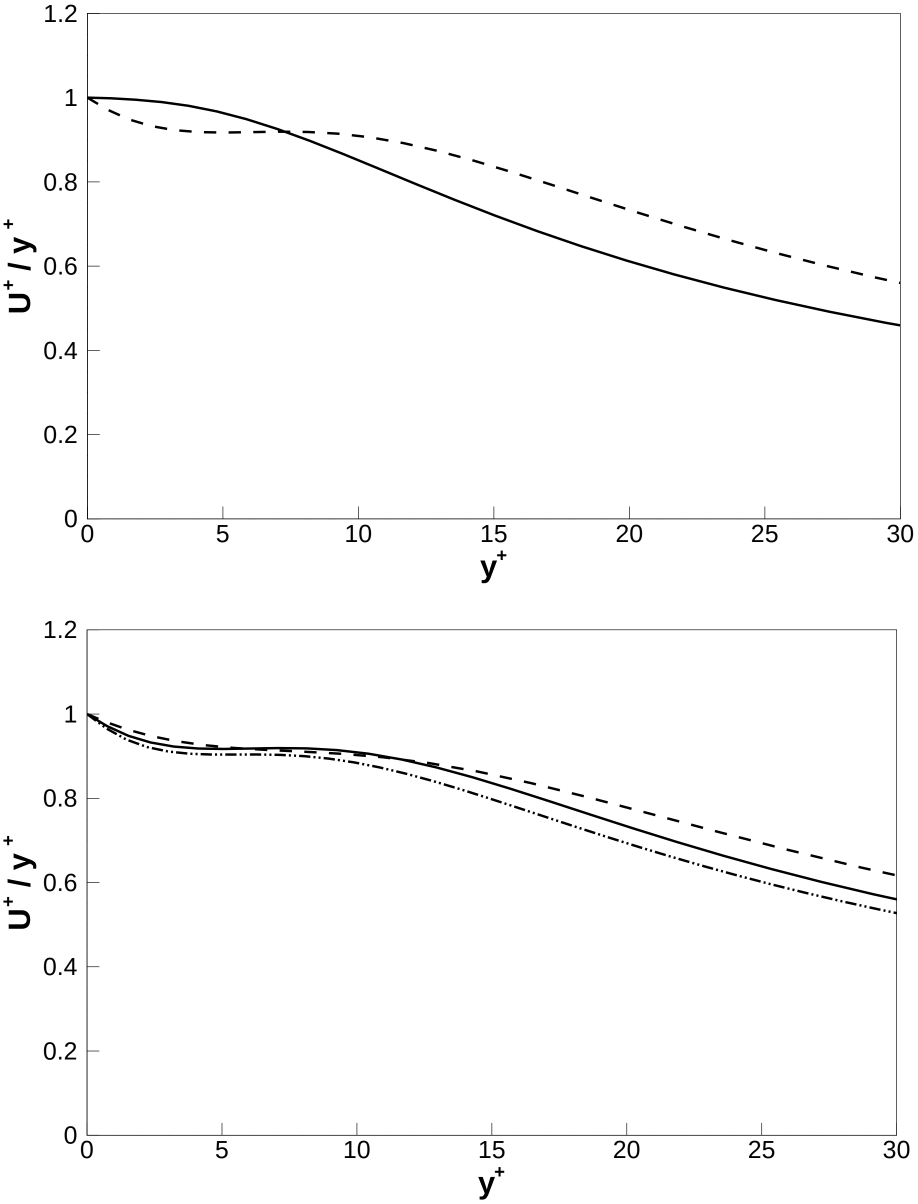

Figure A.2: Near-wall behavior of the mean velocity profile U^+. Top: comparison of the uncontrolled (solid) and controlled (dashed) flow for case **M**. Bottom: Reynolds number effect on the near wall behavior for case **L** (dashed), case **M** (solid) and case **H** (dash-dotted).

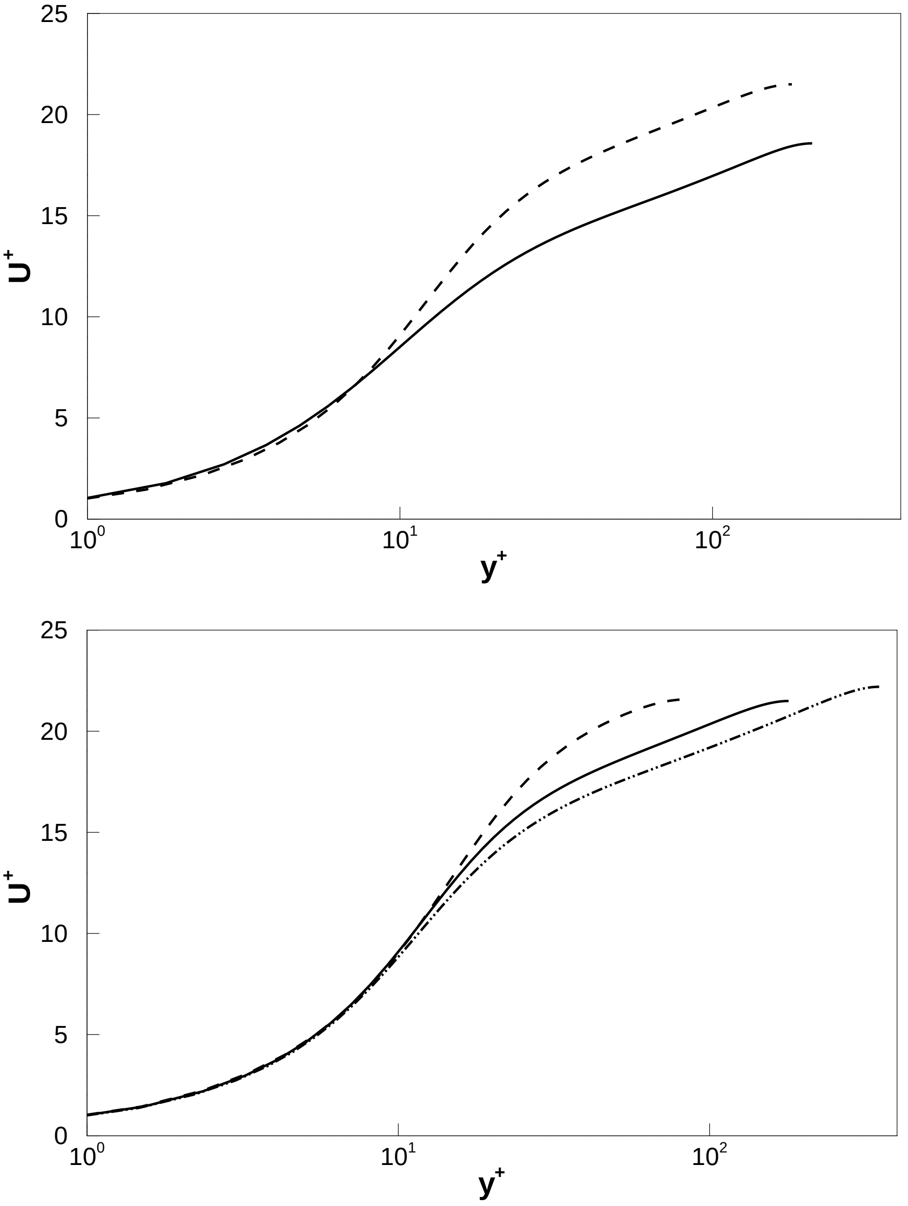

Figure A.3: Mean velocity profile in the law-of-the-wall form. Top: comparison of the uncontrolled (solid) and controlled (dashed) flow for case **M**. Bottom: Reynolds number effect on the mean velocity profile for case **L** (dashed), case **M** (solid) and case **H** (dash-dotted).

uncontrolled flow in case **M**; it is shown, indeed, that the region where Reynolds stresses are less than $\approx 10\%$ of the total stress widens from ≈ 5 to ≈ 10 wall units.

Taylor series expansion in y direction of the velocity components near the wall and application of boundary conditions reveal that, in the controlled case, the departure of the Reynolds stress profile from the wall is linear:

$$\langle uv\rangle^+ \approx \langle u_{y,w}\phi\rangle^+ y^+ + \dots$$

instead of the usual behavior $\sim {y^+}^3$ in uncontrolled channel flow. The intensity of the fluctuations is reduced along the whole channel, but for the region $y^+ < 5$. An increase in the value of the Reynolds number modifies the curve in terms of amplitude and position of the local minimum and global maximum, while the position of the near-wall local maximum apparently is not changed with Re.

The variance of the streamwise and wall-normal velocity fluctuations $\langle uu\rangle^+$ and $\langle vv\rangle^+$ is reported in fig. A.5 and fig. A.6. The component $\langle ww\rangle^+$ of the Reynolds stress tensor is slightly affected by the control and it is not reported here. Top frames of both figures compare the uncontrolled and controlled flow for case **M**. Control reduces the intensity of fluctuations, and in particular the peak intensity of $\langle uu\rangle^+$ is moved toward the center of the channel. In the near wall region, this profile is not monotonic with y^+, and a local maximum and minimum are present. These features characterize the whole Reynolds number range considered, as shown in fig. A.5 (bottom). The wall-normal velocity fluctuation $\langle vv\rangle^+$ is affected by the non-homogeneous boundary condition on v, and this explains the non-zero variance at $y^+ = 0$. A local minimum is present at about $y^+ \approx 5$; the same feature was reported by Choi et al. [26], and was then associated by Hammond et al. [45] to the presence of a so-called virtual wall inside the flow. For $y^+ > 10$, the $\langle vv\rangle^+$ fluctuations in the controlled case are reduced, but the peak is located nearly in the same position of the controlled case. Reynolds number increase affects the intensity of the fluctuations, but the overall behavior of the curves does not change significantly (see fig. A.6 (b)). We also note here that, by Taylor series expansion of the v component near the wall, and using continuity, one obtains:

$$\langle vv\rangle^+ = \langle \phi\phi\rangle^+ + \langle \phi v_{yy,w}\rangle^+ {y^+}^2 + \dots$$

where $v_{yy,w}$ denotes the second derivative of v at the wall. It can be seen from fig. A.6 that the term $\langle \phi v_{yy,w}\rangle$ is negative, for the three values of Re considered; this fact was evident also in in the data of Choi et al. [26] when using opposition control.

The production term $\Big(-\langle uv\rangle dU/dy\Big)^+$ in the balance equation for the turbulent kinetic energy is reported in fig. A.7 (top) for the uncontrolled and controlled flow in case **M**. It is interesting to note that, although the intensity of the components of the Reynolds stress tensor is reduced along most of the channel, the production of turbulent kinetic energy is reduced in the range $5 < y^+ < 15$ only, i.e. where the production of the uncontrolled flow peaks. Outside this range, the production

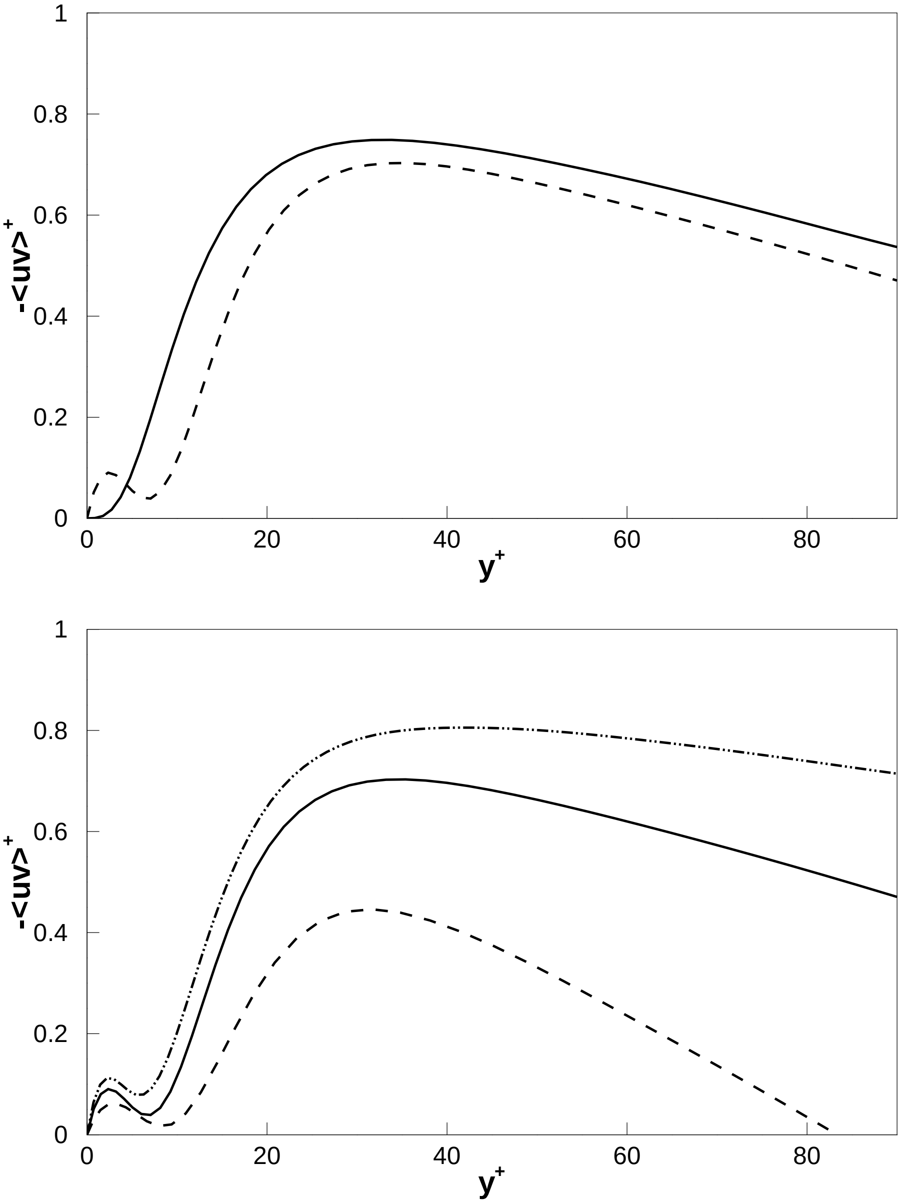

Figure A.4: Reynolds stresses $\langle uv \rangle^{+}$. Top: comparison of the uncontrolled (solid) and controlled (dashed) flow for case **M**. Bottom: Reynolds number effect on the profile of $\langle uv \rangle^{+}$; curves for case **L** (dashed), case **M** (solid), case **H** (dash-dotted).

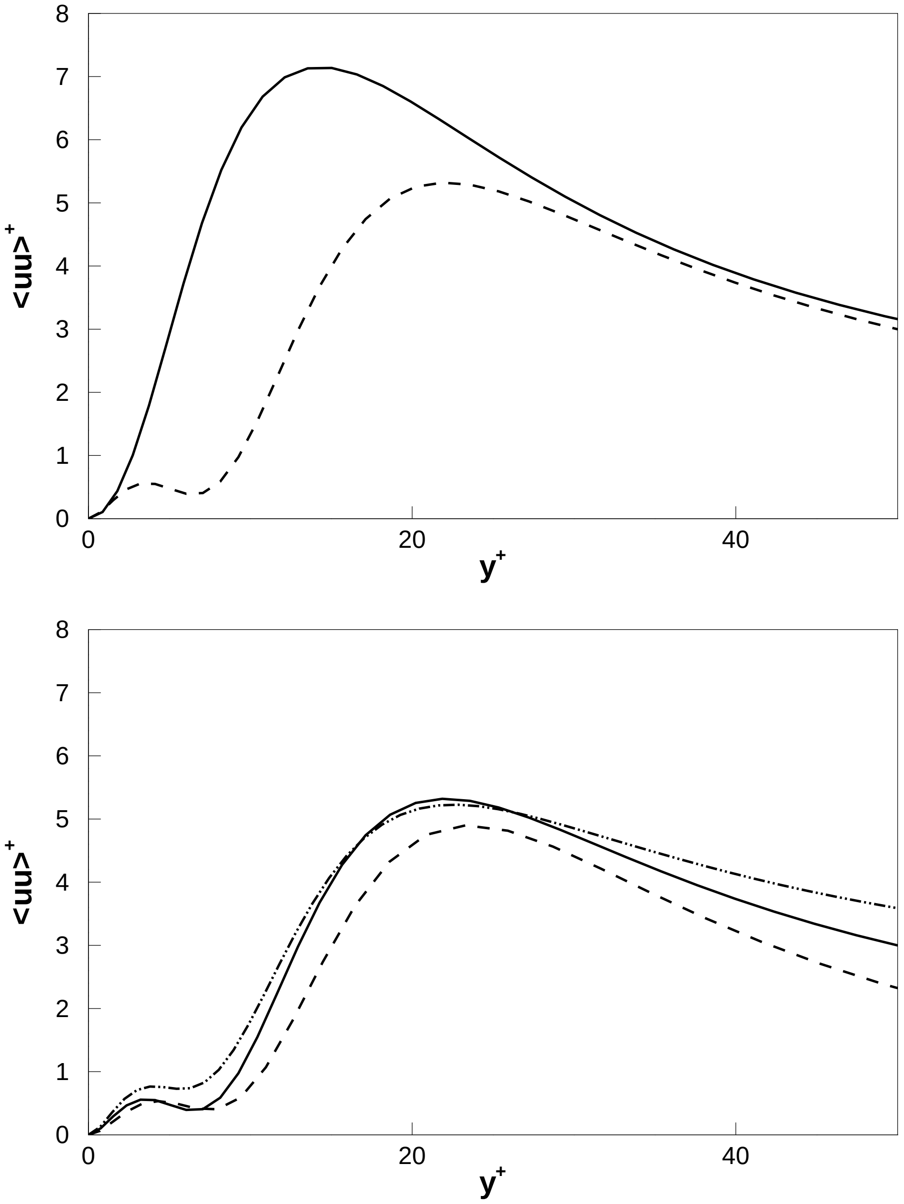

Figure A.5: Reynolds stresses $\langle uu \rangle^+$. Top: comparison of the uncontrolled (solid) and controlled (dashed) flow for case **M**. Bottom: Reynolds number effect on the profile of $\langle uu \rangle^+$; curves for case **L** (dashed), case **M** (solid), case **H** (dash-dotted).

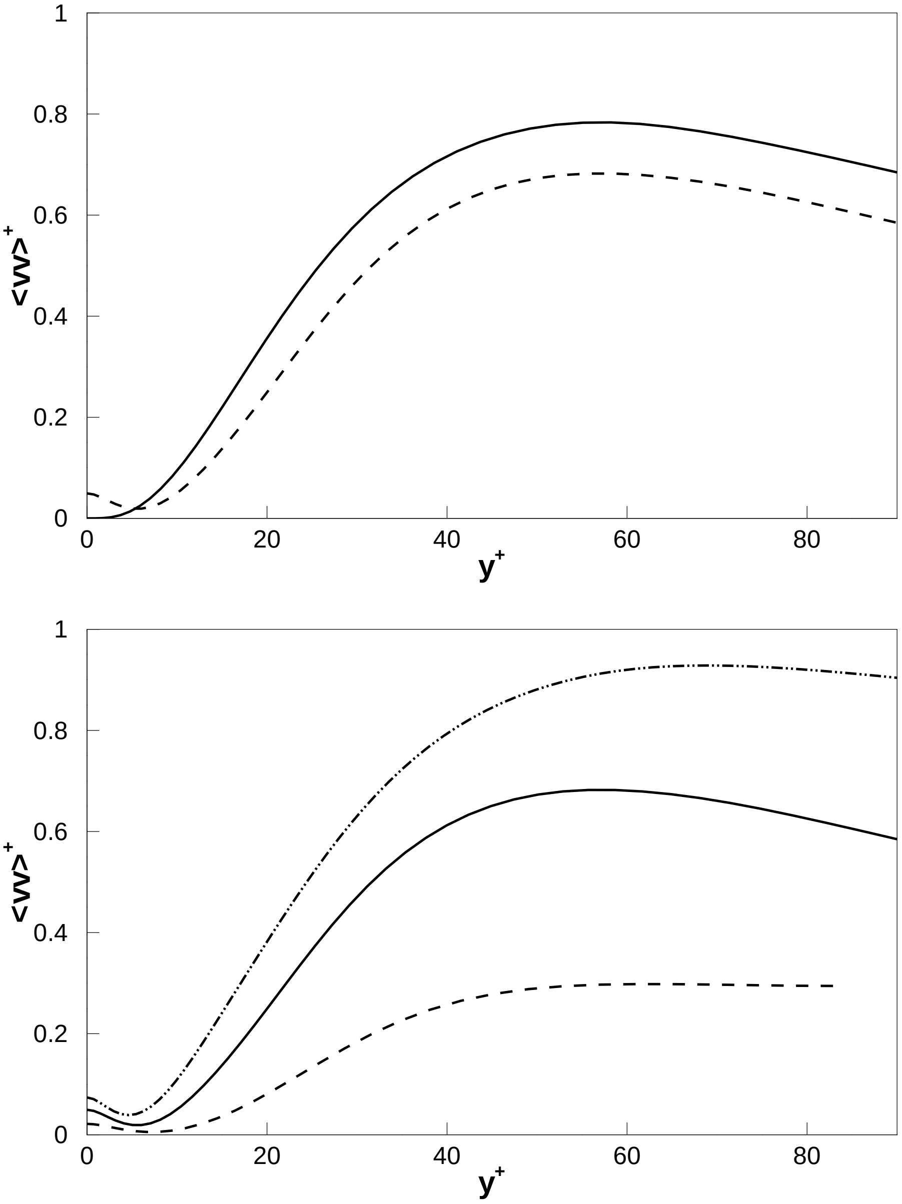

Figure A.6: Reynolds stresses $\langle vv \rangle^+$. Top: comparison of the uncontrolled (solid) and controlled (dashed) flow for case **M**. Bottom: Reynolds number effect on the profile of $\langle vv \rangle^+$; curves for case **L** (dashed), case **M** (solid), case **H** (dash-dotted).

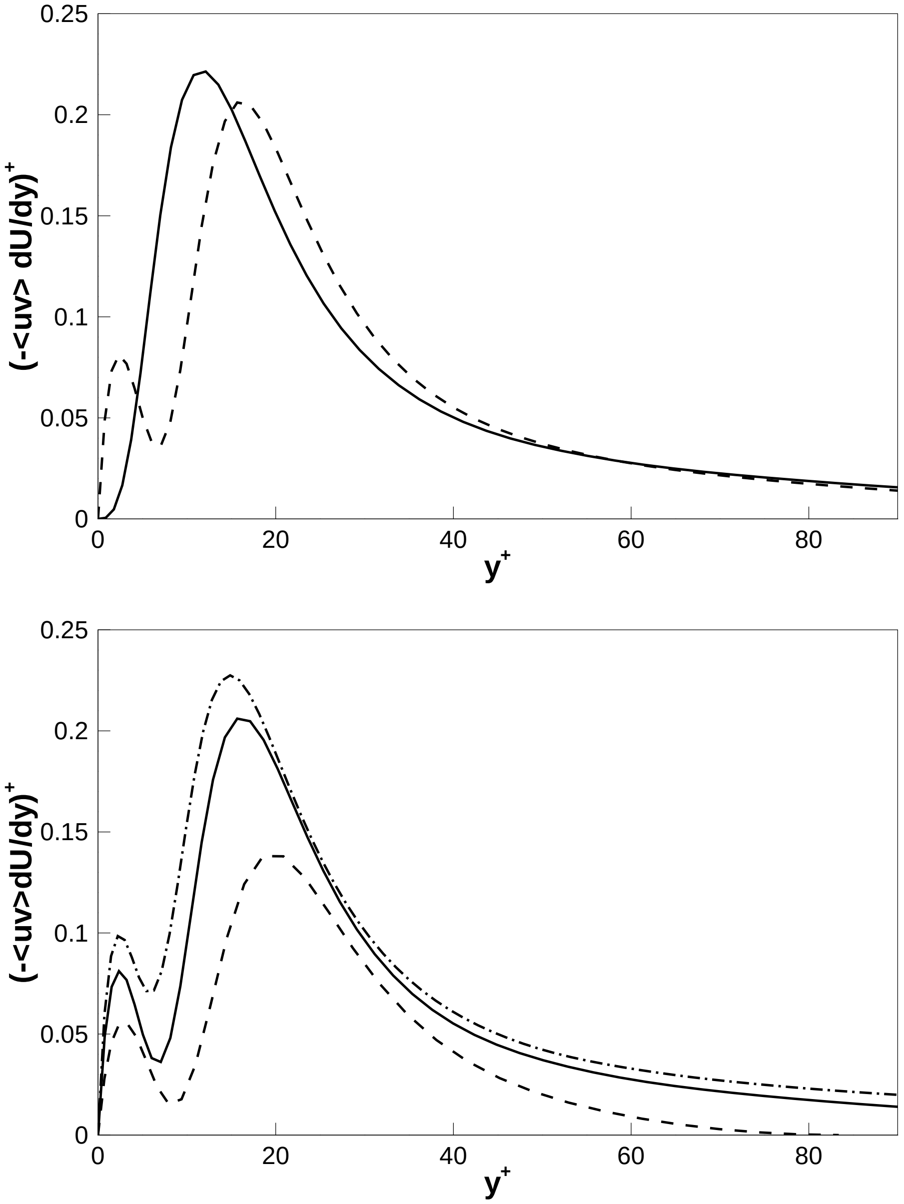

Figure A.7: Production term of turbulent kinetic energy $-\left(\langle uv\rangle dU/dy\right)^+$. Top: comparison of the uncontrolled (solid) and controlled (dashed) flow for case **M**. Bottom: Reynolds number effect on the profile of $-\left(\langle uv\rangle dU/dy\right)^+$; curves for case **L** (dashed), case **M** (solid), case **H** (dash-dotted).

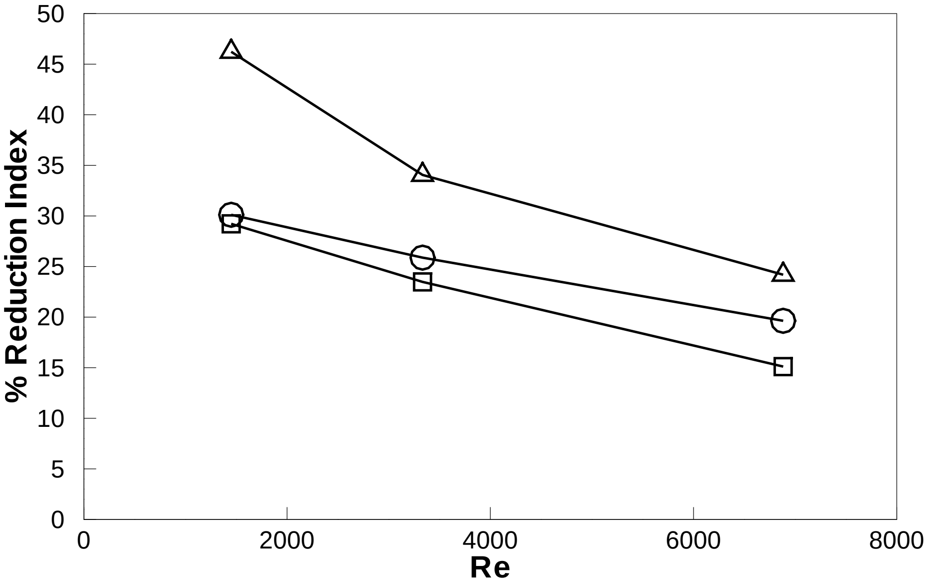

Figure A.8: Performance of the controller as a function of Re. △: Turbulent kinetic energy. ○: Skin friction drag. □: Net power saved.

for the controlled flow exceeds the one of the uncontrolled flow, at least with the present scaling. A Reynolds number increase (fig. A.7 (bottom)) does not affect the general shape of the curves, and affects slightly the positions of the extrema in the y direction .

Performance

Skin friction drag and turbulent kinetic energy are significantly reduced in the controlled turbulent flow, if compared with the uncontrolled flow at the same Re. This effect is quantified by introducing the following drag reduction (DR) and energy reduction (ER) indexes:

$$DR = 100\frac{\tau_r - \tau_c}{\tau_r}, \qquad ER = 100\frac{E_r - E_c}{E_r},$$

where the subscripts r and c stand for the reference and controlled flow, respectively, and E denotes the turbulent kinetic energy. The power reduction index (expressing the net power saved when applying the controller) is defined as:

$$PR = 100\frac{P_r - P_c}{P_r}$$

where P_c is the sum of the time average of P_ϕ and the (reduced) power required to drive the flow against the viscous shear stress. In the evaluation of these indexes, care has been exercised in properly removing the transient initial response of the turbulent channel flow to the control action. Values of these performance indexes are reported in fig. A.8 against Re. Fig. A.8 shows that energy reduction is most affected by the Re increase, while drag and power reduction decrease almost linearly with Re. It is shown that, in case **H**, 20% drag reduction is achieved with 15% of net power saved with respect to the uncontrolled case. In terms of drag reduction, these results slightly outperform the opposition control [55] at comparable Reynolds number. However, the trend which emerges from our simulations is definitely one of decreasing DR with increasing Re, in contrast with the opposition-controlled flow, whose drag-reducing performance above $Re_\tau = 100$ has been shown to be practically independent of Re.

Drag reduction mechanism

To discuss the mechanism by which LQR control achieves turbulent drag reduction, we start by comparing the degree of anisotropy that characterizes the near-wall flow with and without control.

As shown by Lumley & Newman[84], anisotropy in a turbulent flow is properly quantified by the normalized anisotropy tensor a_{ij}, defined as:

$$a_{ij} = \frac{\langle u_i u_j \rangle}{\langle u_k u_k \rangle} - \frac{1}{3}\delta_{ij}$$

where δ_{ij} is the Kronecker symbol, and repeated indexes imply summation.

In particular the second and third invariants, II_a and III_a, of the tensor a_{ij} can be computed, to produce anisotropy invariant maps. In fig. A.9 these maps for the uncontrolled (top) and the controlled flow (bottom) are compared in case **M**. A point in the map identifies a particular wall distance y, to which the couple (III_a,II_a) is associated. All admissible turbulence states lie inside the triangular region, known as the Lumley triangle [99], delimited by black thick lines. In the uncontrolled case (fig. A.9, top), the usual anisotropy pattern of a turbulent channel flow is observed, namely, the turbulent flow is predominantly two-component in the near-wall region, and eventually moves towards the isotropic state in the center of the channel. The anisotropy invariant map for the controlled flow (fig. A.9, bottom) shows some special features. The point at $y = 0$ (not shown) is characterized by pure one-component turbulence (the control action), and is located on the right-top corner of the triangle. The very-near-wall velocity field changes along y from a condition of nearly axisymmetric turbulence strained by expansion (right side of the triangle, where the v component is much larger than the other two components) to a condition of nearly axisymmetric turbulence strained by compression (left side of the triangle, where the fluctuations of v are smaller than those of u and

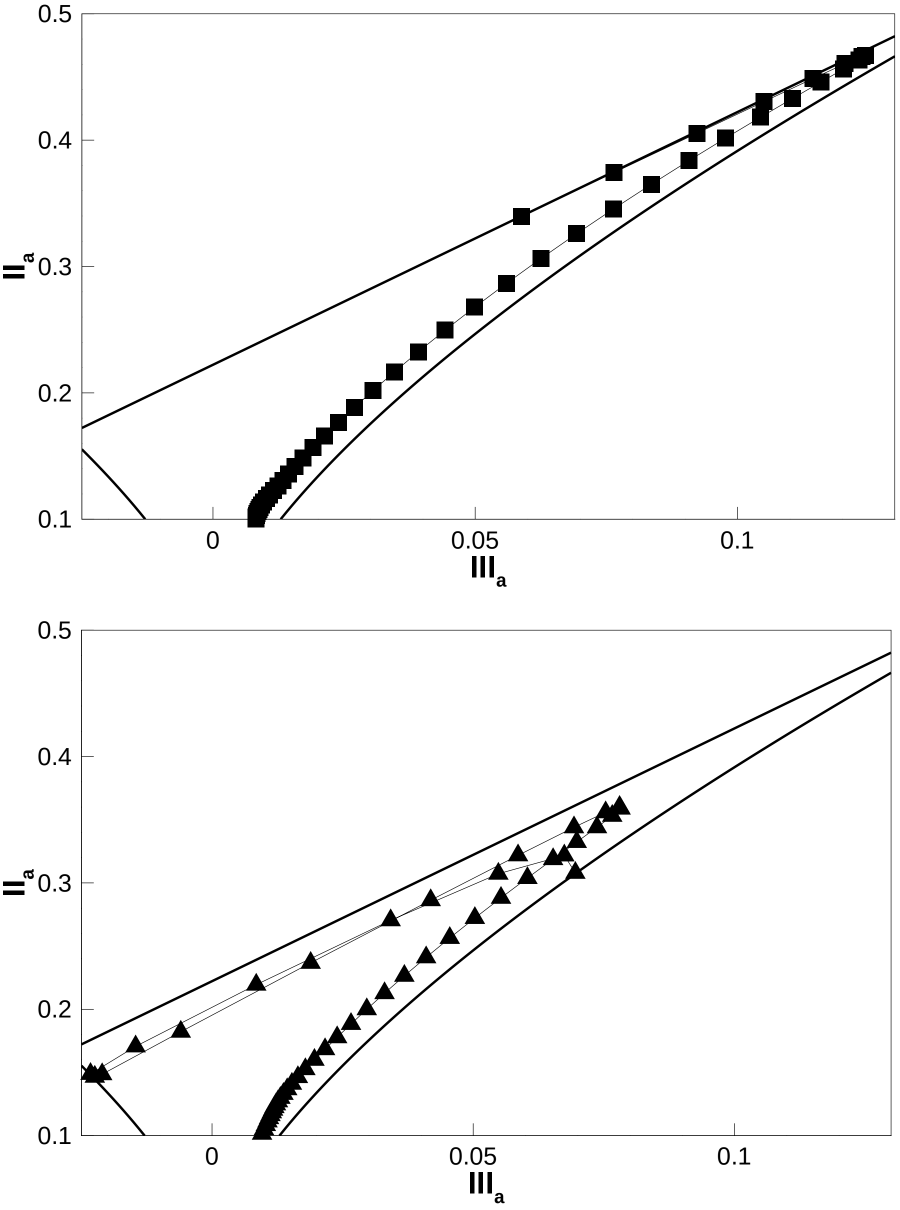

Figure A.9: Anisotropy invariant map for the uncontrolled (top) and controlled (bottom) flow for case **M**.

w) at $y^+ \approx 6$, the location corresponding approximately to the minimum of $\langle vv \rangle^+$. Locations closer to the centre of the channel tend towards the isotropic state, as in uncontrolled channel flow. A recent study [37] used the concept of anisotropy invariant mapping to characterize common features in drag-reduced turbulent wall flows. These authors noted that a large variety of such flows were characterized by increased level of anisotropy (towards the one-component state) of the flow in the near wall region. The present results show that this interpretation does not apply in the present case, where the anisotropy pattern of the flow is fairly more complex.

To gain some insight on the effects of increasing Re on drag reduction, we use the result, recently demonstrated by Fukagata et al. [38], that the friction coefficient in a turbulent channel flow at fixed flow rate can always be expressed as:

$$C_f = \frac{3}{Re} + 6 \int_0^1 (y-1)\langle uv \rangle \, dy$$

even when wall blowing and suction with zero net mass flux is applied.

In this relation, the first term is the laminar contribution, and the second is a weighted integral of the Reynolds stress component $\langle uv \rangle$ across the channel. The integrand $(y-1)\langle uv \rangle$ is plotted against y in fig. A.10, for the uncontrolled and controlled flows, cases **L** and **H**. The difference in the areas under the two curves is directly proportional to the drag reduction. It is shown that the effect of the control causes a negligible positive contribution to the total drag for $y \to 0$, and this effect becomes less and less important at higher Re. It is interesting to note that, in the controlled case, an increase of the value of the Reynolds number causes the peak value to increase and its position to become closer to the one of the uncontrolled flow, squeezing the area under the curve in the near wall region, hence decreasing the drag reduction amount.

Finally, the drag reduction mechanism may also be investigated by means of visualizations of the instantaneous velocity fields in the controlled case, to verify whether a link between LQR control and opposition control can be visually established.

In fig. A.11, surfaces of constant $(uv)^+ = -3$ are visualized, and colored according to the value of the vertical velocity, to highlight that a pattern emerges where wall suction is applied under ejection events (regions with $u < 0$ and $v > 0$), whereas wall blowing tends to be associated with sweep events (regions with $u > 0$ and $v < 0$). Similar conclusions can be drawn from the analysis of fig. A.12, where two views of the channel wall are presented, separately picturing blowing with high-speed streaks and suction with low-speed streaks.

Discussion and conclusions

This paper has described LQR controllers applied to turbulent channel flow for drag reduction, and has focused on their performance at different Re. We have stud-

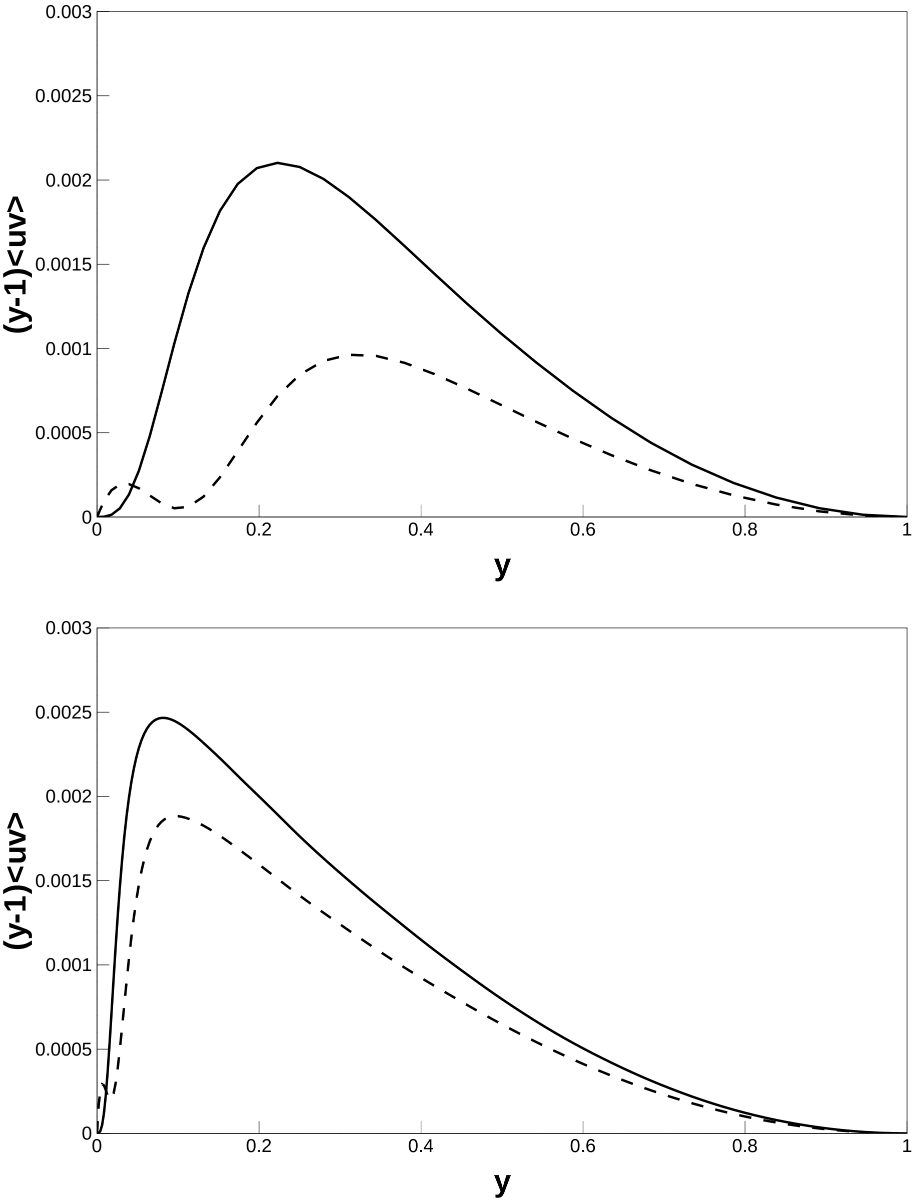

Figure A.10: Weighted Reynolds stress contribution $(y-1)\langle uv\rangle$ for case **L** (top) and case **H** (bottom). Comparison of the uncontrolled (solid) and controlled (dashed) flow.

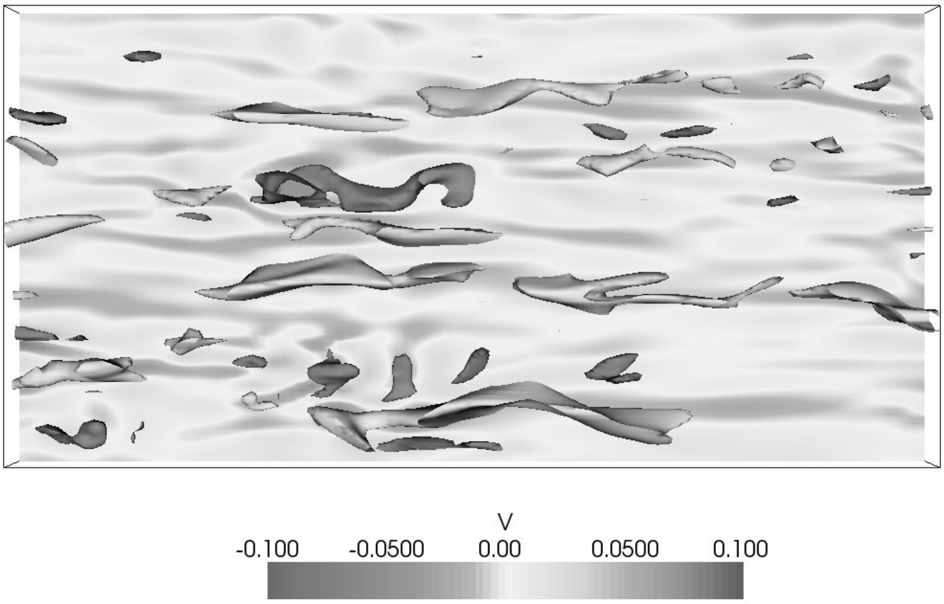

Figure A.11: Visualization of surfaces at constant value of $(uv)^+ = -3$ in the controlled flow, in a subset of the computational domain with size $L_1/2 \times L_3/2$ in streamwise and spanwise direction, and $y^+ < 60$. Surfaces are colored according to the local value of the vertical velocity v. Light surfaces correspond to ejection events, whereas dark correspond to sweeps. The wall (lower surface) is colored according to the same scheme, showing that, typically, wall blowing/suction is applied underneath sweep/ejection events, respectively.

ied the effects of this control strategy at values of Re significantly higher than those ever reported in the literature. Though this issue is certainly of crucial relevance in assessing the feasibility of a control strategy for practical applications, LQR control has been studied to date with DNS at very low values of Re, owing to the huge size of the computational problem, where computing the control kernels is significantly demanding.

Results presented in this paper suggest that LQR control, that uses optimal control theory by relying upon a linearized model of the system, shares some of its features with opposition control [26], that in contrast derives its control law from an informed guess driven by physical intuition alone. Statistics of the controlled flow and flow visualizations suggest that the LQR controller interacts favourably with near-wall structures, counteracting the sweep and ejection events, and ultimately acts with a mechanism which definitely resembles, at least qualitatively, that of the opposition control. It becomes thus natural to compare the two control strategies in terms of performance degradation at relatively high Re. On one side, opposition control has been shown [55] to present a low (if any) sensitivity to Re in terms of amount of drag reduction. This is at odds with the LQR controller, whose performance have been shown here to degrade significantly. Moreover, the net power

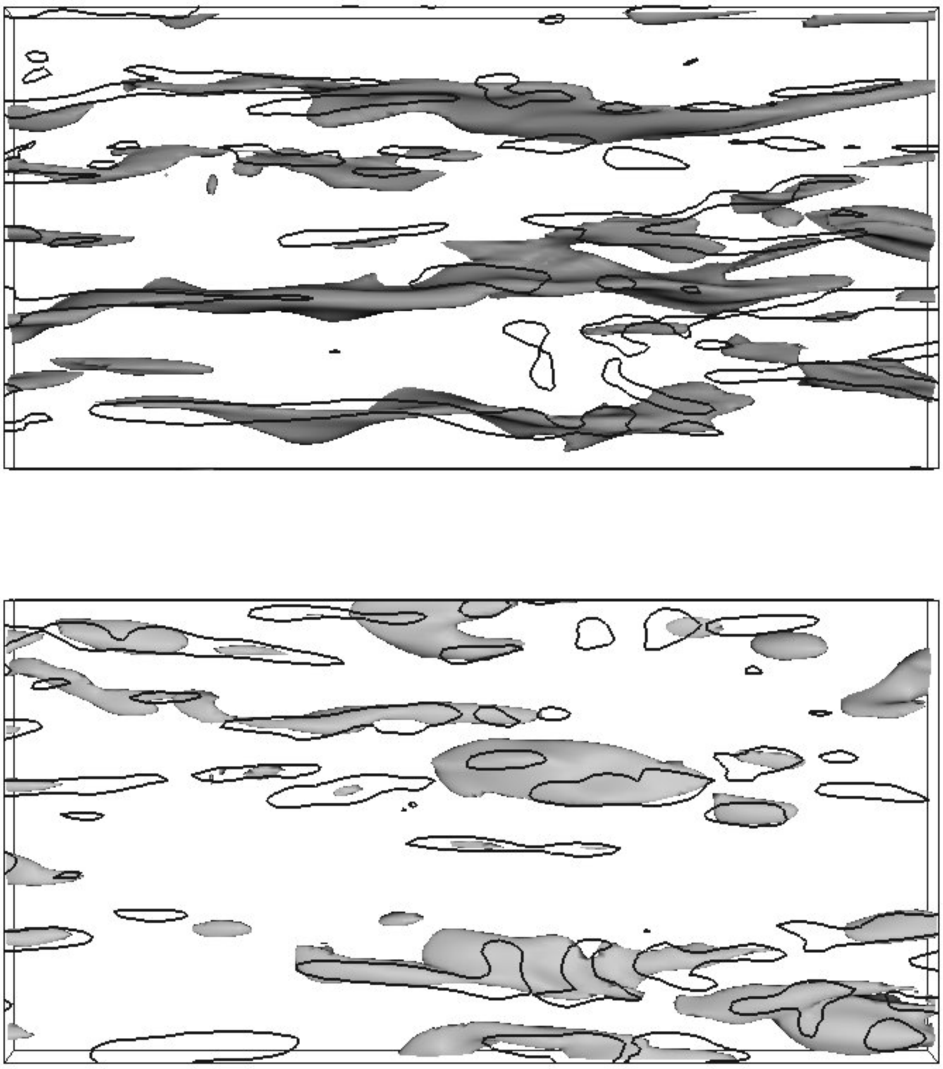

Figure A.12: Visualization of high (light, bottom) and low (dark, top) speed streaks $u^+ = \pm 3$ in the same subset of the computational domain as in fig. A.11. View from below; black lines (at the wall) are at constant wall-normal velocity $v^+ = 0.2$ (bottom) and $v^+ = -0.2$ (top). It is shown that, typically, wall blowing/suction is located underneath the high/low speed streaks, respectively.

saved as a function of the Reynolds number decreases almost linearly from $\approx 30\%$ at the lowest Re to $\approx 15\%$ in case **H**: this results is particularly worrying, especially if one considers that the present results might still be affected by residual low-Re effects, as pointed out by Moser et al. [91].

While this is certainly not good news for LQR control, it is as yet unclear, however, how far-reaching the significance of this result really is. The maximum Reynolds number tested in this work is limited by computational resources, and it is not yet high enough to exclude that performance degradation will disappear as soon as low-Re-effects are suppressed. On the other hand, the two techniques are quite similar in terms of physical mechanism. It is our opinion that a possibility exists to exploit the few design degrees of freedom available in LQR control to further increase performance and at the same time to obtain a smaller performance degradation with Re, or no degradation at all.

It is worth recalling that the asymptotic performance of active controllers at high Reynolds numbers has been studied theoretically by Iwamoto et al. [54]. They have hypothesized that the control system is capable of completely suppressing velocity fluctuations in the near-wall region, and have demonstrated that such a controller could yield good performance at high Reynolds number too. We notice that this theoretical result does not apply to the present case, since our controllers increase, or at least do not reduce, the intensity of near-wall fluctuations when compared to the uncontrolled case.

Finally we conclude with the observation that the success of LQR control provides further indirect support to the idea that linear mechanisms, related to the Orr-Sommerfeld-Squire operator and in particular to the linear coupling term, play an important role in the non-linear, self-sustaining mechanism of the turbulence wall cycle [66]. The present controller, thanks to the model-based design that accounts for the linear dynamics of the system, is indeed capable of targeting these linear mechanisms and of weakening the wall cycle.

Appendix B

Feedback control of transient energy growth in subcritical plane Poiseuille flow

Active suppression of the transient energy growth in subcritical plane Poiseuille flow is addressed. It is assumed that the time derivative of the wall-normal velocity component can be imposed at the walls as the control input, and that full-state information is available. We show first that it is impossible to design a linear state-feedback controller that leads to a closed-loop system without transient energy growth. In a second step, a linear state feedback many wavenumber controller kernel, targeting directly the transient growth mechanism, is designed, and its performance successfully tested in a fully nonlinear simulation.

Introduction

Transient energy growth has recently been recognized as a possible mechanism explaining subcritical transition in wall-bounded flows. In fact, subcritical flows may experience large transient amplifications of the energy of perturbations, that could trigger nonlinear mechanisms and lead to transition to turbulence[20; 110; 122; 77].

Many recent attempts in the active control of transitional flows have targeted this transient growth mechanism. In recent works Corbett & Bottaro[30] addressed the control of two- and three-dimensional nonmodal disturbances in boundary-layer flows in the framework of optimal control theory, and Zuccher et al.[142] applied steady suction for attenuating the growth of assigned optimal disturbances in a Blasius boundary layer. In plane Poiseuille flow, optimal and robust control theory was applied to a state-space model derived after discretization of the Orr-Sommerfeld-Squire equations, by Bewley & Liu[15] for a single wavenumber pair and by Högberg et al.[49] for a large array of wavenumber pairs. This led to a reduction of the maximum transient growth as well as to an increase in transition thresholds. Despite these efforts, however, to date no feedback control law has been ever found that is capable of ensuring that the closed-loop system does not admit transient energy growth, or, in other words, is *strictly dissipative*. Such control law is the subject of the present paper.

The problem of designing active controllers with constraints on some norm of the state trajectory has received attention in the analysis of a class of partially linear cascade systems [130], and more recently in conjunction with a linear matrix inequality (LMI) approach [98; 97]. In a fairly recent paper, Whidborne & McKernan [136] extended these results, and gave conditions for the existence of a feedback controller that ensures the strict dissipativity of the closed-loop system.

Leveraging these results, in the present paper we will show that it is impossible to design a linear state-feedback controller ensuring the controlled plane Poiseuille flow to be strictly dissipative. Then, using a recently developed technique [85; 137], we will compute an upper-bound minimizing controller; its performance will be tested in a fully nonlinear simulation.

Problem formulation

We consider the dynamics of small perturbations to the laminar Poiseuille solution in a plane channel. A cartesian coordinate system is introduced, where x, y denote the streamwise and wall-normal directions, and u, v denote the corresponding perturbation velocity components. The Navier-Stokes equations, linearized around the laminar solution $U(y) = U_p(1-y^2)$, are non-dimensionalized with the centreline velocity U_p and the channel half-width δ, and rewritten in the form of a single equation for v. Fourier transformation in x direction yields the well known Orr-Sommerfeld form:

$$\Delta\dot{\tilde{v}} = [-j\alpha U\Delta + j\alpha U'' + \Delta\Delta/Re]\tilde{v} \tag{B.1}$$

at the streamwise wavenumber α. In this expression, the tilde denotes Fourier coefficients, j is $\sqrt{-1}$, $\Delta = d^2/dy^2 - \alpha^2$, and $Re = U_p\delta/\nu$ is the Reynolds number, ν being the kinematic viscosity of the fluid. We select boundary conditions representing time-varying wall-normal transpiration:

$$\begin{aligned} \tilde{v}(y=1,t) &= \tilde{q}_u(t), \\ \tilde{v}(y=-1,t) &= \tilde{q}_\ell(t), \\ \frac{\partial\tilde{v}}{\partial y}(y=\pm1,t) &= 0. \end{aligned} \tag{B.2}$$

These conditions are enforced by representing $\tilde{v}$ as a homogeneous component $\tilde{v}_h(y,t)$ plus inhomogeneous (actuation) components $f_u(y)\tilde{q}_u(t)$, $f_\ell(y)\tilde{q}_\ell(t)$

$$\tilde{v}(y,t) = \tilde{v}_h(y,t) + f_u(y)\tilde{q}_u(t) + f_\ell(y)\tilde{q}_\ell(t), \tag{B.3}$$

where $f_u(y) = (-y^3 + 3y + 2)/4$ and $f_\ell(y) = (y^3 - 3y + 2)/4$ are inhomogeneous functions for the upper and lower wall actuations, respectively[85]. All components of $\tilde{v}$ have vanishing y derivatives at the walls. We discretise $\tilde{v}_h$ in the wall-normal direction using a modified Chebyshev series cardinal function basis

$$\tilde{v}_h(y,t) = \sum_{0}^{N-4} \Gamma_n^{DN}(y) a_{v,n}(t), \tag{B.4}$$

where the modified Chebyshev functions $\Gamma_n^{DN}(y)$ implicitly enforce the required homogeneous Dirichlet and Neumann boundary conditions, lead to good conditioning of the discrete Laplacian operator, and are such that no spurious modes are generated [85].We then evaluate the equations on a set of Gauss-Lobatto collocation points in y direction, i.e. $y_k = \cos(\pi k/N), k = 2, \ldots, N-2$, to obtain the system of equations

$$\mathbf{E}\mathbf{a} + \mathbf{F}\mathbf{q} = \mathbf{L}\dot{\mathbf{a}} + \mathbf{G}\dot{\mathbf{q}}, \tag{B.5}$$

where $\mathbf{q} = (\tilde{q}_u, \tilde{q}_\ell)^T$ and $\mathbf{a} = (a_{v,0}, \ldots, a_{v,N-4})^T$. Finally we rearrange the equations as actuation by rate of change of transpiration $\dot{\mathbf{q}}$ instead of a combination with transpiration $\mathbf{q}$ [49]

$$\begin{pmatrix} \dot{\mathbf{a}} \\ \dot{\mathbf{q}} \end{pmatrix} = \begin{pmatrix} \mathbf{L}^{-1}\mathbf{E} & \mathbf{L}^{-1}\mathbf{F} \\ \mathbf{0} & \mathbf{0} \end{pmatrix} \begin{pmatrix} \mathbf{a} \\ \mathbf{q} \end{pmatrix} + \begin{pmatrix} -\mathbf{L}^{-1}\mathbf{G} \\ \mathbf{I} \end{pmatrix} \dot{\mathbf{q}}$$

i.e. as a linear time-invariant plant[127]

$$\dot{\mathbf{x}}(t) = \mathbf{A}\mathbf{x}(t) + \mathbf{B}\mathbf{u}(t), \quad \mathbf{x}(0) = \mathbf{x}_0, \tag{B.6}$$

where $\mathbf{A}$, $\mathbf{B}$ are constant system and input matrices, and $\mathbf{u}$, $\mathbf{x}$ are respective input and state vectors, and where we have transformed $\mathbf{x}$ such that the system energy is $\mathbf{x}^H\mathbf{x}$[127].

Theorem

We now recall a theoretical result that will be exploited in the sequel. We consider the linear time-invariant plant (B.6) and further assume that $\mathbf{B}^H\mathbf{B} > 0$, that is $\mathbf{B}$ has full column rank (i.e. all the actuators are independent). As shown by Whidborne & McKernan[136, Theorem 1], a static state-feedback controller $\mathbf{u} = \mathbf{K}\mathbf{x}$ exists, where $\mathbf{K}$ is a constant matrix, such that the closed-loop system possesses strict dissipativity (i.e. energy $\mathbf{x}^H\mathbf{x}$ decays monotonically from all initial conditions $\mathbf{x}_0$), if and only if

$$\mathbf{B}^\perp \left(\mathbf{A} + \mathbf{A}^H\right) \mathbf{B}^{\perp H} < 0 \text{ or } \mathbf{B}\mathbf{B}^H > 0, \tag{B.7}$$

where $\mathbf{B}^\perp$ is the left null space of $\mathbf{B}$. Additionally[136], if no static controller that achieves strict dissipativity exists, then no dynamic state-feedback controller, where

$\mathbf{u}$ is given from $\mathbf{x}$ by the dynamic system

$$\begin{aligned} \dot{\mathbf{x}}_k(t) &= \mathbf{A}_k\mathbf{x}_k(t) + \mathbf{B}_k\mathbf{x}(t), \quad \mathbf{x}_k(0) = \mathbf{x}_{k0}, && \text{(B.8)} \\ \mathbf{u}(t) &= \mathbf{C}_k\mathbf{x}_k(t) + \mathbf{D}_k\mathbf{x}(t), && \text{(B.9)} \end{aligned}$$

where $\mathbf{A}_k$,$\mathbf{B}_k$, $\mathbf{C}_k$ and $\mathbf{D}_k$ are constant matrices and $\mathbf{x}_k$ are controller states, exists either. The theorem is actually more general, as it states[136] additional criteria in the case of a static and dynamic *output* feedback controller.

We now move to applying the theorem to the present system. It is immediate to verify that the second criterion in (B.7) is never satisfied in the present system, as the hermitian matrix $\mathbf{BB}^H$ is never positive definite but is always positive semidefinite, since the dimension of the input vector is always smaller than the one of the state vector.

On the other hand, verifying the first algebraic criterion in (B.7) is not trivial, and thus we opt for a numerical verification. In particular, the state-space model (B.6) is first obtained on a fine grid and then truncated, as suggested by Reddy & Henningson[110], by retaining a limited number N_t of eigenfunctions, while discarding the ones corresponding to highly damped eigenvalues. This leads to a reduced-order model $\mathbf{A}_r$,$\mathbf{B}_r$, and the negative-definitess of the corresponding matrix $\mathbf{B}_r^{\perp}\left(\mathbf{A}_r + \mathbf{A}_r^H\right)\mathbf{B}_r^{\perp H}$ in (B.7) is verified by computing its maximum (real) eigenvalue λ_{max}, for an array of (Re, α) pairs. Figure B.1 shows the present result along with the well-known result on the transient growth dependence on (Re, α) in plane Poiseuille flow[110] (i.e. the open-loop case). The white area corresponds to the domain where the open-loop system is strictly dissipative[110], while the shaded area is the region where the open-loop system admits transient energy growth. Lines correspond to level curves of λ_{max}, and it can be appreciated that the line corresponding to $\lambda_{max} = 0$ lies on the very boundary between the shaded and white areas. This means that the hermitian matrix $\mathbf{B}_r^{\perp}\left(\mathbf{A}_r + \mathbf{A}_r^H\right)\mathbf{B}_r^{\perp H}$ is indefinite when the open-loop system is not strictly dissipative. From the theorem stated above, this implies that a linear state-feedback controller cannot be designed to ensure the closed-loop Poiseuille flow to be strictly dissipative, when the corresponding open-loop flow is not. This result highlights an inherent limitation in the feedback control of the transient growth mechanism, when actuation with the time rate of change of the wall-normal velocity at the walls is used. In a practical setting, perturbations will be spectrally distributed on a broad range of wavenumbers, including those associated to two-dimensional dynamics; hence, the present result is significant in the three-dimensional case as well.

LMI upper bound minimizing controller and results

We now turn to the design of a linear state-feedback controller by using a technique that directly targets the transient growth mechanism. The technique of Whidborne & McKernan[136] to design controllers that minimize the transient growth is

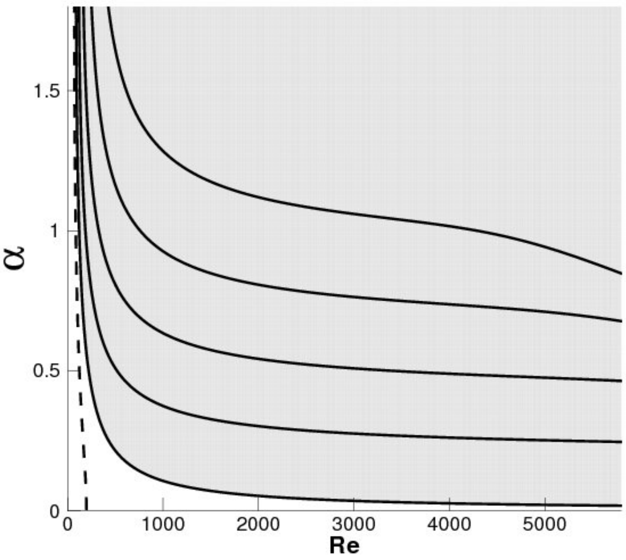

Figure B.1: Numerical verification of the first algebraic criterion in eq. (B.7). Lines: contours of constant $\lambda_{max}(Re, \alpha)$. Levels are from -0.1 to 0.4 by 0.1 increments (from left to right); dashed line is negative value. The shaded area corresponds to the domain where the open-loop system is not strictly dissipative, i.e. admits a transient growth. The level curve corresponding to $\lambda_{max}(Re, \alpha) = 0.0$ lies on the boundary of the region, indicating that no state feedback controller can be designed to ensure strict dissipativity of the closed-loop system when the open-loop system is not strictly dissipative. Result obtained with $N = 100$, $N_t = 50$.

too computationally demanding for this problem. However, a less demanding LMI-based technique [85; 137] that minimizes an upper bound on the transient growth can be used instead. In order to keep controller gains sensibly low, the constraint $\mathbf{u}^H(t)\mathbf{u}(t) \leq \mu^2$ for all $t \geq 0$ is now included in the formulation.

This upper bound minimizing controller is designed for an array of wavenumber pairs, in a plane channel having length $L_x/\delta = 24\pi$ and $\alpha_{max}\delta = 2$, and the same constraint to the control effort $\mu = 100$ is applied to all wavenumbers. The exacting memory requirements of LMI solvers limit matrix sizes to double figures; in the design of the present controller, y discretization was limited to 54 grid points, itself a significant increase over the 20 grid points employed by McKernan[85] in plane Poiseuille flow. Upon inverse Fourier transformation to physical space, controller gains take the form of a convolution kernel. The integral in y direction of the squared value of the kernel is reported in fig. B.2 as a function of x, evidencing compact support. This feature has been noticed previously, e.g., by Högberg et al.[49], when describing the spatial structure of a convolution kernel obtained by a LQR approach in plane Poiseuille flow.

The effectiveness of this kernel has been tested on a direct numerical simulation of perturbed Poiseuille flow, where optimal perturbations are given as initial conditions on the first 24 modes. The DNS is performed with the code developed

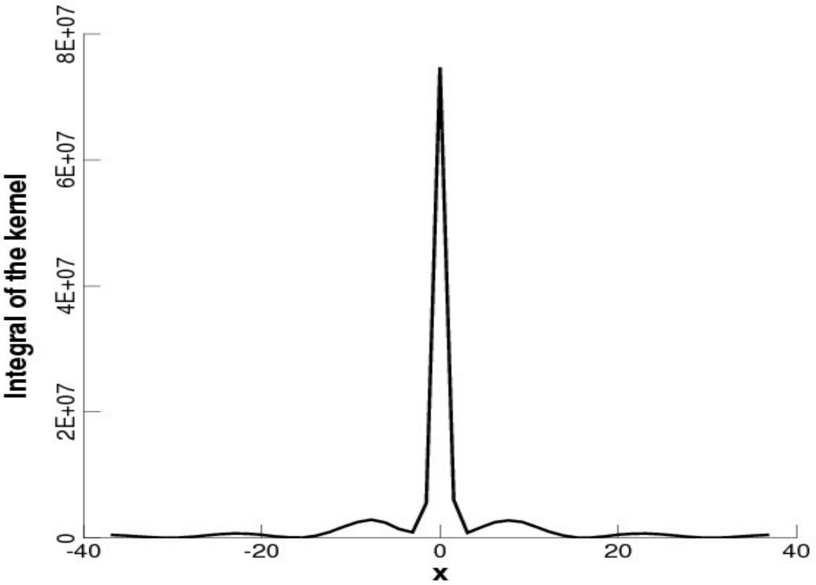

Figure B.2: Integral in y direction of the LMI kernel. Result obtained with $L_x/\delta = 24\pi$, $\alpha_{max}\delta = 2$, $\mu = 100$.

by Luchini & Quadrio[80]; the length of the domain in streamwise direction is $L_x/\delta = 24\pi$ and the value of the Reynolds number is $Re = 500$. Results reported in fig. B.3 show that the maximum energy amplification in the controlled case is about 70% of the one of the uncontrolled system.

Conclusions

In summary, we have exploited a recent result in the field of control theory, to demonstrate that it is impossible to achieve strict dissipativity for the plane Poiseuille flow when using a linear state-feedback controller that uses the time derivative of the wall-normal velocity component at the walls as control variable. We have also proposed a technique, based on a Linear Matrix Inequality approach, that directly addresses the growth mechanism, and we have shown an example result in a fully nonlinear simulation. Clearly, the ability of a feedback controller to completely suppress the transient growth mechanism depends on the kind of actuators used (i.e. the matrix $\mathbf{B}$). Thus, this result does not exclude that feedback controllers designed for systems with different actuators (for instance, tangential actuation, or actuation with the wall-normal velocity itself) may achieve the complete closed-loop suppression of the transient growth mechanism, at least in some range of α and Re. An example of such complete closed-loop suppression was presented by Sharma et al.[125]; however, the actuation in their model was made by a body force (corresponding to having $\mathbf{B}\mathbf{B}^H$ positive definite) instead of the more

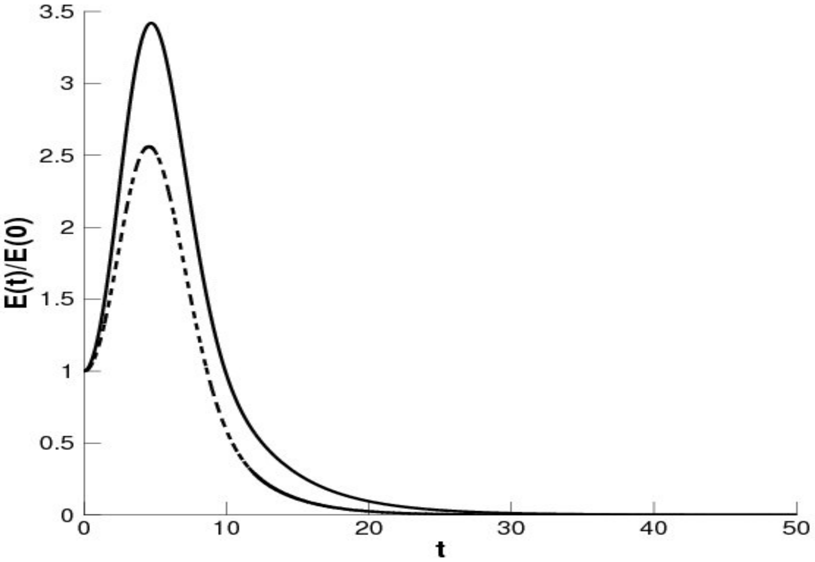

Figure B.3: Time history of the energy in the uncontrolled (solid) and controlled (dashed) cases; results obtained with $L_x/\delta = 24\pi$, $\alpha_{max}\delta = 2$, $\mu = 100$, and the optimal initial condition for the uncontrolled flow is given to both simulations on the first 24 modes.

practically appealing wall-based actuation.

For a given system and actuation technique, the present results provide an alternative and general approach to the design of feedback controllers when the transient behavior of some norm of the state is of interest; moreover, an algebraic criterion is provided to check the existence of fundamental performance limitations in the transient response of the closed-loop system.

Bibliography

[1] F. Abergel and R. Temam. On some control problems in fluid mechanics. *Theor. Comput. Fluid Dyn.*, 1:303–325, 1990.

[2] P. H. Alfredsson, A. V. Johansson, J. H. Haritonidis, and H. Eckelmann. The fluctuating wall-shear stress and the velocity field in the viscous sublayer. *Phys. Fluids*, 31(5):1026–1033, 1988.

[3] B. D. O. Anderson and J. B. Moore. *Optimal control: linear quadratic methods*. Prentice Hall, 1990.

[4] B. Bamieh, F. Paganini, and M. A. Dahleh. Distributed control of spatially invariant systems. *IEEE Trans. Autom. Control*, 47(7):1091–1107, 2002.

[5] A. Baron, M. Quadrio, and L. Vigevano. On the boundary layer/riblets interaction mechanism and the prediction of the turbulent drag reduction. *Int. J. Heat Fluid Flow*, 14(4):324–332, 1993.

[6] D.W. Bechert, M. Bruse, and W. Hage. Experiments with three-dimensional riblets as an idealized model of shark skin. *Exp. Fluids*, 28:403–412, 2000.

[7] J. S. Bendat and A. G. Piersol. *Engineering applications of correlation and spectral analysis*. John Wiley & Sons, 1980.

[8] O. O. Bendiksen. High-altitude limit cycle flutter of transonic wings. *J. Aircraft*, 46(1):123–136, 2009.

[9] T. W. Berger, J. Kim, C. Lee, and J. Lim. Turbulent boundary layer control utilizing the Lorentz force. *Phys. Fluids*, 12(3):631–649, 2000.

[10] T. Bewley. Flow Control: New Challenges for a New Renaissance. *Prog. Aerosp. Sci.*, 37:21–58, 2001.

[11] T. Bewley and O.M. Aamo. A 'win-win' mechanism for low-drag transients in controlled two-dimensional channel flow and its implications for sustained drag reduction. *J. Fluid Mech.*, 499:183–196, 2004.

[12] T. Bewley, P. Moin, and R. Temam. DNS-based predictive control of turbulence: an optimal benchmark for feedback algorithms. *J. Fluid Mech.*, 447:179–225, 2001.

[13] T. Bewley and B. Protas. Skin friction and pressure: the ”footprints” of turbulence. *Physica D*, 2004.

[14] T. R. Bewley. A fundamental limit on the balance of power in a transpiration-controlled channel flow. *J. Fluid Mech. (In Press)*, 2009.

[15] T. R. Bewley and S. Liu. Optimal and robust control and estimation of linear paths to transition. *J. Fluid Mech.*, 365:305–349, 1998.

[16] T. R. Bewley and M. Ziane. A Fundamental Limit on the Heat Flux in the Control of Incompressible Channel Flow. *IEEE Trans. Autom. Control*, 52:2118–2128, 2007.

[17] K. S. Breuer. Micromachined sensors and actuators for the measurement and control of complex flows. In *Proc. of the 1993 AFOSR Contractors Meeting*, 1993.

[18] K.S. Breuer, J. Park, and C. Henoch. Actuation and control of a turbulent channel flow using Lorentz forces. *Phys. Fluids*, 16(4):897–907, 2004.

[19] D. M. Bushnell, J. N. Hefner, and R. L. Ash. Effect of compliant wall motion on turbulent boundary layers. *Phys. Fluids*, 1977.

[20] K.M. Butler and B.F. Farrel. Three-dimensional optimal perturbations in viscous shear flow. *Phys. Fluids*, 4(8):1637–1650, 1992.

[21] P. W. Carpenter and A. D. Garrad. The hydrodinamic stability of flow over Kramer-type surfaces. Part 1. Tollmien-Schlichting instabilities. *J. Fluid Mech.*, 155:465–510, 1985.

[22] P. W. Carpenter and A. D. Garrad. The hydrodinamic stability of flow over Kramer-type surfaces. Part 2. Flow-induced surfaces instabilities. *J. Fluid Mech.*, 170:199–232, 1986.

[23] J. J. Chattot. Low speed design and analysis of wing/winglet combinations including viscous effects. *J. Aircraft*, 2006.

[24] M. Chevalier, J. Höpffner, T. R. Bewley, and D.S. Henningson. State estimation in wall-bounded flow systems. Part 2. Turbulent flows. *J. Fluid Mech.*, 552:167–187, 2006.

[25] H. Choi, P. Moin, and J. Kim. Direct numerical simulation of turbulent flow over riblets. *J. Fluid Mech.*, 255:503, 1993.

[26] H. Choi, P. Moin, and J. Kim. Active turbulence control for drag reduction in wall-bounded flows. *J. Fluid Mech.*, 262:75–110, 1994.

[27] K.-S. Choi. Near-wall structure of a turbulent boundary layer with riblets. *J. Fluid Mech.*, 208:417–458, 1989.

[28] K.-S. Choi, J.R. DeBisschop, and B.R. Clayton. Turbulent boundary-layer control by means of spanwise-wall oscillation. *AIAA J.*, 36(7):1157–1162, 1998.

[29] K.-S. Choi, X Yang, B. R. Clayton, E. J. Glover, M. Atlar, B. N. Semenov, and V. M. Kulik. Turbulent drag reduction using compliant surfaces. In *Mathematical, Physical and Engineering Sciences*, volume 453, pages 2229–2240, 1997.

[30] P. Corbett and A. Bottaro. Optimal control of nonmodal disturbances in boundary layers. *Theor. Comput. Fluid Dyn.*, 15:65–81, 2001.

[31] L. Cortelezzi and J. Speyer. Robust reduced-order controller of laminar boundary layer transition. *Phys. Rev. E*, 1998.

[32] B. N. Datta. *Numerical Methods for Linear Control Systems*. Elsevier, 2004.

[33] E. De Angelis, Casciola. C.M., R. Benzi, and R. Piva. Homogeneous isotropic turbulence in dilute polymers. *J. Fluid Mech.*, 531:1–10, 2005.

[34] J. W. Dettman. *Mathematical Methods in Physics and Engineering*. Dover, 1988.

[35] X. Fan, L. Hofmann, and T. Herbert. Active flow control with neural networks. In *AIAA Paper No. 93-3273*, 1993.

[36] B. Friedland. *Control System Design*. Dover Publications, 2005.

[37] B. Frohnapfel, P. Lammers, J. Jovanovic, and F. Durst. Interpretation of the mechanism associated with turbulent drag reduction in terms of anisotropy invariants. *J. Fluid Mech.*, 577:457–466, 2007.

[38] K. Fukagata, K. Iwamoto, and N. Kasagi. Contribution of Reynolds stress distribution to the skin friction in wall-bounded flows. *Phys. Fluids*, 14(11), 2002.

[39] M. Gad-el Hak. Modern developments in flow control. *Appl. Mech. Rev.*, 49:365–379, 1996.

[40] M. Gad-el Hak. *Flow Control – Passive, Active and Reactive Flow Management*. Cambridge University Press, 2000.

[41] M. Gad-el Hak. Flow Control: the Future. *J. Aircraft*, 38(3):402–418, 2001.

[42] M. Gad-el Hak and D.M. Bushnell. Separation Control: Review. *J. Fluid Eng.*, 113(3):5–29, 1991.

[43] K. A. Gallivan, S. Thirumalai, P. Van Dooren, and V. Vermaut. High performance algorithms for Toeplitz and block Toeplitz matrices. *Linear algebra and its applications*, 1996.

[44] J. Gollub, H. Fernando, M. Garib, J. Kim, S. Pope, A. Smits, and H. Stone. Research in Fluid Dynamics: Meeting National Needs. Report of the U.S. National Committee on Theoretical and Applied Mechanics, 2006.

[45] E.P. Hammond, T.R. Bewley, and P. Moin. Observed mechanisms for turbulence attenuation and enhancement in opposition-controlled wall-bounded flows. *Phys. Fluids*, 10(9):2421–2423, 1998.

[46] J. H. Haritonidis. *The measurement of wall shear stress*. Springer-Verlag Berlin, 1988.

[47] C.-M. Ho. UCLA Micro Systems Laboratories. http://ho.seas.ucla.edu/.

[48] C.-M. Ho and Y.-C. Tai. MEMS and fluid flow. *Ann. Rev. Fluid Mech.*, 30:579–612, 1998.

[49] M. Högberg, T.R. Bewley, and D. Henningson. Linear feedback control and estimation of transition in plane channel flow. *J. Fluid Mech.*, 481:149–175, 2003.

[50] M. Högberg, T.R. Bewley, and D. Henningson. Relaminarization of $Re_\tau = 100$ turbulence using gain scheduling and linear state-feedback control. *Phys. Fluids*, 15(11):3572–3575, 2003.

[51] J. Höpffner, M. Chevalier, T. R. Bewley, and D.S. Henningson. State estimation in wall-bounded flow systems. Part 1. Perturbed laminar flows. *J. Fluid Mech.*, 534:263–294, 2005.

[52] A.K.M.F. Hussain and W.C. Reynolds. The mechanics of an organized wave in turbulent shear flow. *J. Fluid Mech.*, 41(2):241–258, 1970.

[53] A.K.M.F. Hussain and W.C. Reynolds. The mechanics of an organized wave in turbulent shear flow. Part 2. Experimental results. *J. Fluid Mech.*, 54(2):241–261, 1972.

[54] K. Iwamoto, K. Fukagata, N. Kasagi, and Y. Suzuki. Friction drag reduction achievable with near-wall manipulation at high Reynolds numbers. *Phys. Fluids*, 17(011702):4, 2005.

[55] K. Iwamoto, Y. Suzuki, and N. Kasagi. Reynolds number effect on wall turbulence: toward effective feedback control. *Int. J. Heat Fluid Flow*, 23:678–689, 2002.

[56] S. A. Jacobson and W. C. Reynolds. Active control of streamwise vortices and streaks in boundary layers. *J. Fluid Mech.*, 360:179–211, 1998.

[57] S. Jeon, H. Choi, J. Y. Yoo, and P. Moin. Space-time characteristics of wall shear-stress fuctuations in a low-Reynolds-number channel flow. *Phys. Fluids*, 11(10):3084–3094, 1999.

[58] D. Jerison and D. Stroock. Norbert Wiener. *Notices of the AMS*, 42(4):430–438, 1994.

[59] J. Jiménez and A. Pinelli. The autonomous cycle of near-wall turbulence. *J. Fluid Mech.*, 389:335–359, 1999.

[60] S.S. Joshy, J.L. Speyer, and J. Kim. A system theory approach to the feedback stabilization of infinitesimal and finite-amplitude perturbations in plane Poiseuille flow. *J. Fluid Mech.*, 332:157–184, 1997.

[61] W.J. Jung, N. Mangiavacchi, and R. Akhavan. Suppression of turbulence in wall-bounded flows by high-frequency spanwise oscillations. *Phys. Fluids A*, 4 (8):1605–1607, 1992.

[62] T. Kailath. *Linear Systems*. Prentice Hall, 1980.

[63] N. Kasagi, Y. Suzuki, and K. Fukagata. Miroelectromechanical systems-based feedback control of turbulence for skin friction reduction. *Ann. Rev. Fluid Mech.*, 2009.

[64] J. Kim. Control of turbulent boundary layers. *Phys. Fluids*, 15(5):1093–1105, 2003.

[65] J. Kim and T. R. Bewley. A linear systems approach to flow control. *Ann. Rev. Fluid Mech.*, 39:383–417, 2007.

[66] J. Kim and J. Lim. A linear process in wall-bounded turbulent flows. *Phys. Fluids*, 12(8):1885–1888, 2000.

[67] J. Kim, P. Moin, and R. Moser. Turbulence statistics in fully developed channel flow at low Reynolds number. *J. Fluid Mech.*, 177:133–166, 1987.

[68] M. O. Kramer. Boundary layer stabilization by distributed damping. *J. Aero. Sci.*, 1957.

[69] T. S. J. Lammerink, M. Elwenspoek, and J. H. J. Fluitman. Optical excitation of micro-mechanical resonators. In *Proc. 1991 IEEE MEMS Workshop*, 1991.

[70] M. T. Landahl. On sublayer streaks. *J. Fluid Mech.*, 212:593–614, 1990.

[71] C. Lee, J. Kim, D. Babcock, and R. Goodman. Application of neural networks to turbulence control for drag reduction. *Phys. Fluids*, 9:1740–1747, 1997.

[72] C. Lee, J. Kim, and H. Choi. Suboptimal control of turbulent channel flow for drag reduction. *J. Fluid Mech.*, 358:245–258, 1998.

[73] G. B. Lee, C. Shih, Y.-C. Tai, T. Tsao, C. Liu, A. Huang, and C.-M. Ho. Robust Vortex Control of a Delta Wing by Distributed Microelectromechanical-Systems Actuators. *J.Aircraft*, 37(4):697–706, 2000.

[74] K. H. Lee, L. Cortelezzi, J. Kim, and J. Speyer. Application of reduced-order controller to turbulent flows for drag reduction. *Phys. Fluids*, 13(5), 2001.

[75] J. Lighthill. *An Informal Introduction to Theoretical Fluid Mechanics*. Clarendon Press, Oxford, 1986.

[76] J. Lim. *Control of wall-bounded turbulent shear flows using modern control theory*. PhD thesis, Univ. Of California, Los Angeles, 2003.

[77] P. Luchini. Reynolds-number-independent instability of the boundary layer over a flat surface: optimal perturbations. *J. Fluid Mech.*, 404:289–309, 2000.

[78] P. Luchini. Acoustic Streaming and Lower-than-Laminar Drag in Controlled Channel Flow. In L. L. Bonilla, M. Moscoso, G. Platero, and J. M. Vega, editors, *Mathematics in Industry*, pages 169–177. Springer, 2008.

[79] P. Luchini. Phase-locked linear response and the optimal feedback control of near-wall turbulence. In Liguori, editor, *Mathematical Physics Models and Engineering Sciences*. Napoli, 2008.

[80] P. Luchini and M. Quadrio. A low-cost parallel implementation of direct numerical simulation of wall turbulence. *J. Comp. Phys.*, 211(2):551–571, 2006.

[81] P. Luchini, M. Quadrio, and S. Zuccher. Phase-locked linear response of a turbulent channel flow. *Phys. Fluids*, 18(121702):1–4, 2006.

[82] J. Lumley and I. Kobu. Turbulent drag reduction by polymer additives: a survey. In B. Gampert – Springer Verlag, editor, *The Influence of Polymer Additives on Velocity and Temperature Fields (IUTAM symposium Essen 1984)*, 1985.

[83] J. L. Lumley. Drag reduction in two-phase and polymer flows. *Physics of Fluids*, 20(10):64, 1977.

[84] J. L. Lumley and G. R. Newman. The return to isotropy of homogeneous turbulence. *J. Fluid Mech.*, 82(1):161–178, 1977.

[85] J. McKernan. *Control of plane Poiseuille flow: a theoretical and computational investigation*. PhD thesis, Department of Aerospace Sciences, School of Engineering, Cranfield University, 2006.

[86] J. McKernan, J.F. Whidborne, and G. Papadakis. Linear quadratic control of plane Poiseuille flow - the transient behaviour. *Internat. J. Control*, 80(12):1912–1930, December 2007.

[87] H. U. Meier and M. D. Zhou. The development of acoustic generators and their application as a boundary layer transition control device. *Exp. Fluids*, 11:93–104, 1991.

[88] T. Min, S.M. Kang, J.L. Speyer, and J. Kim. Sustained sub-laminar drag in a fully developed channel flow. *J. Fluid Mech.*, 558:309–318, 2006.

[89] P. Moin and T. Bewley. Feedback control of turbulence. *Appl. Mech. Rev.*, 47(6):S3–S13, 1994.

[90] M. Morari and E. Zafiriou. *Robust Process Control*. Prentice Hall, 1998.

[91] R. Moser, J. Kim, and N.N. Mansour. Direct numerical simulation of turbulent channel flow up to $Re_\theta = 590$. *Phys. Fluids*, 11(4):943–945, 1999.

[92] W. Nitsche, P. Mirow, and J. Szodruch. Piezo-electric foils as a means of sensing unsteady surface forces. *Exp. Fluids*, 7(2):111–118, 1989.

[93] B. Noble. *Methods based on the Wiener-Hopf Technique for the solution of partial differential equations*. Chelsea Publishing Company, 1988.

[94] J. Pang and K.-S. Choi. Turbulent drag reduction by Lorentz force oscillation. *Phys. Fluids*, 16(5):L35–L38, 2004.

[95] R.L. Panton. Overview of the self-sustaining mechanisms of wall turbulence. *Prog. Aerospace Sc.*, 37:341–383, 2001.

[96] A. Papoulis. *Probability and statistics*. Prentice Hall, 1990.

[97] E. Plischke. *Transient effects of linear dynamical systems*. PhD thesis, Universitat Bremen, Germany, 2005.

[98] E. Plischke and F. Wirth. Stabilization of linear systems with prescribed transient bounds. In *Proc. 16th Int. Symp. Math. Theory Networks Syst.*, Leuven, Belgium, 2004.

[99] S.B. Pope. *Turbulent Flows*. Cambridge University Press, 2000.

[100] M. L. Post and T. C. Corke. Separation Control of High Angle of Attack Airfoil using Plasma Actuators. *AIAA J.*, 42(11), 2004.

[101] M. Quadrio. Streamwise-traveling waves of spanwise velocity at the wall of a turbulent channel flow. In *iTi Conference on Turbulence, Bertinoro (I), October 12-15, 2008*, 2008.

[102] M. Quadrio and P. Luchini. Integral time-space scales in turbulent wall flows. *Phys. Fluids*, 15(8):2219–2227, 2003.

[103] M. Quadrio and P. Luchini. Method for reducing the viscous friction between a fluid and an object. International Patent, N. WO 2009/000703 A1, 2009.

[104] M. Quadrio and P. Ricco. Critical assessment of turbulent drag reduction through spanwise wall oscillation. *J. Fluid Mech.*, 521:251–271, 2004.

[105] M. Quadrio and P. Ricco. Generalized Stokes layer by streamwise-traveling waves of spanwise wall velocity. *Submitted to J. Fluid Mech.*, 2008.

[106] M. Quadrio, P. Ricco, and C. Viotti. Streamwise-traveling waves of spanwise wall velocity for turbulent drag reduction. *J. Fluid Mech.*, 2009.

[107] M. Quadrio and P.A. Ricco. Initial response of a turbulent channel flow to spanwise oscillation of the walls. *J. Turbulence*, 4(7), 2003.

[108] R. Rathnasingham and K.S. Breuer. Active control of turbulent boundary layers. *J. Fluid Mech.*, 495:209–233, 2003.

[109] H. Rebbeck and K.-S. Choi. Opposition control of near-wall turbulence with a piston-type actuator. *Phys. Fluids*, 13(8):2142–2145, 2001.

[110] S.C. Reddy and D.S. Henningson. Energy growth in viscous channel flows. *J. Fluid Mech.*, 252:209–238, 1993.

[111] R. M. Rennie and E. J. Jumper. Gust alleviation using trailing-edge flaps. In *37th AIAA Aerospace Meeting and Exhibit*, 1999.

[112] W.C. Reynolds and A.K.M.F. Hussain. The mechanics of an organized wave in turbulent shear flow. Part 3. Theoretical models and comparison with experiments. *J. Fluid Mech.*, 54(2):263–288, 1972.

[113] P. Ricco. Modification of near-wall turbulence due to spanwise wall oscillations. *J. Turbulence*, 5(24), 2004.

[114] P. Ricco and M. Quadrio. Wall-oscillation conditions for drag reduction in turbulent channel flow. *Int. J. Heat Fluid Flow*, 29:601–612, 2008.

[115] P. Ricco and S. Wu. On the effects of lateral wall oscillations on a turbulent boundary layer. *Exper. Therm. Fluid Sc.*, 29(1):41–52, 2004.

[116] J. Rissanen. Recursive identification of linear systems. *SIAM J. Control*, 9(3), 1971.

[117] S. Bagheri, L. Brandt, and D. S. Henningson. Input-output analysis, model reduction and control of the flat-plate boundary layer. *J. Fluid Mech.*, 620:263–298, 2009.

[118] A. H. Sayed and T. Kailath. A survey of spectral factorization methods. *Num. Lin. Alg. Appl.*, 8:467–496, 2001.

[119] H. Schlichting and K. Gersten. *Boundary-Layer Theory*. Springer, 2000.

[120] P. J. Schmid and D. S. Henningson. A new mechanism for rapid transition involving a pair of oblique waves. *Phys. Fluids*, 4(9):1986–1989, 1992.

[121] P. J. Schmid and D. S. Henningson. *Stability and Transition in Shear Flows*. Springer, 2001.

[122] P.J. Schmid and D.S. Henningson. Optimal energy density growth in Hagen-Poiseuille flow. *J. Fluid Mech.*, 277:197–255, 1994.

[123] W. Schoppa and F. Hussain. Coherent structure generation in near-wall turbulence. *J. Fluid Mech.*, 453:57–108, 2002.

[124] G. Schrauf. Key Aerodynamic Technologies for Aircraft Performance Improvement. In *5th Community Aeronautics Days*, 2006.

[125] A. S. Sharma, D. J. N. Limebeer, B. J. McKeon, and J. F. Morrison. Stabilising control laws for the incompressible Navier-Stokes equations using sector stability theory. In *3rd AIAA Flow Control Conference*, 2006.

[126] C. H. Sieverding and C. Warsop. MEMS and Active Flow Control. In Von Karman Institute, editor, *VKI Lecture Series*, 2002.

[127] S. Skogestad and I. Postlethwaite. *Multivariable feedback control.* Wiley, Chichester, England, 1996.

[128] V. I. Smirnov. *A course of Higher Mathematics - Vol. IV.* Pergamon Press, 1964.

[129] T. W. Strganac, J. Ko, D. E. Thompson, and A. J. Kurdila. Identification and control of limit cycle oscillations in aeroelastic systems. *J. Guid. Con. Dyn.*, 23(6):1127–1133, 2000.

[130] H.J. Sussmann and P.V. Kokotovic. The peaking phenomenon and the global stabilization of nonlinear systems. *IEEE Trans. Autom. Control*, 36(4):424–440, 1991.

[131] D. P. Telionis. *Unsteady Viscous Flow*. Springer-Verlag, New York, 1981.

[132] T. Tsao, F. Jiang, R. Miller, Y.-C. Tai, B. Gupta, R. Goodman, S. Tung, and C.-M. Ho. An integrated MEMS system for turbulent boundary layer control. In *International Conference on Solid State Sensors and Actuators, 1997. TRANSDUCERS '97 Chicago., 1997*, volume 1, pages 315–318, 1997.

[133] W. J. Vankan, R. Maas, and M. Laban. Fitting fitness in aircraft design. In *Proceedings of the ICAS Conference*, 2006.

[134] P. S. Virk. Drag reduction in rough pipes. *J. Fluid Mech.*, 45(2):225–246, 1971.

[135] M.J. Walsh. Drag characteristics of V-groove and transverse curvature riblets. *In Viscous Drag reduction (ed. G.R. Hough). American Institute of Aeronautics and Astronautics.*, 1980.

[136] J. Whidborne and J. McKernan. On the Minimization of Maximum Energy Growth. *IEEE Trans. Autom. Control*, 52(9):1762–1767, 2007.

[137] J.F. Whidborne, J. McKernan, and G. Papadakis. Minimising transient energy growth in plane poiseuille flow. *Proc. IMechE J. Syst. Contr. Eng.*, 2008. To be published.

[138] Y. Xu, Y.-C. Tai, A. Huang, and C.-M. Ho. IC-Integrated Flexible Shear-Stress Sensor Skin. *J. Microelec. Syst.*, 12(5):740–747, 2003.

[139] D.C. Youla, J.J. Bongiorno, and H.A. Jabr. Modern Wiener-Hopf design of Optimal Controllers. Part I: The Single-Input-Output Case. *IEEE Trans. Autom. Control*, ac-21(1):3–13, 1976.

[140] D.C. Youla, H.A. Jabr, and J.J. Bongiorno. Modern Wiener-Hopf design of Optimal Controllers. Part II: The Multivariable Case. *IEEE Trans. Autom. Control*, ac-21(3):319–338, 1976.

[141] K. Zhou, J. C. Doyle, and K. Glover. *Robust and Optimal Control.* Prentice Hall, 1996.

[142] S. Zuccher, P. Luchini, and A. Bottaro. Algebraic growth in a Blasius boundary layer: optimal and robust control by mean suction in the nonlinear regime. *J. Fluid Mech.*, 513:135–160, 2004.